Chemotaxis, Shape and Adhesion Dynamics of Amoeboid Cells Studied by Impedance Fluctuations in Open and Confined Spaces

A Dissertation
submitted to the Faculty of Sciences
of Potsdam University
in partial fulfilment of the requirements
for the degree of
Doctor of Sciences
(Dr. rer. nat.)

Helmar M. Leonhardt
May 2017

Published online at the
Institutional Repository of the University of Potsdam:
URN urn:nbn:de:kobv:517-opus4-405016
http://nbn-resolving.de/urn:nbn:de:kobv:517-opus4-405016

ZUSAMMENFASSUNG

Die vorliegende Arbeit befasst sich mit elektrischen Impedanzmessungen von amöboiden Zellen auf Mikroelektroden. Der Modellorganismus *Dictyostelium discoideum* zeigt unter der Bedingung des Nahrungsentzugs einen Übergang zum kollektiven Verhalten, bei dem sich chemotaktische Zellen zu einem multizellulären Aggregat zusammenschließen. Wir zeigen wie Impedanzaufnahmen über die Dynamik der Zell-substrat Adhäsion ein präzises Bild der Phasen der Aggregation liefern. Darüberhinaus zeigen wir zum ersten mal systematische Einzelzellmessungen von Wildtyp-Zellen und vier Mutanten, die sich in der Stärke der Substratadhäsion unterscheiden. Wir zeichneten die projizierte Zellfläche durch Zeitverlaufsmikroskopie auf und fanden eine Korrelation zwischen den quasi-periodischen Oszillationen in der Kinetik der projizierten Fläche — der Zellform-Oszillation — und dem Langzeittrend des Impedanzsignals. Amöboidale Motilität offenbart sich typischerweise durch einen Zyklus von Membranausstülpung, Substratadhäsion, Vorwärtsziehen des Zellkörpers und Einziehen des hinteren Teils der Zelle. Dieser Motilitätszyklus resultiert in quasi-periodischen Oszillationen der projizierten Zellfläche und der Impedanz. In allen gemessenen Zelllinien wurden für diesen Zyklus ähnliche Periodendauern beobachtet trotz der Unterschiede in der Anhaftungsstärke. Wir beobachteten, dass die Stärke der Zell-substrat Anhaftung die Impedanz stark beeinflusst, indem die Abweichungen vom Mittelwert (die Größe der Fluktuationen) vergrößert sind bei Zellen, die die vom Zytoskelett generierten Kräfte effektiv auf das Substrat übertragen. Zum Beispiel sind bei $talA^-$ Zellen, in welchen das Actin verankernde Protein Talin fehlt, die Fluktuationen stark reduziert. Einzelzellkraft-Spektroskopie und Ergebnisse eines Ablösungsassays, bei dem Adhäsionskraft gemessen wird indem Zellen einer Scherspannung ausgesetzt werden, bestätigen, daß die Größe der Impedanzfluktuationen ein korrektes Maß für die Stärke der Substratadhäsion ist. Schließlich haben wir uns auch mit dem Einbau von Zell-substrat-Impedanz-Sensoren in mikrofluidische Apparaturen befasst. Ein chip-basierter elektrischer Chemotaxis Assay wurde entwickelt, der die Geschwindigkeit chemotaktischer Zellen misst, welche entlang eines chemischen Konzentrationsgradienten über Mikroelektroden wandern.

ABSTRACT

We present electrical impedance measurements of amoeboid cells on microelectrodes. The model organism *Dictyostelium discoideum* shows under starvation conditions a transition to collective behavior when chemotactic cells collect in multicellular aggregates. We show how impedance recordings give a precise picture of the stages of aggregation by tracing the dynamics of cell-substrate adhesion. Furthermore, we present for the first time systematic single cell measurements of wild type cells and four mutant strains that differ in their substrate adhesion strength. We recorded the projected cell area by time lapse microscopy and found a correlation between quasi-periodic oscillations in the kinetics of the projected area — the cell shape oscillation — and the long-term trend in the impedance signal. Typically, amoeboid motility advances via a cycle of membrane protrusion, substrate adhesion, traction of the cell body and tail retraction. This motility cycle results in the quasi-periodic oscillations of the projected cell area and the impedance. In all cell lines measured, similar periods were observed for this cycle, despite the differences in attachment strength. We observed that cell-substrate attachment strength strongly affects the impedance in that the deviations from mean (the magnitude of fluctuations) are enhanced in cells that effectively transmit forces, generated by the cytoskeleton, to the substrate. For example, in $talA^-$ cells, which lack the actin anchoring protein talin, the fluctuations are strongly reduced. Single cell force spectroscopy and results from a detachment assay, where adhesion is measured by exposing cells to shear stress, confirm that the magnitude of impedance fluctuations is a correct measure for the strength of substrate adhesion. Finally, we also worked on the integration of cell-substrate impedance sensors into microfluidic devices. A chip-based electrical chemotaxis assay is designed which measures the speed of chemotactic cells migrating over microelectrodes along a chemical concentration gradient.

Contents

1 INTRODUCTION

This interdisciplinary and experimental doctoral thesis in the field of biological physics is concerned with the electrical detection and monitoring of micromotion of cultured biological cells interfaced to microelectrodes in open and confined spaces. The technological principles are the result of developments of electrical cell-based micro sensors on one hand, such as microwire or micropipette electrodes and later whole planar microelectrode arrays to study electrical activity of cells, and cultivation and preparation of living tissues *in vitro*, of organ and cell cultures under controlled conditions on the other hand [1, 2]. These techniques enabled studies of cellular functions of single cells and cell populations outside from their natural environment. Cultured cells provide the basis to examine noninvasively electrics and dielectrics of the cellular shelled system composed of an ionic solution content enclosed by a lipid bilayer plasma membrane. Ion channels and pumps in the membrane generate electric activity, which is studied in neurosciences. Adaption to and control of stimuli by a cell turns the cell itself into a sensor when recording its electrical response to these stimuli. This work however focusses on the passive electrical properties of biological cells when exposed to weak alternating electric fields, which was the subject of research of hundred years [3, 4]. Electric fields act as the sensing element for uncovering the resistive, conductive and capacitive characteristics of shelled particles or cells in suspension or when anchored to electrode surfaces via adhesion systems.

By recording the time trace of the impedance the process of cell movement can be monitored since this physical process consists of an interaction with the underlying substrate. The movement of the cell body by exertion of traction forces to the substrate is achieved by dynamic assembly and disassembly of localized cell-matrix adhesions (focal adhesions), which enables the cell to transmit tensile forces from bundled actin filaments at the intracellular side of the basal membrane to the substrate mediated by transmembrane receptors, usually integrins [5, 6]. Interference reflection microscopy studies revealed the existence of a cell-substratum gap and regions of different separations within this gap, highly dynamic structures modulated by a cell during movement [7]. These processes associated with adhesion take place at the subcellular scale and are invisible in brightfield

microscopy. Giaever and Keese were among the first who showed that cultured cells on the surface of microelectrodes cause fluctuations of the impedance, which proceed even in cases when a confluent cell layer has formed and shape changes of single cells are no longer observed [8]. Shape changes at the cellular scale alter the fraction of membrane coverage of electrodes and thus affect the impedance. Adhesion dynamics on the subcellular scale however cause fluctuations of the impedance, since the current flow through the cell-substratum gap sensitively reacts to modulations of the substrate separation. Thus, a noninvasive and label-free method was found to monitor shape oscillations and adhesion dynamics of cell populations and even single cells. The method was called ECIS — Electric Cell-substrate Impedance Sensing [8–18].

Cyclic shape changes, governed by actin polymerization (protrusion) and actomyosin contraction (retraction), and attachment/detachment dynamics constitute the crawling-type motion and locomotion of *Dictyostelium discoideum* and other amoeboid cell types [19, and references therein]. The motility cycle appears as an intrinsic property of amoebae, during most stages of their life cycle and under various environmental conditions, and can be performed without external cues. However, in chemotaxis- and aggregation-competent cells, the morphological changes are dependent on the chemotactic dynamics initiated by receptor-ligand interactions. For *Dictyostelium* cells displacement and directed motion must be accomplished in cooperation and synchrony for successful aggregation, which is mediated by waves of the chemoattractant cyclic adenosine 3',5'-monophosphate (cAMP) emitted from signaling aggregation centers. When cAMP binds to its receptors, the cells respond by performing coordinated steps in direction of the wave source. Time lapse microscopy studies reveal the development of cooperative behavior during the pre-aggregation phase by identifying the formation of cell clusters and streams to aggregation centers on the population level. Pattern formation in a field of aggregating amoebae evolves by spatial correlation of shape changes and becomes visible by dark field illumination of the aggregation plane [19, Fig.8.1]. ECIS has shown to yield new insights in the aggregation process by uncovering the time trace of substrate interactions [20, 21]. Moreover, impedance recordings display a phase transition to coherent impedance oscillations and measure time, phase and frequency of progressive entrainment of cells in collective behavior more precisely than other methods.

Dictyostelium discoideum is a widely used model organism. Its genome has been sequenced and a variety of mutants are available for systematic studies of gene functions involved in motility, chemotaxis or the emergence of multicellularity [22]. This work focusses on the study of mutants lacking

proteins involved in cell-substrate adhesion, which link filamentous actin bundles to the membrane or which have a function in actin polymerization. None of these mutants exhibit a severe loss of substrate adhesion, and we demonstrate for the first time by systematic impedance recordings of single cells on microelectrodes how their differences in adhesion strength are detected electrically.

Chemotaxis is the process of receptor-mediated directional sensing and locomotion in direction of a chemical gradient, which is normally quantified by time lapse microscopy and automated cell tracking methods for analysis of cell trajectories [23, 24]. Chemical concentration gradients are prepared by using classical methods as for example micropipettes, agar plates, boyden chambers, or more sophisticated techniques to create stable surface-chemical gradients or printed chemical gradients [25, 26]. Microfluidic device fabrication by Polydimethylsiloxane (PDMS) Soft Lithography and replica molding has become a major approach to create stable arbitrary shaped concentration gradients in microchannels [27–29]. Moreover, microfluidics has great potential and versatility for integration and combination of tasks and functions in a micro-laboratory [30]. In biological sciences it facilitates the creation of controlled micro-environments for the study of cell functions. This work is concerned with the design and construction of chip-based electrical chemotaxis assays and therefore primarily focusses on the technological principles and requirements for the integration of cell-substrate impedance sensors into microfluidic channel systems. The experimental setup presented here can be seen as a first proof of principle that will serve as the basis for further integration of components into a multifunctional platform, which, of course, becomes challenging the more complicated the process of fabrication is. In the experiments presented in this work planar microelectrode arrays are used as the substrate for a system of microchannels, in which a cell inlet reservoir is connected to the gradient chamber of a microfluidic gradient generator. Migration of cells is traced by guiding chemotactic cells across a spatially arranged set of microelectrode stripes. Also an alternative method for compact electrode arrangement and the generation of a chemical gradient is presented.

In chapter 2 (Background) we introduce the reader in the principles of impedance measurement, show the spectral impedance of a cell-free and cell-covered electrode system, give an overview of the adhesion systems of *Dictyostelium* cells and the performance of impedance measurements in microfluidic channels.

In chapter 3 (Materials and methods) the experimental setup is presented and data processing routines, cell culture and alternative methods for independent measurements of substrate adhesion are described. Also, the

fabrication process of microelectrode arrays and microfluidic devices, the performance of concentration gradient generators, the setup for an electrical cell migration assay and alternative methods for electrode disposal and gradient preparation are specified.

In chapter 4 (Results) we show the results and some conclusions of our experiments. These results are ordered in single cell measurements, cell population measurements and measurements of chemotactic cell migration.

In chapter 5 (Discussion) we discuss our results, their implications and possible further developments in future.

2 BACKGROUND

2.1 Electrical Impedance

If a material is placed in an electric field, than its opposition to a flow of direct current is called electrical resistance, whose value characterizes the electrical properties of this material compared to other materials. The field may penetrate more or less into the material, depending on its inner composition, which in the case of direct current is evaluated by the strength of the field obtained when the material is placed into it. This method of sensing small structures down to nanometer levels can be extended when using an alternating current electric field. Besides the field strength, given by the wave amplitude, we then obtain new insights into the response of any system with respect to wave frequency and phase. The corresponding resistance to AC current flow is the complex electrical impedance, which can be measured by applying a sinusoidal voltage with amplitude V_0 and phase ϕ to the system under investigation and measuring amplitude I_0 and phase φ of the current flowing through the sample. The electrical impedance is usually represented by a phasor,

$$\mathbf{Z} = Ze^{i\Delta\Phi} \quad , \tag{2.1}$$

whose magnitude $Z = V_0/I_0$ and phase shift $\Delta\Phi = \phi - \varphi$ are given by Ohm's law, using complex expressions for voltage and current:

$$\mathbf{Z} = \frac{\mathbf{V}}{\mathbf{I}} = \frac{V_0 e^{i(\omega t+\phi)}}{I_0 e^{i(\omega t+\varphi)}} = \frac{V_0}{I_0} e^{i(\phi-\varphi)} = Ze^{i\Delta\Phi} \tag{2.2}$$

The above described method to measure magnitude and phase of the impedance requires a linear response of the system, where the current output is also a sinusoidal as the voltage excitation signal, with the same frequency, but with different amplitude and phase. Complex systems, however, are often nonlinear, but display a pseudo-linear response regime, when a small excitation signal ($\leqslant 10mV$) is used. For a pseudo-linear response, which may be constant over a certain time interval, above used Ohm's law is fulfilled and phase shift between voltage and current is also constant over this interval for a given AC frequency.

The opposition of a passive complex electrical system to an AC electric field is not restricted by energy dissipation, as in the case of a purely resistive element due to *friction* against the motion of electrons, which produces a voltage drop that is in-phase with the current. But, as in the case of capacitive or inductive elements, it is also affected by the reactance of the system, meaning the occurrence of *inertia* against the motion of electrons, which produces a voltage drop that is 90° out of phase with the current. Impedance is a comprehensive complex expression of all forms of opposition to electron flow [31]. Resistance and reactance are given by the real and imaginary part of the impedance. For a purely capacitive reactance, the phase angle between the voltage across a measurement probe and the current through that probe will be −90°, i.e. voltage lags current, whereas for a purely inductive reactance it will be 90°, i.e. voltage leads current. The current response of real heterogeneous systems to an applied potential difference will display phase shifts somewhere in between this ideal cases. We will focus here on the capacitive reactance of interfaces, whose characterization has become a major concern of electrochemistry and material science [32]. But also in biophysics, the electrode-electrolyte interface of (micro)electrodes has become an important topic. The inherent capacitive reactance of such systems produces negative phase shifts between 0° and −90°. Phase shift as well as the magnitude of impedance display the fundamental property of AC frequency dependence. The discovery of impedance dispersions has made impedance spectroscopy to an important characterization tool.

Equivalent circuits, based on mathematical models derived from plausible physical principles, are basic concepts to characterize and interpret experimental data of electrode-material systems. Usually, RC-circuits are developed to describe dispersions of electrode-solution interfaces and their overall capacitive reactance. A parallel combination of a resistor and capacitor displays a single impedance dispersion, which can be regarded as a basic property of such interfaces, despite further elements (for example Constant Phase Elements, CPE's), which had to be included to cope with experimental data. Dispersion of impedance magnitude and phase are governed by a single time constant and its corresponding frequency. At this characteristic frequency, the dispersion of magnitude and phase of the impedance becomes most pronounced. Such a simple system may represent a thin layer or slab of homogeneous material, whose ability to store electrical charge is quantified by its capacitance $C = \varepsilon A/d$, where ε is the dielectric permittivity, A the cross-sectional area and d the thickness of the material [33]. In the following we give a more detailed description of the electrode-solution interface.

2.2 The cell-free electrode system

When an electrode is placed in an electrolyte, an electrochemical double layer forms at the electrode-electrolyte interface due to an unequal distribution of charge across the two phases. The net electrode surface charge, forming the first layer, arises from adsorption of ions from the solution or diffusion of charges from the electrode surface into the solution. An electric field, emerging from this charge distribution, will in turn attract ions from the solution. The free non-absorbed ions in the solution form the "diffusive layer". The layer of surface charge together with the diffusive layer constitute the "double layer", which is characterized by the "double layer capacitance" of the interface. A consequence of the double-charge layer is the emergence of the so called half-cell potential of an electrode, which depends on the type of metal, the ion concentration in the solution and on temperature. If a current flow occurs due to an applied external (DC or AC) potential across the electrode/electrolyte interface, than a resistance must be considered to be in a parallel configuration to the above explained interfacial or double layer capacitance, when deriving an equivalent circuit model for the interface. Charges move in response to the electric field of the applied external potential, so that the net current flow across the interface is no longer zero. In the case of the equilibrium condition, where a constant flux of current occurs in both directions across the interface, the net flux is zero. Thus, an applied external potential will produce a net current flow by driving the potential out from its equilibrium value. The potential difference $V - V_{eq}$, leading to the net flow of charge across the interface, is called the overpotential of an electrode. This overpotential is built up of different contributions, which sum up to the total overpotential. The most important contributions are the charge transfer overpotential, which dominates the net current when $V - V_{eq}$ is small, and the diffusion overpotential due to diffusion of reactants to and from the electrode, which becomes important when operating more far away from equilibrium [34].

The oxidation and reduction currents per unit area at the electrode/ electrolyte interface, which are balanced and equal in magnitude, so that the net current is zero, are called the exchange current density, depending on the type of electrode, electrolyte and redox reactions. Different metals and reactions show large differences in the magnitude of the exchange current density, for example Gold in buffered saline has a value of 2 nA/cm^2, whereas Platinum or Iridium have much larger values (ca. $8\times10^{-4}A/cm^2$ and $2\times10^{-4}A/cm^2$). With the Butler-Volmer equation, the current flow through an interface in response to an applied potential near the equilibrium regime can be calculated, which depends on the overpotential and the

exchange current density. The current-overpotential curve is approximately linear at low overpotentials (<50mV) and thus the slope can be used to estimate the charge transfer resistance of the interface [34].

The charge transfer and the solution resistance are the main constituents of the resistive part of the electrode impedance for an operation near the equilibrium potential. As mentioned above, when acting at higher current densities, the diffusion overpotential comes into play, which introduces a diffusion impedance in series with the charge transfer resistance, since reactants must diffuse to the electrode interface before they undergo oxidation or reduction reactions. In the case of an alternating current, the diffusion impedance tends towards zero for increasing frequency. Warburg presented a model for the diffusion impedance, which depends inversely on the square root of the frequency of the alternating current.

The solution or electrolyte resistance is due to the spreading of current from the working electrode to a distant counter electrode in the electrolyte, the reason why this resistance is also termed spreading resistance. This purely ohmic resistance depends on the resistivity (or inversely on the conductivity) of the solution and the invers of the radius of a disc electrode (or on the square root of the invers electrode area). Since most impedance measurement cells do not have an uniform current distribution, calculation of current flow path becomes a challenge. But it is possible to determine the solution resistance from an equivalent circuit, fitted to an impedance spectrum, by introducing a resistor in series to the electrode/electrolyte interface equivalent circuit. Then the overall present solution resistance dominates the spectral electrode impedance at high frequencies.

The equivalent circuit for the electrode/electrolyte interface derived so far is known in EIS as Randles circuit and comprises a parallel configuration of the double layer capacitance C_{dl} and a faradaic process, which consists of a charge transfer resistance R_{ct} in series with the Warburg diffusion element W. This parallel configuration is in series with the solution resistance R_s. However, in order to model the experimental impedance data of the cell-free gold-film microelectrode in aqueous buffer solution (see blue lines in Fig. 2.2), the best result was obtained with a series combination of single simplified Randles circuit elements. A simplified Randles circuit includes a solution resistance in series with a parallel configuration of a double layer capacitance and a charge transfer or polarization resistance. The calculated impedance of seven of such elements in series provided a good approximation to real and imaginary part of the measured impedance of the gold-film/buffer-solution interface (data not shown). However, the physical interpretation may be difficult due to the many adjustable parameters in the equivalent circuit, which demands systematic measurements over a

broad frequency range under varying conditions, as pointed out in [35]. This was beyond the scope of this thesis, since we were concerned with measurements of cell-covered electrodes (see below).

2.3 The cell-covered electrode system

In biophysical applications electrode-solution interfaces are part of sensor devices for investigating structure and dynamics of membranes, tissues, cells, particles, suspensions etc. At least two electrodes are placed in small culture wells filled with solution. Electric fields spread across the whole volume and interact with the specimen in the culture well. Impedance (or related quantities as admittance Y, dielectric constant ε, capacitance C) measurements were conducted to study erythrocytes [36], blood [37] or cultured cell suspensions [38], yielding insights into membrane structure and its capacitance and thickness, later confirmed by electron microscopy [39]. Schwan pioneered investigations of the passive electrical properties of cells in suspension and discovered three major dispersions of the dielectric permittivity in the AC frequency regimes of kHz (low frequency), MHz (radio frequency) and GHz (microwave frequency), named α-, β-, and $\gamma-$dispersion, reviewed in [40]. At low frequencies (α-dispersion) the membrane resistance dominates, i.e. the cells act as insulating spheroids and decrease the conductivity of the suspension, from which its biomass content can be estimated [3]. As in a parallel configuration of resistance R_m and capacitance C_m, the membrane resistance is progressively short-circuited by the reactance $-1/\omega C_m$ for increasing frequencies, so that the electric field can penetrate into the cell interior. This interfacial polarization (β-dispersion) originates by charging of the membrane and thus is governed by its capacitance. The third main dispersion (γ-dispersion) arises from dipolar relaxation of water molecules [41]. Fig. 2.1A depicts the current flow around and through a spherical particle in suspension in a uniform AC electric field, showing the transition to interfacial polarization due to increasing AC frequency. Since all measurements require the use of at least two electrodes in contact with electrolyte solution, dispersions from the electrode-solution interface as well as from cell membrane systems overlap in the frequency domain. Those different contributions must be identified by firstly scanning the cell-free sensor before cells are introduced in the system.

Besides impedance measurements of cells or particles in suspension there are studies of anchorage dependent cultured cell lines, such as epithelia or endothelia, and motile cells, such as *Dictyostelium discoideum*, which make adhesive contacts to the substrate to optimize cell movement. These cell

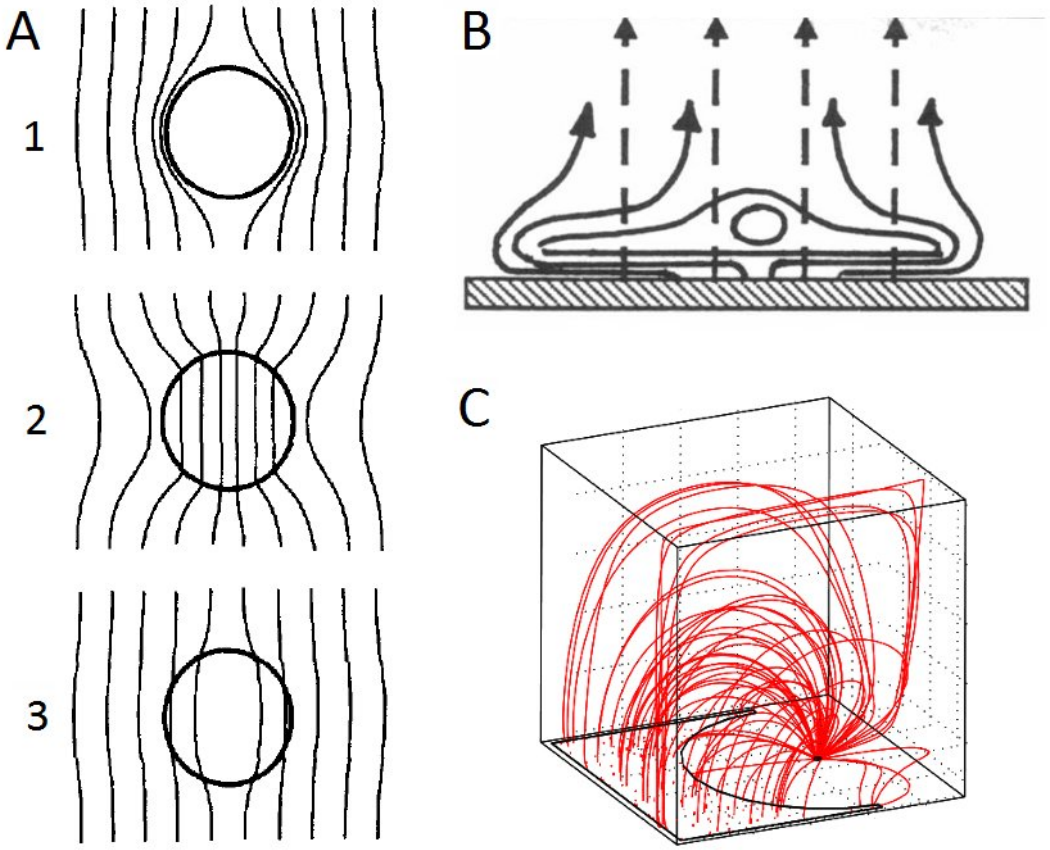

Figure 2.1 – (A) Current flow around and through a particle in suspension (reprinted from Ref. [33]). 1. For the low-frequency current the particle acts as insulating spheroid. 2. and 3. Interfacial polarization at higher frequencies. (B) Low-frequency current (solid lines) around and high-frequency current (dashed lines) through an interfaced cell (reprinted from Ref. [14]). (C) Simulation of electric field lines in a culture well with a small working electrode and a large counter electrode.

lines are studied by creating 2D-substrates with planar electrode arrangement at the bottom of culture wells. Interfaced cells spread and attach to the electrode surfaces and cover a part of these surfaces by their basal membranes, leading to an increase in impedance. At frequencies below the occurrence of interfacial polarization, the current is forced to pass the cleft between basal membrane and substrate (electrode surface) and must flow out into the bulk medium at the side of the interfaced cells (see Fig. 2.1B). This method is capable of sensing dynamic modulations of cell-substrate contacts as well as formation of cell-cell junctions as in epithelia cells by recording the time trace of the impedance. Giaever and Keese applied this technique to cultured layers of fibroblastic, mammalian, endothelial and other cell lines on microelectrodes. These electrodes were much larger than single cells, but small enough to monitor above described changes on the

nanometer level, which are not visible under a brightfield microscope. The method to increase the sensitivity of impedance measurements in the direct surrounding of the working electrode(s) is to increase the surface of the counter electrode to a multiple of that of the working electrode. In this case, the working electrode surface acts as a bottleneck for the electric field lines flowing through the whole system, so that changes due to events at the working electrode surface dominate the overall measured change in impedance.

Fig. 2.1C shows a simulation of electric field lines for a static potential distribution between working and counter electrode, with opposite but equal potentials, i.e. ϕ_{WE} = -ϕ_{CE}. Due to the smallness of the working electrode, which is surrounded by a large counter electrode, the field lines have the highest density at the surface of the working electrode (simulation was done with Comsol software). Therefore, an insulating particle placed on top of the working electrode will cause a much higher resistance than at any other place in the culture well. Geometry and dimensions of electrodes and culture well in the simulation were chosen according to commercially available Standard 8 Well Arrays from the company Applied Biophysics (see Fig. 2.2A and www.biophysics.com). Each well has a substrate area of 0.8 cm^2 and a volume of 600 microliter. A single circular working electrode (gold-film covered with a layer of insulating material with a 250um-hole) in the center of the bottom has an area of 0.0005 cm^2 and is surrounded by a 1000-fold larger counter electrode (0.5 cm^2) with a distance to the working electrode of about 3 mm.

We used an impedance analyzer device (model 3532-50 LCR HITESTER) from the company HIOKI (www.asm-sensor.com) to measure the spectral impedance of cell-free and cell-covered electrodes, using above described 8 well electrode arrays. Frequency scans were performed to test at which frequency the response of a cell-covered microelectrode to a small excitation signal (constant voltage mode with amplitude 10mV) was most pronounced. The aim was to monitor micromotion of *Dictyostelium discoideum* Wild Type AX2 cells at this frequency. It was beyond the scope of this work to perform systematic measurements of the electrode-solution interface. Also it has to be kept in mind that an electrode covered with motile cells represents a non-steady-state system. Motile cells modulate adhesive substrate contacts and continuously alter their shape, which means that the impedance fluctuates over time. Nevertheless, a frequency scan is required to reveal the frequency range of impedance dispersions caused by cells. Fig. 2.2B shows magnitude, phase, resistance and reactance of the impedance as function of frequency from 400 Hz to 30 kHz. The cell-free electrode system in Soerensen buffer as well as the cell-covered electrode

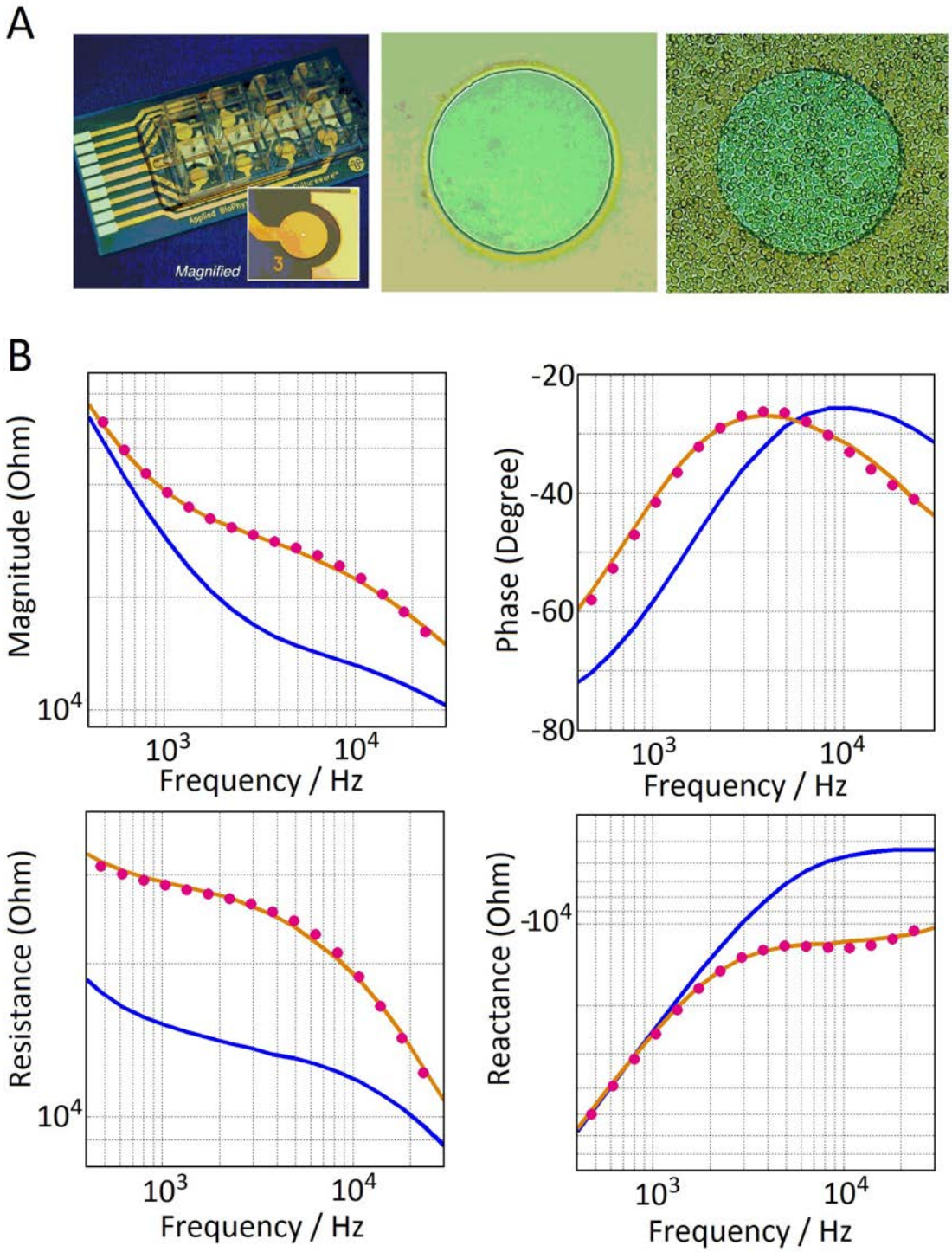

Figure 2.2 – (A) Standard 8 Well Electrode Array from the company Applied Biophysics. Cell-free and cell-covered microelectrode (⊘ 250μm). (B) Dispersion of impedance magnitude, phase, resistance and reactance of a gold-film microelectrode (⊘250μm) in buffer solution. Cell-free electrode (blue line), cell-covered electrode (orange line), impedance model (filled circles).

system with a dense layer of 3×10^6cells/cm^2 was scanned.
Giaever and Keese (References) developed a model for the specific impedance (impedance of unit area) of a cell-covered electrode, Z_c (Ωcm^2). For this model, it is assumed that the electrode is entirely covered by cells and the shape of single cells within the layer is described by a floating disc with radius r_c and cell-substrate separation h. Also, the resistance for the current flow through the paracellular space, R_b, is taken into account, which is strong for cells developing tight junctions to neighboring cells, but weak for the case of motile amoebae. For the latter case, we used the model in the form presented in [42]:

$$\frac{1}{Z_c} = \frac{1}{Z_n}\left[\frac{Z_n}{Z_n+Z_m} + \frac{\frac{Z_m}{Z_n+Z_m}}{\frac{\gamma r_c}{2}\frac{I_0(\gamma r_c)}{I_1(\gamma r_c)} + R_b(\frac{1}{Z_n}+\frac{1}{Z_m})}\right] \tag{2.3}$$

Z_n (cm^2) is the specific impedance of the cell-free electrode, which can be measured and inserted in the model after subtraction of the solution or constriction resistance R_s, which is measured in series with Z_n. Since Z_n decreases with frequency, the frequency-independent solution resistance appears in the high-frequency limit of the spectrum. Z_m (cm^2) is the specific impedance of the cell membranes and is modeled by two parallel RC-circuits in series representing basal and apical membranes, i.e.

$$Z_m = 2\left[\frac{1}{Z_m} + i\omega C_m\right]^{-1}, \tag{2.4}$$

where i=$\sqrt{-1}$ and ω=2πf; f(Hz) is the AC frequency. I_0 and I_1 are modified Bessel functions of the first kind of order 0 and 1. The important shape parameter α=$r_c\sqrt{\rho/h}$ is included in the expression

$$\gamma r_c = r_c\sqrt{\frac{\rho}{h}\Big(\frac{1}{Z_n}+\frac{1}{Z_m}\Big)} = \alpha\sqrt{\Big(\frac{1}{Z_n}+\frac{1}{Z_m}\Big)}, \tag{2.5}$$

where ρ is the resistivity of the solution, which in our case was Soerensen phosphate buffer with a relatively high resistivity of 500 Ωcm. Fig. 2.2B shows data from the impedance model (filled circles) fitted to the frequency scan data for a cell-covered electrode (as described above) by minimizing least squares errors. For a membrane capacitance of $C_m = 4.1$ μF/cm^2 the junctional resistance R_b and the shape parameter α were varied. The best result was obtained for $R_b = 5$ Ωcm^2 and $\alpha = 3.72$ $\Omega^{0.5}$cm. For this value of α the cell-substrate separation of the confluent cell layer can be calculated, which has to be considered as a mean value across all cells at the electrode

as well as across different substrate separations of the same basal membrane of a single cell. For a disc radius $r_c = 5$ μm we obtain h = 90 nm, which may be an overestimation due to the high solution resistivity of $\rho = 500$ Ωcm, which is critical for the calculation of h. The real solution resistivity may be less high due to a small amount of cell culture medium present in the electrode well after addition of cells, which has a higher conductivity than phosphate buffer. For a resistivity half as high as the value used above the calculated substrate separation will be h = 45 nm.

2.4 Cell-substrate adhesion of *Dictyostelium* cells

Adhesion and motility of eukaryotic cells is central to many biological phenomena ranging from morphogenesis and wound healing to cancer metastasis. Across many different cell types, the crawling motion of an eukaryotic cell is typically characterized by a number of essential steps including membrane protrusion, substrate adhesion, traction of the cell body and rear retraction. Among them, cell-substrate adhesion is a key factor that determines how fast and efficient cells are navigating across solid surfaces.

Adhesion of cells to surfaces involves interactions on the subcellular scale. Today, a variety of non-invasive methods are applied to study cell-substrate interactions in vivo, for a review see Ref. [43]. It is now well established that interactions of the ventral membrane with the extracellular matrix (ECM) are mediated through a large network of dynamically interacting molecules [44]. Contact sites between adhesion receptors and the ECM transduce environmental signals into the cell and cellular responses to the outside. For example, in many motile cells, focal complexes and focal adhesions link the actin cortex via integrins to the substratum [45, 46]. Understanding the dynamics of adhesion sites and its dependence on signaling events, mechanical cues, and structural factors is a major focus of current motility research, see e.g. Refs.[47, 48].

The social amoeba *Dictyostelium discoideum* has evolved into a popular model to study eukaryotic cell motility/chemotaxis and adhesion. In *Dictyostelium*, no integrin mediated focal adhesions are present. Instead, several other proteins related to cell-substrate adhesion were identified including the actin anchoring protein talin [49], the nine-transmembrane proteins Phg1 [50] and SadA [51], the disintegrin domain protein AmpA [52], and the type I transmembrane protein SibA [53].

Viewed under a brigthfield microscope, the motility of surface-attached

Dictyostelium cells comprises shape changes on the cellular scale, caused by protrusion of pseudopodia and retraction of the tail, where protrusion usually precedes retraction [54]. A single cell can perform shape changes randomly, without net displacement of the cell body. During persistent movement of chemotactic amoebae, shape changes become coordinated steps of a directed cyclic motion. Often, the movement cycle begins with a small compact cell-shape, turning into a large flat morphology during the cycle, where quasi-periodic oscillations (extensions and contractions) of the area given by the circumference of the cell are observed.

On the subcellular scale, adhesion regions establish cell-substrate contacts and are visible under a reflection interference contrast microscope [54]. The size of such areas of close contact is much larger in vegetative cells during the growth phase and strongly reduced in developed cells after 6h-7h of starvation, giving such cells the competence to dynamically form and disassemble contact sites during propagation across the substrate [54]. Also in interference reflection microscopy, actin foci â dense localized regions of increased F-actin concentration in the cell cortex â have been discovered and associated with cell-substrate adhesion in *Dictyostelium* [55]. Furthermore, traction force microscopy measurements suggested that traction forces are transmitted through these foci [55, 56]. In other studies the kinetics of shear flow-induced cell detachment of *D. discoideum* cells were investigated, giving evidence that detachment occurs by a peeling process during which molecular bonds are disrupted [57, 58].

In recent force cytometry experiments the spatial distribution of traction forces exerted by *D. discoideum* cells during their movement cycle on elastic substrata was measured [59, 60]. During the cycle the cells generate contractile pole forces in the back and front half of the cell [60], so that the cycle of actin polymerization (protrusion) and actomyosin contraction (retraction) is attended by a cycle of continuous contraction and relaxation of the substrate contact zone [59, 61]. Protrusion at the leading edge occurs when traction stress at the front is low. High traction stress at the rear inhibits protrusion [60]. Important for polarization and speed of the cell is the establishment of a traction stress distribution with front/back asymmetry [60]. In [59] it was noted that traction stress patterns in the front and back of the cell probably correspond to the adhesion regions observed in [54, 56].

In all studies cell movement appears as a highly integrated physical process, where cell-substrate adhesion plays an important role as mediator between intracellularly generated mechanical stresses and transmission of traction forces to the substratum for cell body displacement. In this context, too weak or strong adhesion hinders efficient cell movement, i.e. maximal

speed occurs at an intermediate attachment strength [62, 63]. Within this intricate attachment force adjustment also innate non-specific adhesion via cell surface glycoproteins has been suggested to play an important role for *Dictyostelium* cell-substrate adhesion [64, 65].

Besides optical methods, also electrical techniques have been employed to investigate cell-substrate interactions and play an important role in current biosensor concepts [66]. Using electric fields to sense and monitor the activity of cultured cells on microelectrodes is known as Electric Cell-substrate Impedance Sensing (ECIS) [8, 9], a common technique to perform population measurements of different processes, such as cell adhesion [67], viability [68], protrusion formation [69], and chemotaxis [70]. Cell micromotion causes fluctuations in the time evolution of the impedance. By fitting a 'floating disc' model to impedance spectroscopy data of cultured epithelial monolayers, the junctional resistance of intercellular gaps, the shape parameter and cell-substrate fluctuations on the nanometer scale could be captured [8]. Recently, collective synchronized oscillations of cell-substrate contacts during aggregation of starved *D. discoideum* amoebae were discovered, causing oscillations in the impedance [20]. Optical and acoustic methods were utilized to relate synchronous changes in cell density, morphology and cell-substrate distance to the measured time evolution of the impedance [21].

2.5 Impedance sensing in microfluidic devices

Microfluidic systems, in a wider sense, have developed to a major approach for the creation of controlled micro-environments for studying cell functions. The versatility of possible applications allows for further integration of sensors, control of bio-chemical reactions, manipulation of molecules, concentrations, surfaces, switching between tasks, processes, events of all kind, etc. Micro channels in operation can separate, merge, combine such events spatially and temporally on different scales, which shows the way for integrated multifunctional platform applications as the natural route to adapt laboratory tasks to the complex behavior of biochemical micro-systems [71].

The aim of this work was to show the principle of an electric measurement of cell migration in microfluidic chip devices. It is concerned with the integration of microelectrodes into a microfluidic channel system, functioning as impedance sensors for studying the kinetics of electrode surface coverage and substrate interactions of moving *Dictyostelium discoideum* cells by the magnitude of impedance at 4 kHz AC frequency. Impedance sensing was employed to noninvasively detect small changes in cell shape or in the cell-substratum gap, belonging to fundamentals of cell migration and motility

cycles, such as protrusion and adhesion, recorded as population average or even on the single cell level. Chemotaxis as directional cell migration is externally regulated by local asymmetries of soluble factors [23, 72]. This has motivated the creation of controllable micro-environments to provide well-defined concentration gradients [28, 29]. For our aim, to fabricate an electrical cell migration assay, we incorporated micro-electrodes in a microfluidic gradient generator. Such concentration gradient generators control diffusive transport and produce stable gradients by flow-displacement of diffusing molecules perpendicular to their diffusion flux, thus creating a range of stationary diffusive concentration profiles along the flow channel. Arbitrary shapes of profiles can be generated by splitting and mixing two or more inlet concentrations in a branched channel network, leading to a set of stepped concentrations, which, when merged in a final laminar flow stream, provide the desired stable gradient shape. Gradient generators are very useful to achieve stable gradients *perpendicular* to the direction of the flow channel.

Electric measurements of chemotaxis rates can be performed by recording impedance kinetics of the surface coverage of a single microelectrode, or by using a two-dimensional disposal of a set of microelectrodes, that is, a microelectrode array, relating time-resolved signals of different electrodes. The latter method would be in principle applicable to single cells, crossing 2D-spaced electrode stripes. The first method requires electrode overgrowing confluent cell layers, where migration speed is calculated from the temporal increase of single electrode impedance, caused by gradual decrease of conducting electrode area. Single electrode cell overgrowth was employed to design automated cell migration assays in open wells, such as wounding assays, replacing traditional scratch methods, or electric fence assays, providing a cell-free electrode surface during cell layer formation [73, 74]. We demonstrate both methods in narrow spaces of gradient chambers using impedance-sensor-based microfluidic chip devices.

The todays common method for rapid prototyping of microfluidic chip devices is soft lithography for transfer of micro channel master structures of arbitrary geometries onto the surface of the soft material polydimethylsiloxane (PDMS) by replica molding [75, 76]. The completion of the device is straight forward and consists of sealing the channel system by plasma-bonding of the patterned PDMS surface with the surface of a glass slide. For our aim, when surface-attached and moving cells have to be directly interfaced to spatially disposed planar microelectrodes, introduction of microelectrodes into the channel system is required and involves additional fabrication steps. The easiest way is to fabricate a plane electrode array by deposition of metal film electrodes on the surface of a glass slide by a

lift-off process and placing a piece of PDMS with embossed micro channels on top of that array. In this case an additional insulation layer deposition step is not required, since the electrode leads outside the micro channels are entirely covered by PDMS and electrical conductance occurs only inside the channels when filled with fluid. For chemotaxis rate measurements a suitable electrode disposal is the zebra-crossing configuration, where migrating cells have to cross a set of consecutively disposed microelectrode stripes. These electrode stripes must be placed perpendicular to the direction of chemoattractant gradient and cell movement, and it is clear, that, when using arrays without insulated electrode leads, electrode stripes should be inserted in a micro channel transversally to its direction, since then all electrode leads are covered by insulating PDMS. Using such a configuration requires a concentration gradient *in direction* of the micro channel, which is not given by the above described gradient generator. We tested another technique, which provides an elegant way to create a cAMP source, that is photo-activation of caged compounds, meaning that inert (caged) molecules cannot be recognized by cells so long as they become activated (uncaged) by photolysis [77]. Uncaging can be restricted to certain locations in a micro channel, using a focused laser beam to create a point-like molecule source, which, upon diffusion, generates a molecular gradient along the channel.

The completion of the chip device consists of interfacing and sealing of electrode-array- and PDMS-surfaces, which normally works well with air- or oxygen-plasma activation of PDMS/glass substrates. Yet another route for sealing the chip was chosen: firstly, PDMS block and electrode array were interfaced with an alignment tool and then clamped between two plastic plates to slightly press the PDMS block onto the electrode array with small equal forces from every side. This technique was also employed by other authors, see for example [78]. It has the advantage that electrode arrays can be repeatedly used, provided that the PDMS block can be removed after measurement, which is possible when electrode leads are stable enough. Another advantage is that spring contact pins can be mounted into the upper plastic plate for contacting electrode pads on the edge of the chip, making the use of a separate device for electrode tapping dispensable.

With the described methods we performed chemotaxis rate measurements of small clusters of *Dictyostelium discoideum* wild type AX2 cells with an impedance-based cell migration assay. The recorded velocities of migration lie in the range of 5 - 20 μm/minute. The versatility of the technique allows further development and integration of micro-laboratory tasks into the chip device and we propose an advanced fabrication technique for a compact electrode arrangement in microfluidic channels.

2.6 The aim of the thesis

Frequency scans shown in Fig. 2.2B were performed to test at which frequency the response of a cell-covered microelectrode to a small excitation signal (constant voltage mode with amplitude 10mV) was most pronounced. Fig. 2.2B shows that the cell layer produced a remarkable increase of the magnitude of impedance (compared to the cell-free electrode impedance) at frequencies ranging from 1000 Hz to 20 kHz, with a maximal difference at about 4000 Hz. The magnitude of impedance is given by the ratio of effective values of voltage and current. If additionally the phase shift ϕ between voltage and current is measured, the impedance can be broken down in resistance R=|Z|cosϕ and reactance X=|Z|sinϕ, representing the 'in-phase' and 'out-of-phase' components of the complex impedance. The frequencies where resistance and reactance are most different from those of the cell-free system, are 2000 Hz and 10-20 kHz, respectively, i.e. the reactance acts at higher frequencies. The measured impedance can be interpreted as the signal of a resistor and capacitor in series, where the overall capacitance as function of frequency, C(ω), can be calculated from the capacitive reactance X(ω)= -1/ωC(ω). In Wegener et al. 2000 it was shown that the kinetics of the overall capacitance at 40 kHz is the most suitable measure for monitoring the increasing electrode surface coverage due to cell spreading, because of the linear dependence of this kinetics on the electrode coverage [**?**]. The focus and aim of our work however was to monitor micromotion of single motile *Dictyostelium* cells on microelectrodes. Some test experiments showed that a single cell on a 50um×50um square microelectrode covers only 5 -15% of its surface and that this small surface coverage produced no remarkable phase shift between voltage and current. The kinetics of the magnitude of impedance however displayed rapid fluctuations due to micromotion and larger fluctuation amplitudes for cell lines with stronger substrate interactions. Therefore, the magnitude of impedance at 4000 Hz was chosen as the measure for single cell recordings presented in this work. The current response of the electrode system was measured via transimpedance amplifiers. Operational amplifiers are used to amplify small excitation signals.

3 MATERIALS AND METHODS

3.1 Experimental setup

For measuring the cell-substrate impedance a custom-made cell-substrate impedance sensor (CSIS) was developed using commercially available electronic parts including DAQ hardware (NI PCI-6120 board, National Instruments, München, Germany) and a data processing platform (LabVIEW, National Instruments, München, Germany), see Fig. 3.1. The key part of the device is a microelectrode array interfacing the cells to the DAQ hardware. For single cell recordings microelectrode arrays (MEAs) from Multi Channel Systems (Reutlingen, Germany) were used, with 59 $50\mu m$-TiN-square-electrodes, and ECIS cultureware 8W1E DD PET (Applied Biophysics Inc., Troy, New York, USA), an eight-well-array containing eight circular gold-film electrodes with four different diameters, two of which with $\oslash 50\mu m$ were used. A 4kHz-ac-signal with voltage amplitude 10mV was applied to the counter electrode and the current ($< 1\mu A$) was measured at the working electrode using a current-to-voltage converter made of a TL071CP operational amplifier (Texas Instruments Inc., Dallas, USA) and a 560 kOhm metal oxide resistor. Amplitudes of analog input/output signals V_{in} and V_{out} from the CSIS were converted and sampled with DAQ hardware at sampling frequency 4 MHz and displayed and stored with LabVIEW software. With the current V_{out}/R and Ohm's Law the impedance was calculated as $Z = V_{in}/I_{out} = R\ V_{in}/V_{out}$.

MEAs were mounted into a MEA1060UP interface kit (Multi Channel Systems, Reutlingen, Germany), or alternatively, if eight-well-arrays were used, into a custom made interface. Cells on MEAs were observed with an upright microscope (IX61, Olympus) or an inverted microscope (IX71, Olympus) when eight-well-arrays were used. The inverted microscope was equipped with a XM10 (Olympus, Tokio, Japan) camera. Both types of MEAs were equipped with culture chambers to accommodate cells and culture medium on top of the microelectrodes. Measurements of the complex impedance $Z = |Z| \exp(i\Delta\phi)$ require the measurement of voltage $|V_{in}|$, current $|V_{out}|/R$ and phaseshift $\Delta\phi$ of voltage and current caused by the impedance of the sample. In Ref. [17], it was demonstrated that the kinetics of the real part of Z, the resistance, acts most sensitively to cell-substrate or

intercellular interactions of an established cell layer at frequencies 1-10 kHz, whereas the imaginary part, the reactance resp. capacitance, acts upon the establishment of a cell layer at frequencies >10 kHz, i.e. when cells attach to the electrode-electrolyte-interface. Therefore, for single cell-substrate interaction measurements, the phaseshift was neglected and the kinetics of the magnitude of Z recorded at 4 kHz (at this frequency, the observed change of |Z| due to cell micromotion was the strongest, see Fig. 2.2B). The kinetics of impedance and timelapse brightfield microscopy of selected single *D. discoideum* cells were simultaneously recorded to assess possible correlations between impedance fluctuations and shape changes of the cell.

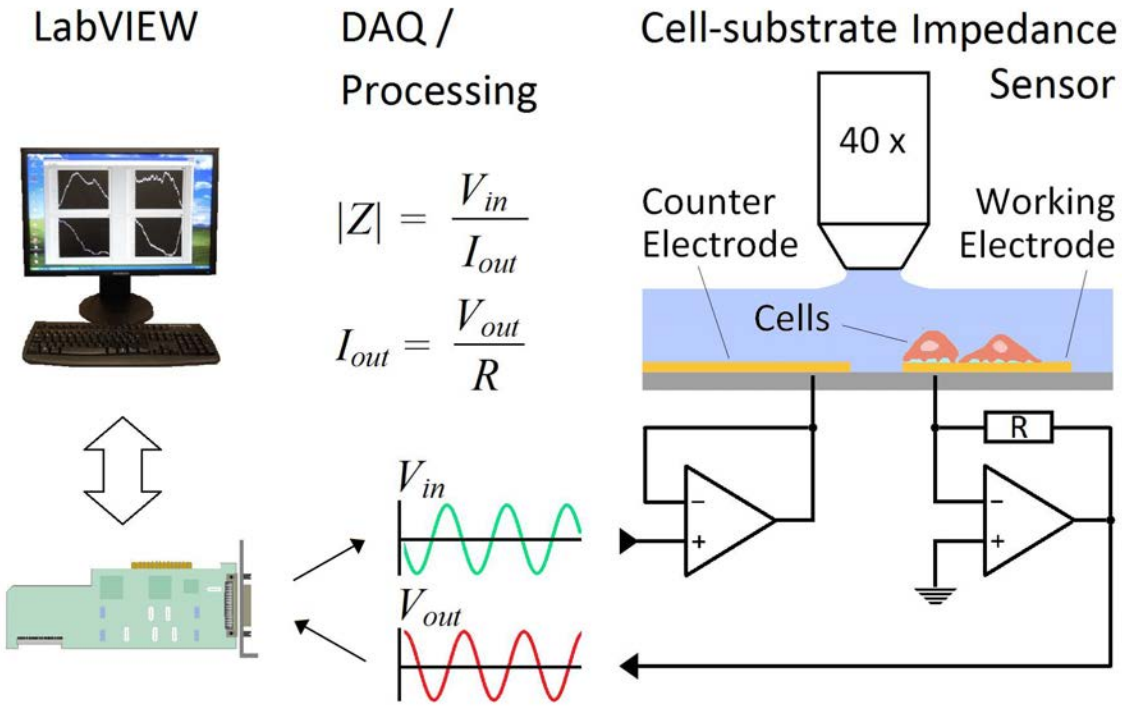

Figure 3.1 – Experimental setup. A voltage signal, controlled by LabVIEW software, is applied to the counter electrode of the Cell-Substrate Impedance Sensor (CSIS) and the current measured at the working electrode by a current-to-voltage converter. The impedance is given by $Z = V_{in}/I_{out}$.

3.2 Data processing and analysis

To capture shape changes of a cell, we determined the time evolution of the projected area of a cell on a two-dimensional surface. Images were processed with an edge-detecting algorithm, which finds and fills the closed contour of the cell. We then subtracted the background and performed binary thresholding. Computing the pixel variance of the binary images yielded a white cell surrounded by a black contour line. The contour lines

were then closed by further increasing the pixel variance. Finally, the area within the closed-contour objects was filled.

To extract the characteristic periods of shape oscillations of a cell (motility cycle period) from impedance data, we implemented the continuous *wavelet transform* resp. its time-scale representation, the *scalogram*, in Matlab (MathWorks Inc., USA), using the Morlet wavelet. A similar approach has been used earlier to analyze oscillatory dynamics during starvation-induced cAMP signaling in *Dictyostelium* [79]. First, each time series of raw impedance data was wavelet transformed. In a second step, its time dependence was removed by element summation of the scale-columns in the scalogram. The resulting time-averaged scalograms displayed several characteristic peaks which were assigned to particular persistent scales. The peak corresponding to the lowest oscillation period was selected to determine the motility cycle periods as shown in Fig. 4.5.

The magnitude of impedance fluctuations was quantified by calculating the standard deviation of impedance signals after linear trends were removed, see Fig. 4.6 A.

3.3 Cell culture and mutant strains

The cell lines used in our experiments were *Dictyostelium discoideum* AX2-WT cells (kindly provided by R. Gräf, University of Potsdam) and the mutant strains *tal*A$^-$ (dictyBase-strain ID: DBS0236177), *nap*A$^-$ (dictyBase-strain ID: DBS0236597), *amp*A$^-$ (dictyBase-strain ID: DBS0235493), which were ordered from the *Dictyostelium* Stock Center [22]. The AX2-derived *GFP-α-tubulin* expressing strain was kindly provided by G. Gerisch (MPI of Biochemistry, Martinsried, Germany). Cells were grown from frozen spores by incubation in HL5 medium (*Foremedium*) for three up to four days at 20°C. Cells were then transferred into culture flasks containing HL5 medium until a cell density of 2×10^6 cells per ml was reached. Finally, all cell lines were inoculated at 5×10^5 cells per ml in 25 ml HL5 medium and grown on a shaker at 150 rpm and 20°C for about twenty hours.

3.4 Detachment assay

Cell-substrate adhesion of wild type cells and mutant strains was assessed by a detachment assay as described in Refs. [80, 81], exposing cells to fluid shear stress. 3 ml of cell suspension at a density of 8×10^5/ml were filled into a six-well plate made of polysterene (Sarstedt AG, Nümbrecht, Germany) and cells were allowed for 10 minutes to sediment and attach to

the bottom of the wells. The final cell density in each of the six wells was $2.5\times10^5/\text{cm}^2$. The plate was shaken at 150 rpm and after 0, 5, 15, 30, 45 and 60 minutes of shaking the supernatant medium was replaced by fresh HL5 medium. Detached cells in the supernatant medium were counted using a haemocytometer. The percentage of detached cells of a well was calculated by summing up all cells counted up to the indicated time points and dividing the sum by the number of attached cells at time point 0 min. Finally, means and standard deviations of the calculated percentages of the six wells of a plate were taken. Results are shown in Fig. 4.6 E.

3.5 Single Cell Force Spectroscopy

As a further method to assess the substrate adhesion strength of single cells, we used an AFM-based single cell force spectroscopy (SCFS) (Asylum MFP-3D, Asylum Research) setup with a 30 mm z-range. We functionalized a tipless cantilever (Arrow TL2, NanoWorld, fo=6 kHz, k = 0.03 N/m) with CellTack®(1:30 diluted with 1mM $NaCO_3$) and immobilized a single cell at the front of the cantilever by picking. After a regeneration time of 2 min, we pressed (trace) the cell with a velocity of 2.5 μm/second and a force of 0.5 nN against an untreated, ethanol cleaned glass surface for 30 seconds. We repeated this cycle up to 20 times, with a regeneration time of 30 seconds between each cycle. Cells were measured in the interval from 0h to 3h after exchange of medium to phosphate buffer. As a result, a characteristic force-distance-curve was obtained, from which the maximal adhesion force F_{max} could be extracted. Results are shown as boxplots in Fig. 4.6 D.

3.6 Fabrication of microelectrode arrays

The performance of electrical impedance measurement in a microfluidic channel system with conducting fluid requires the use of planar microelectrodes, consisting of thin metal layers with a thickness typically less than 100 nm. A single counter electrode serves as the common pole of the active electrodes and has to be placed in close proximity to them. The geometry and disposal of the electrodes must be constructed in a way that the active part of the array forms - together with the microfluidic channel placed on top - the measurement cell, where the current flow between counter electrode and working electrodes takes place.

For the fabrication of arrays of planar microelectrodes a high accuracy and homogeneity must be achieved concerning the geometry of closely

positioned electrodes and the electrode surfaces. The method we use in our laboratory appropriate for manufacturing thin metallic films on a solid substrate such as dia-glass is 'sputter coating' and belongs to the group of processes termed 'physical vapor deposition'. These methods work at pressures far below the atmospheric pressure, i.e. they operate in a high vacuum environment, in which a vaporized metal is deposited atom by atom onto a solid substrate. This provides the required accuracy in manufacturing micro-structured planar electrodes.

Sputtering means the ejection of particles from the surface of a solid target due to bombardment of the target surface by energetic particles. The energetic particles are generated in an evacuated chamber by ionization of atoms of an inert gas such as Argon. The ionization is achieved by an electric field, where the target serves as cathode and the substrate opposite to the the target as anode. The constituents of the plasma, Ar^+-ions and electrons, are accelerated towards the target and the substrate, respectively. The impingement of Ar^+-ions and subsequent ejection of the target atoms is a physical process driven by momentum exchange between projectiles and target atoms and can be used for deposition of the sputtered target material. The ejected target atoms are accelerated towards the substrate and will condense over its surface. Important parameters for the whole process are the cathode current, the discharge voltage, the process pressure and the distance between target and substrate [82].

The sputter coater we use in our laboratory is the K575X model from Quorum Technologies Ltd. (Ashford, UK), which employs a magnetron target assembly, i.e. it uses electric and magnetic fields to confine plasma ions close to the target surface, which leads to more ionizing collisions and thus makes the process more efficient. Two targets can be used to deposit two-layer coatings without opening the evacuated chamber. Noble targets as well as targets which need pre-cleaning to remove oxide layers can be used. A shutter assembly allows the cleaning and coating cycle to be executed while maintaining the vacuum. The vacuum system consists of a turbo molecular pump backed by a rotary vane pump. Even depositions are achieved by a rotating sample table and the gas pressure can be controlled by a gas bleed needle valve.

The desired microstructuring of electrodes is established by combination of the sputtering process with a lift-off technique, as widely used in microtechnology, for example for patterning of integrated circuits in semiconductor device fabrication. Often a light-sensitive material, a photoresist, is used in the lift-off process, which, upon selective light exposure through a photomask, becomes structured with soluble and unsoluble regions, thus giving an excellent patterning down to smallest features. The photoresist

we use in our laboratory is the SU-8 series from the company microchem (MicroChem Corp., Westborough, USA, german distributor: Micro Resist Technology GmbH, Berlin, Germany), which we use for manufacturing microfluidic systems in combination with soft lithography. SU-8 photoresist is designed for micromechanical systems (MEMS) fabrication, but has also applications in bio-MEMS due to its biocompatibility. It is an epoxy-based negative photoresist, i.e. near UV (350-400 nm) exposure causes cross-linking and polymerization of the material. The SU-8 2000 series is available in different viscosities, allowing coatings with film thicknesses ranging from 0.5 μm to more than 200 μm. Usually, the processing steps include 1. The coating of the cleaned and dried substrate by a spin coater, where the coat thickness is regulated by the spin speed. 2. The soft bake for solvent evaporation and for making a solid stable layer, which can be a critical step due to stress formation causing cracks. The heating is done on a level hot plate, performing a 65°C step followed by ramping to 95°C to reduce stress formation. After pre-baking the coated substrate is slowly cooled down to room temperature. 3. The exposure of the solid layer to UV light, where the exposure time depends on film thickness and exposure dose. Patterning is performed using a photomask placed into close contact to the layered substrate. During exposure the cross-linking of the material begins with photoacid generation by interaction of the photons with the salt in the layer. 4. The post exposure bake (PEB), during which the final epoxy cross-linking and polymerization occurs, a process termed curing, which is thermally driven and catalyzed by the acid produced during the exposure step. The PEB is also done via ramping from 65°C to 95°C. 5. Development of the unexposed, soluble regions of the resist layer, where development time depends on the film thickness (SU-8 Developer). For finishing the development process the substrate with the patterned layer has to be rinsed with Isopropanol and air dried. Depending on the final use of the patterned coat a further cross-linking and curing of the layer is achieved by a hard bake. Before we present the reader a detailed list of the whole process of microelectrode array fabrication, we give a brief description of the used instruments and devices in our microstructure laboratory. The sputter coater is described above. For photoresist UV exposure we use the PRX 2000-20 Exposure System (TAMARACK scientific co., inc., Corona (California),USA), which is designed to provide ultra violet illumination in the band width of 350 nm to 450 nm over the target area. Illumination is by a 2000 Watt high pressure mercury arc lamp, whose beam is directed into an optical system consisting of a Rhodium coated ellipsoidal reflector, two mirrors which reflect UV and pass unwanted IR, a homogenizer assembly, a filter and aperture assembly and a collimating reflector. Exposure timing

electronics and lamp power supply complete the system. The high pressure mercury arc lamp provides the important wavelength for SU-8 exposure, the i-line (365 nm) in the near UV.

The plasma cleaner we use is the model PDC-002 (HARRICK PLASMA, Ithaca, New York). Generally, the interaction of plasma with a surface include the processes ablation, i.e. the removal of surface contaminants by electron and ion bombardment, and activation, i.e. the creation of surface chemical functional groups and dissociation and reaction of a plasma gas with the surface. These processes makes a plasma useful for cleaning and pretreatment of surfaces for the use of photoresist coating and for bonding, i.e. creation of a tight seal between PDMS and a glass slide when fabricating microfluidic devices. Plasma process gases are for example Air, Oxygen, Argon, Nitrogen or Hydrogen. The use of plasma for vapor deposition is described above.

Further important devices for substrate pretreatment and subsequent photoresist coating are the spin coater model WS-400BX-6NPP/LITE (Laurell Technologies Corporation, North Wales, USA), used for even photoresist depositions with defined coat thickness, a temperature controlled Precision Hot Plate model 1000-1 (PI-KEM Ltd., Staffordshire, England) and a Ultrasonic Cleaner (HBM Machines, Moordrecht, Netherlands).

In the following we give a detailed list of the process steps for fabrication of microelectrode arrays as shown in Fig. 3.2:

1. Substrate Preparation

Dia-glass, 49×49 mm, 1 mm thick, was cleaned in an Isopropanol and subsequent deionized water bath in an Ultrasonic cleaner for 10 min each and dried with a stream of nitrogen. For a better photoresist adhesion the glass slides were sputter coated with a very thin non-conducting layer of Titan.

2. Coat

The smallest features of the electrode design on the photo mask were 50 microns. Photoresists from the SU-8 2000 series were used. Initially, the SU-8 2025 photo- resist was tested with coat thickness of 25 microns (spin coating speed: 3600 rpm), but due to the usage of a polyester photo mask without an expensive mask aligner it was much easier to work with the SU-8 2005 photoresist, which achieves a thickness of 5 microns at 3000 rpm, thus an aspect ratio of 1/10. Before spin coating, the glass substrates were heated on a hotplate at 200°C for 15 minutes and air-plasma cleaned for 80 seconds, which gives a smooth coating. Spin coating then was performed with the following steps: 1. Dispense of about 1.5 ml of resist for a 49×49 mm glass substrate. 2. Spin at 500 rpm for 10 seconds with acceleration of 100 rpm/second. 3. Spin at 3000 rpm for 40 seconds with acceleration of

250 rpm/second. After spinning the coated substrates were stored in petri dishes for 30 minutes to allow relaxation of the resist layer. The Pre Bake then was performed on the level hotplate at 65°C for 1.5 minutes, followed by ramping up to 95°C at 2.5°C/10 seconds with the subsequent Soft Bake at 95°C for 3 minutes.

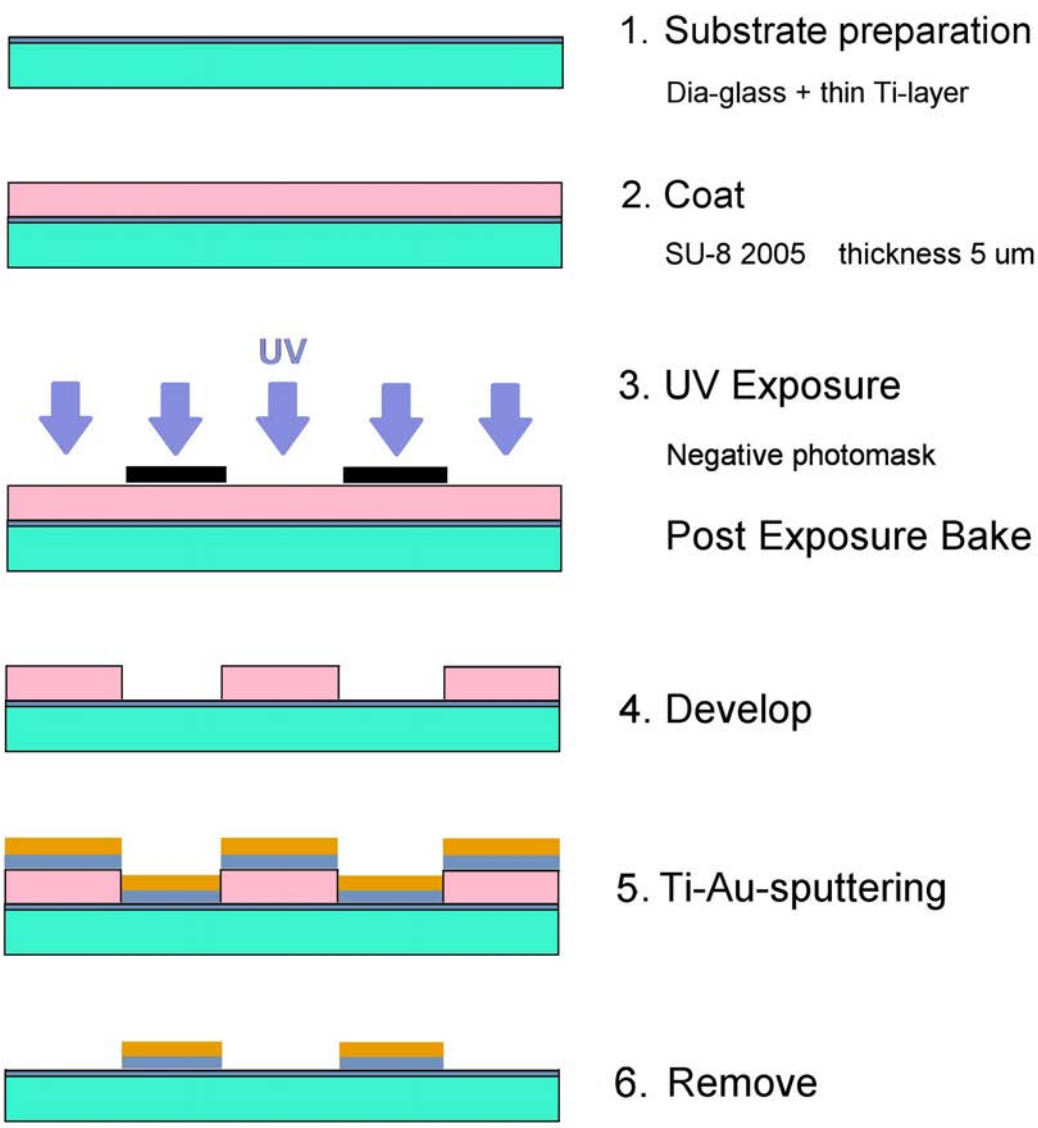

Figure 3.2 – The six steps of microelectrode array fabrication. Details are explained in the text.

3. Expose and PEB

After cooling down to room temperature the stable solid resist layer was ready for UV exposure. The coated glass substrate was stably positioned on a paperboard and the polyester photo mask was super-imposed to it and fixed on the paperboard with tape. Finally a heavy quartz glass plate was

laid on the photo mask to press it against the resist film. The UV lamp exposure dose of about 125 mW/cm^2 was measured with an UV sensor. The recommended total exposure energy according to the Processing Guidelines of the SU-8 2000 series is about 100 mJ/cm^2 for a coat thickness of 5 microns, i.e. an exposure time of 0.8 seconds was selected according to the formula 125 mW/cm^2 $\times$ 0.8 sec = 100 mJ/cm^2. After exposure the samples were heated again to 65°C on the level hotplate, followed by ramping up to 95°C at 2.5°C/10 seconds with the subsequent Post Exposure Bake (PEB) at 95°C for 4 minutes. Shortly after the onset to 95°C the pattern of the resist layer became visible.

4. Develop

The development of the resist layer after the PEB process was done with MicroChems SU-8 developer in a suitable beaker. For a thin resist layer of 5 microns a development time of 1 minute was sufficient. Also it was no problem to perform the development step hours or even some days later than the PEB step. After development the samples were rinsed with Isopropanol and dried on a hotplate at 65°C for about 2 minutes.

5. Ti-Au-sputtering

The electrode pattern was checked under an inverted microscope. Sometimes small microparticles of any material were located on the electrode structure, leading to defect patterns when deposited with gold. In most cases, a strong stream of nitrogen was sufficient to remove the particles. After this check the samples were ready for sputtering. A Titan film was sputtered, layered by a Gold film of about the same thickness. The final thickness of the 2-metal film was 10-20 nm according to the sputter times used.

6. Remove

For removing the non-developed regions of the resist layer with the 2-metal film on top, the samples were placed in glass dishes and covered with MicroChems remover 660-rem. After some minutes it was visible that the resist layer detached. After 20 hours the resist was entirely removed, the electrode arrays were rinsed with Isopropanol to stop removing and dried on a hotplate at 65°C.

A microelectrode array fabricated according to the six steps described above is shown in Fig. 3.3.

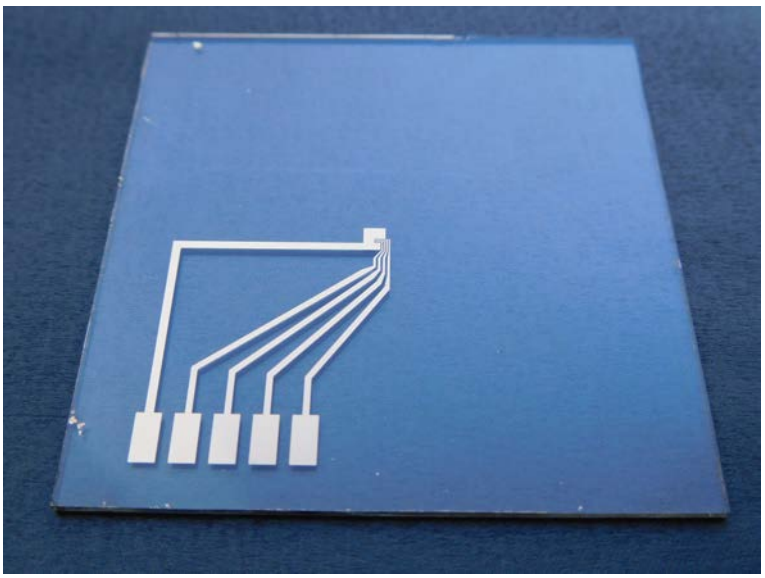

Figure 3.3 – Microelectrode array on 49 × 49 mm Dia-glass with one counter electrode and four working electrodes.

3.7 Microfluidic channel systems - from the idea to the master mold and PDMS replication

A microfluidic gradient mixer device consists of a small block of solid material, in which a system of channels and small chambers, with cross sectional areas of about $0.001 - 0.1$ square millimeters, is located with terminal connections to the outside of the block, allowing the fluid supply of the channels with at least two different concentrations of one or more chemo-attractants, which then are mixed by the channel system and joined together in a terminal chamber to produce a temporally stable gradient of chemo-attractant, which than can be used for further applications. A continuous flow ensures the maintenance of the gradient. Typically, to fabricate sealed micro channel structures, two surfaces, the solid material surface bearing the micro structure and a plain surface of the same or another solid material, must be brought together. But the first important step of the fabrication is: how can a desired pattern, drawn with a suitable computer program, be brought as a microstructure onto the surface of the solid material? This task is the subject of this chapter. The sealing of the channel system, which is usually made by plasma bonding between the micropatterned surface and a glass slide, marks the final step in microfluidic device fabrication and is described in the next chapter.

Soft lithography techniques are widely used to complete the task of surface micropatterning for microfluidic device fabrication, in that photo-

lithography, used to create a master structure on a wafer, is complemented by transmitting the (negative) master structure onto a surface of a soft material. The material of choice is Polydimethylsiloxane (PDMS), a silicon elastomer, which is poured in liquid form (mixed with a cross-linking agent) onto the wafer master structure. Heating at 75°C will cross-link and cure the liquid PDMS, thus giving it the outstanding properties suitable for application in microfluidics: viscoelasticity (which means that cured PDMS can be removed from the wafer without destroying the micro-structure; waterproofed tube connections and handling of complicated channel systems with high aspect ratio is possible), biocompatibility, transparency, bonding to glass or PDMS. Also, adhesion to plain surfaces of various materials is a useful property (see next chapter) and the fact that, at small scale, the cured PDMS is solid enough to bear a microstructure for a long time without damaging [83].

In the following we list a detailed protocol for the fabrication of a microfluidic channel structure on the surface of a block of PDMS:

1. From drawing of the micropattern to the completed photomask

The first event is the idea of a pattern, which then is drawn on a CAD file with a suitable computer program. The CAD software we use is Dip Trace (Novarm Ltd., Dnepropetrovsk, Ukraine), an advanced printed circuit board design tool, allowing the creation of schematic diagrams ranging from centimeters at full extension to a few microns at the smallest scale. Zooming in and out allows for the exact positioning of all parts of the diagram. The finished diagram is exported as a Gerber file as the standard input format for photoplotters, used for the fabrication of photolithography masks. We send our Gerber files to the company JD Photo Data (Hertfordshire, United Kingdom) to order a flexible film photomask consisting of a polyester PET base with a soft photographic emulsion gel film, which, after exposure and development, turns black and reveals the opaque structures. The unexposed areas are washed out clear and represent the transparent structures. Emulsion film photomasks have limited resolution, but have the important property of low cost compared to quartz glass masks.

2. Fabrication of a master structure on a silicium wafer by photolithography

With the photomask on hand the process started with the fabrication of a master structure on a silicium wafer. Before spin coating, the silicium wafer was heated on a hotplate at 200°C to remove water molecules. Then ca. 3 ml of the photo resist SU-8 2050 was spin coated (see the last chapter for a description of the spin coater used) at 500 rpm for 10 seconds with

acceleration of 100 rpm/second and then at 1630 rpm for 30 seconds with acceleration of 250 rpm/second. The spin speed was calculated for SU-8 2050 resist to achieve a layer thickness of 100 microns. For relaxation of the resist layer the wafer was left on the spin coater for ca. 15 minutes. Afterwards the Soft Bake step of the process was performed at 65°C for 5-10 minutes and subsequent ramping up to 95°C at 0.2°C/second and baking at 95°C for 20 minutes. UV-exposure was performed as in the case for microelectrode array production. The photomask was laid on the cooled resist-coated wafer and a heavy quartz plate was positioned on top of the mask. According to MicroChems datasheet the recommended exposure energy for a 100 microns resist film is about 240 mJ/cm^2. As in section A the UV lamp intensity was measured and the exposure dose calculated and experimentally tested. Finally an exposure time of 2.6 seconds was used. In the subsequent Post Exposure Bake the image of the structure appeared shortly after the wafer was placed on the hotplate. The PEB step was performed for 5 minutes at 65°C, followed by ramping up to 95°C at 0.2°C/second and baking at 95°C for 10 minutes. Then the resist film was developed for 10 minutes with MicroChems SU-8 Developer. Finally the master structure was further hardened in a Hard Bake step for about 1 hour at 95°C.

3. PDMS soft lithography replication of the master mold

The soft lithographic step comprises the transmission of the master structure to the surface of the soft material PDMS. For that, the viscous PDMS was mixed thoroughly with a crosslinking agent to cure the PDMS. The ratio of the mixture was 1:10. The wafer with the master mold was placed on the bottom of a plastic dish and PDMS was poured into the mold. The next important step was the remove of air bubbles arising from the mixing step, for which an exsiccator with a connected vacuum pump was used. The degassing step was performed for at least half an hour. After that the air bubbles were completely removed and the PDMS was transparent as glass. Then the hardening of the PDMS on the mold was performed in an oven at 75°C for about two hours. Once the PDMS was hardened, it was cut in the desired block-forms, with one channel structure in the middle of every block. Then single PDMS blocks were carefully stripped from the wafer, the wafer was cleaned with isopropanol and ready for further preparation of series of PDMS blocks. As a result transparent blocks of PDMS were obtained with the micro-channel structure on the surface stripped from the wafer.

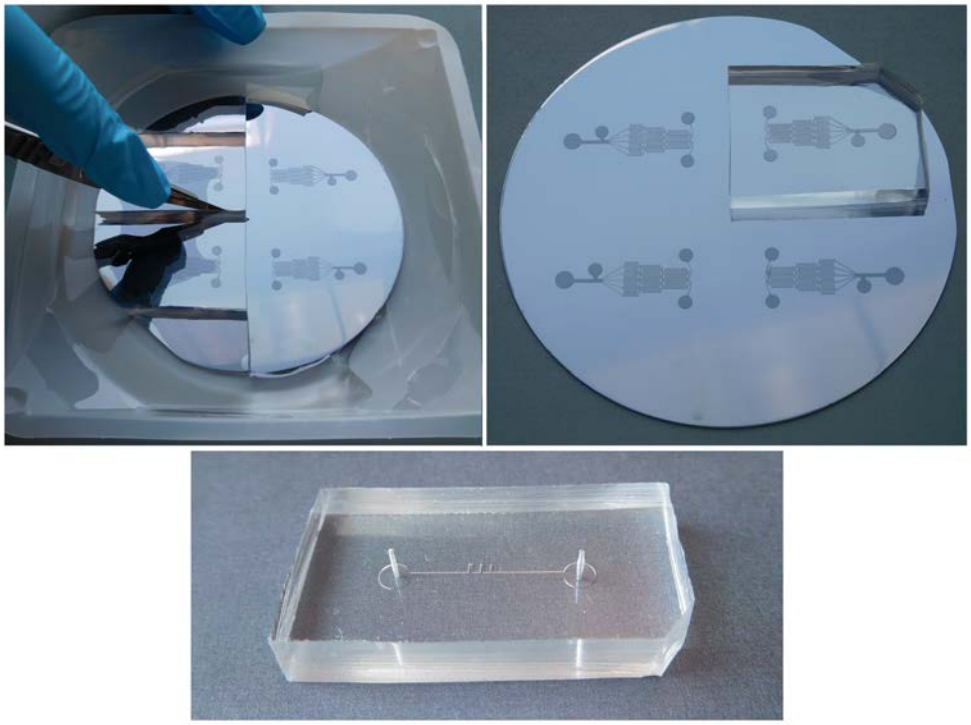

Figure 3.4 – Pieces of PDMS patterned by replica molding.

3.8 Microfluidic concentration gradient generators

Microfluidics has become a major approach to generate spatially and temporally stable gradients of diffusible substances due to its capability to handle small volumes of fluid in a controlled environment. A lot of interesting papers to this subject were published since the beginning of the new millennium [29, and references therein]. The interplay of advective and diffusive transport processes, described by the Peclet number, is utilized to maintain a stable molecular gradient in a microfluidic channel. When laminar flow streams with different concentrations of a substance flow side-by-side in a common micro-channel, then diffusion of molecules perpendicular to the direction of flow leads to an equilibrium state with a homogenous concentration of molecules across the channel, where a gradient cannot be maintained any longer. But due to the flow, there is a position downwards the channel, where advective and diffusive transport will maintain a non-equilibrium state, leading to a stable gradient at this position. Therefore, when joining several of such laminar streams in a common channel, it is possible to generate a stable linear gradient, when successive higher concentrations of the substance are provided by consecutive streams. A step gradient at the beginning of the channel will turn by diffusion to a stable linear gradient at a position downwards the channel.

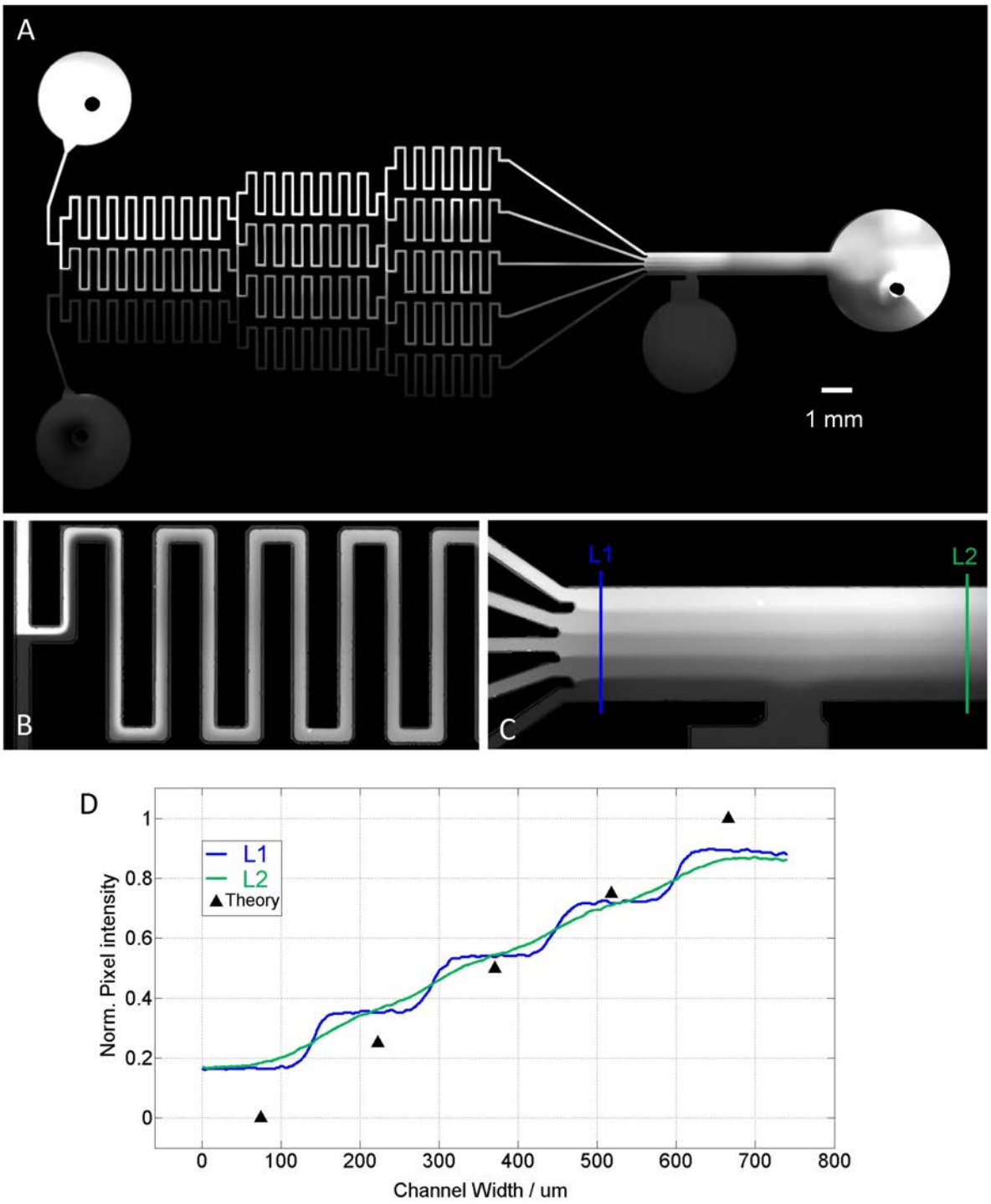

Figure 3.5 – Microfluidic concentration gradient generator. (A) Mosaic composed of 32 photographs with fluorescin under UV illumination. (B) Detail of the branched channel network. (C) Main channel with gradient. (D) Normalized pixel intensity measured at indicated positions shown in C. Theoretical concentrations (symbols) calculated with the formula in the text (without diffusion).

The next question is how to generate successive increasingly concentrations of a substance. Using separate fluid-inlets for every concentration would be a too elaborate and difficult task. But there was developed an

elegant way to overcome this problem (see papers mentioned above) by introducing a tree-like branched network of micro-channels, where two channels with a low and a high concentration are mixed in consecutive cascades to obtain at the end a set of channels with intermediate concentrations, which then are joined together in a final broad channel where the gradient is generated.

The microfluidic gradient generator we used for our experiments was originally introduced in [84] and is shown in Fig. 3.5, which is a mosaic image composed of 30 transparent overlapping photographs. The microfluidic chip was fabricated as described in section 3.7. The sealing of PDMS block and a glass slide was done by plasma bonding after punching 0.5 mm-holes in the two inlets and the outlet by a cannula. The upper inlet was supplied with a 1:100 dilution of fluorescin and phosphate buffer, the lower inlet with buffer only. The velocity of the flow was maintained at 4 μL/minute by a syringe pump, which corresponds to a velocity of 0.9 mm/second in the broad main channel with a cross sectional area of 740×100 μm. The chip was placed on an inverted microscope and photographs of fluorescin intensity taken with a camera.

The principle of gradient generation was described in the above mentioned papers and can be understood from the following principles: every mixing cascade consists of horizontal serpentine channels of the same length. A cascade with n serpentine channels is followed by a cascade with n+1 serpentine channels. Vertical channels in between the cascades consist of either splitting units ($\dashv$) or combining units ($\vdash$). All serpentine channels end in a splitting unit. The split flows are then combined to a single channel flow except the two outermost flows. To which ratios the flows are divided can be calculated from the fact that the resistance to fluid flow is the same within every serpentine channel of a cascade, which means that the same volume flow is transported through the channels. For a cascade with n channels, 1/n of the entire volume flows through every channel, where in the next cascade with n+1 channels, 1/(n+1) of the entire volume flows through every channel. Because of the symmetry, the splitting of the middle channel of a cascade with an odd number of channels is the same downwards from the splitting unit than upwards. When B denotes the number of serpentine channels of a cascade and V = 0,. . .,B-1 labels a single serpentine channel of this cascade, then the volume flow portion downwards from the splitting unit is given by (B-V)/(B+1) and the flow portion upwards is given by (V+1)/(B+1). These rules can be used to calculate the concentrations of substances within every channel of the network. For the gradient generator of Fig. 3.5 with two initial concentrations c_1 and c_2 at inlet 1 and 2, the following formula can be used to calculate the concentrations of a cascade

from the concentrations of the previous cascade. The outermost serpentine channels of a cascade have always the concentrations c_1 (bottom) and c_2 (top). If B>2 denotes the cascade with n=1,...,B serpentine channels, than for the concentrations C_n(B) it holds:

$$
\begin{aligned}
n = 1 : &\qquad C_1(B) = c_1 \\
n = 2, \ldots, B-1 : &\qquad C_n(B) = \tfrac{n-1}{B-1} C_{n-1}(B-1) + \tfrac{B-n}{B-1} C_n(B-1), \\
n = B : &\qquad C_n = c_2,
\end{aligned}
$$

starting with the inlet concentrations $C_1(2) = c_1$ and $C_2(2) = c_2$. The theoretical concentrations for B=5, $c_1 = 0$ and $c_2 = 1$ are presented in Fig. 3.5, together with the experimental values from two indicated positions in the main channel. The pixel intensity corresponding to the highest fluorescin concentration was normalized to 1. Important for the generation of a stable linear gradient is to maintain the right flow velocity, so that a complete mixture of the combined concentrations in the serpentine channels is achieved, with a homogeneous concentration at the end of the channel. As mentioned above, the used velocity was 0.9 mm/second. This velocity corresponds well with the value of 1 mm/second reported in [84], where the main channel of the gradient generator has a similar cross sectional area than that shown in Fig. 3.5.

3.9 Sealing the channel system

Once the micro channel pattern is brought onto the surface of the PDMS material, it must be sealed by joining the PDMS surface with another surface, usually glass. The glass surface then serves as the bottom of the channel system, walls and ceilings are given by the patterned PDMS material. A tight seal between the glass and PDMS surface is established by low pressure plasma bonding. We use the plasma cleaner described in section A to activate the surfaces by an air plasma. Before plasma treatment the glass substrates were cleaned with an Ultrasonic cleaner in an isopropanol bath, rinsed with deionized water and dried with a nitrogen stream. The surfaces of PDMS and glass were exposed to air plasma for about 80 seconds and joined together immediately after plasma exposure. This procedure of sealing microfluidic chips works very well if PDMS and pure glass surfaces are used.

In the case of an impedance based microfluidic chip with integrated microelectrodes the glass substrates are replaced by electrode arrays. Since the microelectrodes must be placed in a designated location of the micro channel system, the patterned PDMS block must be exactly positioned on top of the electrode array when sealing the channel system. This means that a device must be constructed, which allows the insertion of the PDMS

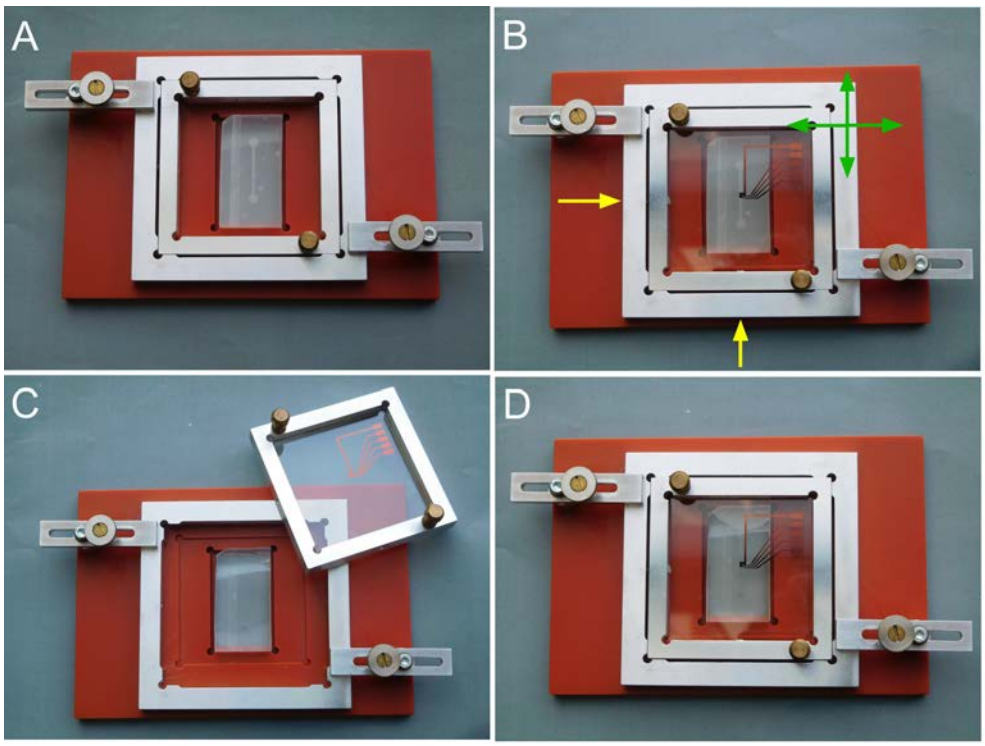

Figure 3.6 – Tool for alignment of microelectrodes in microchannels. (A) The patterned piece of PDMS with tape on its surface is clamped in a hollow of the bottom plate. (B) The electrode array is placed on top of the PDMS block and fixed to the inner frame by plastic screws (yellow arrows). The metal frames can be moved on the plate to find the right position. Then the outer frame is fixed by two brackets. (C) The inner frame is removed, the tape on PDMS is stripped off. The outer frame holds its position. (D) The inner frame can be reinserted. Now array and PDMS are aligned and can be removed from the tool.

block as well as the electrode array into two parts of the device, which both can be entirely placed in the plasma cleaner and which can be quickly joined together after plasma activation of both surfaces. If the two parts of the device are assembled, the PDMS block and the microelectrode array are automatically joined together in an accurate position. Such an alignment tool is depicted in Fig. 3.6. It consists of three parts: 1. a bottom plate with a centred rectangular well, in which the PDMS block can be stably positioned. 2. An outer metal frame, which can be clamped and fixed by two screws to the bottom plate. 3. An inner metal frame, which can be inserted in the outer frame. First, the PDMS block with the channel structure upwards is placed in the well and the frames positioned so that the PDMS block lies within the inner frame. Then the electrode array is placed with the electrode structure downwards on top of the PDMS block, which is sealed with transparent tape. The array can be fixed to the inner frame with plastic screws, which are tightened with a small screwdriver through holes in the outer and inner frame. The structures of PDMS block

and array are aligned by moving the frames and fixing the outer frame to the bottom plate when finding the right position. Finally the inner frame can be removed from the outer frame and the tape stripped from the PDMS block. When plasma bonding is the selected way of sealing the chip, then both parts, the inner frame with the clamped array and the bottom plate with the fixed outer frame are placed together in the plasma chamber. After surface activation, the inner frame will be inserted in the outer frame again, so that the electrode array is located in the desired position on top of the PDMS block. The sealed and bonded chip then can be released from the tool by unloosening the plastic screws. We fabricated the low cost alignment tool in our own workplace. The accuracy of alignment accounts to 10-20 microns if the device is handled carefully.

3.10 Connecting transimpedance amplifiers

As mentioned above, the plasma bonding establishes a tight seal between the PDMS surface and a glass slide. However, this was not always the case when a microelectrode array instead of the glass slide was used, probably due to contaminants on the surface of the micro-electrode array, stemming from the fabrication process of the array. This problem could be partly compensated by sputtering an additional non-conducting thin Titan layer on the array surface, which improved the formation of tight bonds after plasma activation, but this made the procedure of sealing the chip more complicated. So we looked for another technique of sealing, which was used for example in [78] and which utilizes the adhesion property of PDMS to a flat surface. If a PDMS block is placed on a dried surface, the adhesion of the rubber-like PDMS material suffices to establish a waterproofed seal to the surface. This seal of microfluidic channels can be breached by the fluid flow if the fluid pressure is high enough, but this problem can be solved by smoothly pressing a stable plate on top of the PDMS block, which has the advantage that the PDMS block can be removed from the electrode array after the experiment, allowing the repeated usage of electrode arrays. This technique can be combined with the connections of the electrode leads to the impedance amplifier circuit.

Fig. 3.7 shows the whole measurement setup with the microelectrode array, the PDMS block on top of the array, two Plexiglas-plates for pushing together array and PDMS block and the spring contact pins for the connections to the transimpedance amplifier circuit. The upper Plexiglas-plate is fixed by eight screws to the lower plate, allowing the balancing of the pushing forces exerted to the PDMS block from every side by tightening the screws. The five spring contact pins are custom-built models from the

company INGUN (INGUN Prüfmittelbau GmbH, Konstanz, Germany).

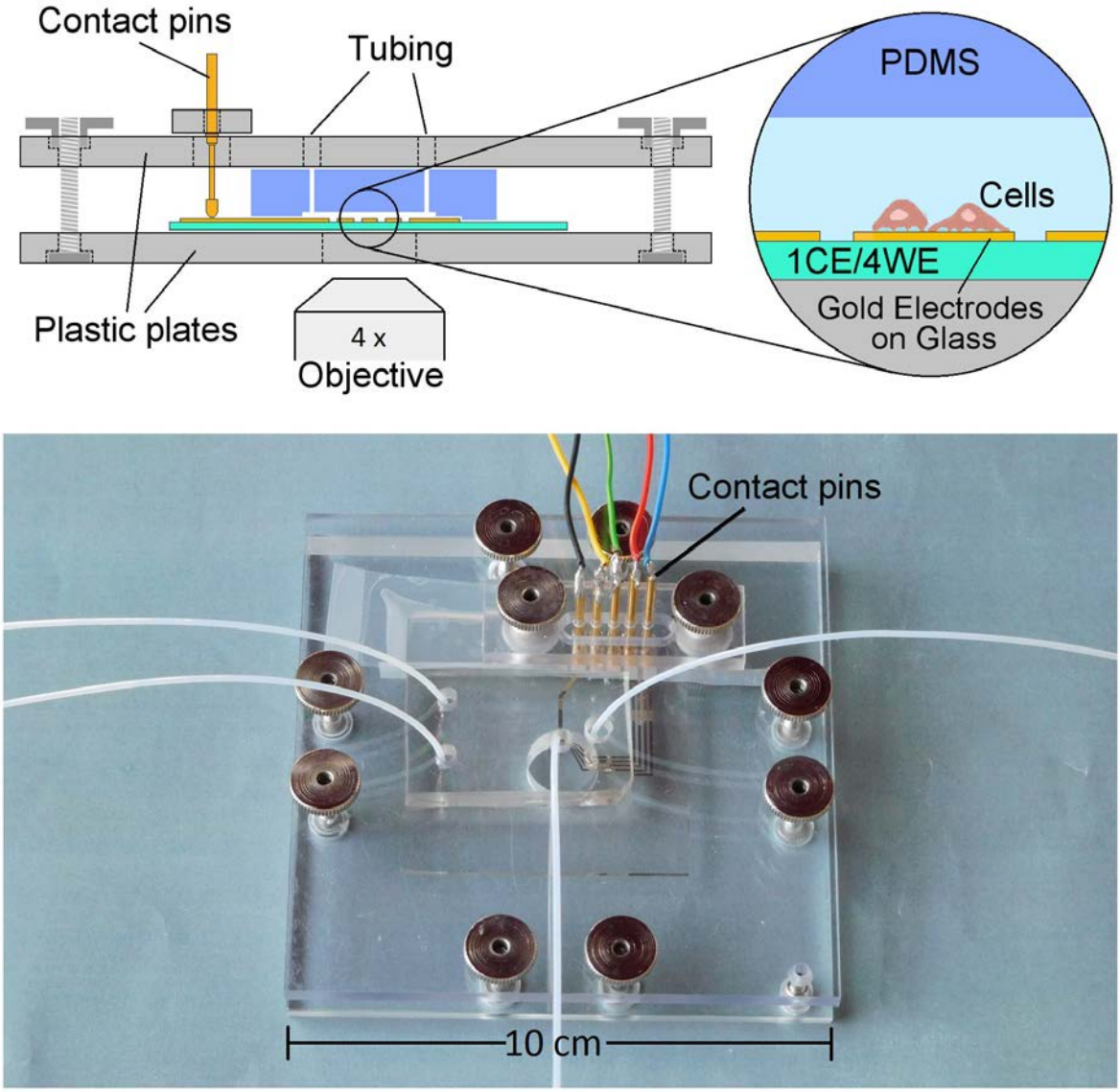

Figure 3.7 – Clamp tool for a waterproofed sealing of the chip. Sketch with magnified chip interior (side view, not to scale). CE: counter electrode, WE: working electrode. Photograph with tubes (top view). Spring contact pins in the upper plate contact electrode pads at the edge of the chip.

The contact pins are plugged in five small holes in a separate piece of Plexiglas, which is mounted on top of the upper Plexiglas-plate by two screws. The pins are inserted through a slot in the upper Plexiglas-plate and pushed to the contact pads on the electrode array at the lower plate. Short cables are soldered in holes at the topside of the pins and are connected to impedance amplifier circuit by small pin connectors. A hole in the lower Plexiglas-plate allows for observation of the micro-channel system of the chip by an inverted microscope.

3.11 Compact electrode arrangement in microfluidic channels

Cell-substrate impedance sensing of planar microelectrodes interfaced by cells requires high density of electric field lines on working electrode (WE) surfaces compared to the density on the counter electrode (CE), which therefore must have a much larger surface area than that of working electrodes. This is due to the problem that the counter electrode must be placed in the same measurement chamber than that of working electrodes and that normally many cells are placed on the CE surface when filled in the measurement chamber. Hence, the contribution of the counter electrode to the overall measured impedance must be reduced, which is achieved by increasing the surface area. These conditions impose requirements on the performance of impedance measurements in microfluidic channels, such that the space of the measurement cell must have a minimal size, adapted to the impedance of the electrode system used. This means that the height of the micro channel must be the larger, the smaller the size of electrodes and the larger the spacing of CE and WE.

With respect to easiness of fabrication, all electrodes can be placed on the bottom of a micro channel by using arrays of planar electrodes on a glass slide and by placing a piece of PDMS with embossed micro channels on top of that array. But in the next step it is straight forward to think about the compactness and miniaturization of the measurement cell with respect to its size and electrode arrangement. The fabrication technique presented in this chapter deals with the spatial arrangement of working and counter electrode, which may be called 'electrode sandwiching', meaning that the counter electrode is placed in vertical opposition to the working electrodes. The working electrodes remain at their position on the bottom of the micro channel, whereas the counter electrode is decoupled from the electrode array and reinserted in the chip as the ceiling of the micro channel. Such a compact metal/liquid/metal electrode configuration is realized by the following fabrication steps:

1. The counter electrode is fabricated by vapor deposition of a thin gold film onto the plain surface of a piece of PDMS. Some papers deal with fabrication of electrodes on PDMS, for example [85–87]. Sputtering on PDMS is problematic, since charged metal ions cause tensions and deformations on the PDMS surface, leading to fine cracks and wrinkles in the sputtered metal film, which increases the electrical resistance. The best result was obtained by plasma cleaning of the PDMS surface and subsequent vapor deposition of a thin gold film, which works without charged particles.

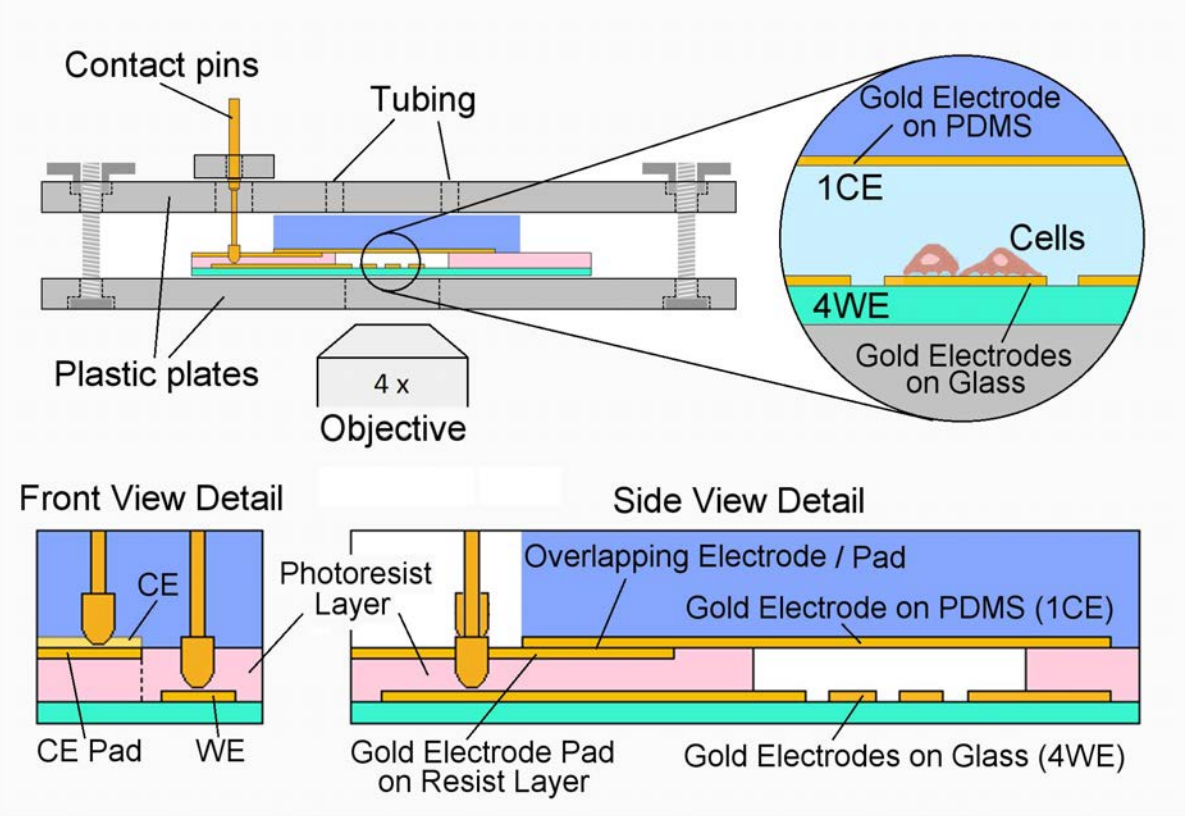

Figure 3.8 – (Not to scale) Clamp tool as shown in Fig. 3.7, but with a chip with compact electrode arrangement. The counter electrode (CE) is deposited on the PDMS surface and forms the ceiling of the microchannels. Channels are given by a patterned resist layer on the array surface. The counter electrode is contacted via a gold pad on the resist layer, which has an overlapping region with the counter electrode. Front and side view depict the details.

2. A microelectrode arrays is fabricated as described in section 3.6, but without a counter electrode. The array is entirely coated by a SU-8 resist layer and the micro channel pattern is embossed into the layer via photo lithography. After development of the resist layer, the active parts of electrodes are exposed on the bottom of a micro channel, whereas non-active parts (electrode leads) are covered by the insulating resist layer. Electrode pads on the edge of the array are also exposed by resist development of a rectangle, containing all four electrode pads.

3. To seal the micro channel system, the piece of PDMS with gold film is placed on the resist coated and patterned electrode array. To tap the counter electrode at the edge of the chip, a stripe of gold is sputtered onto the resist layer, which is partly covered by the piece of PDMS, so that an overlapping region is created between the electrode stripe on the resist layer and the gold film on the PDMS surface. The exposed gold stripe at the edge of the chip, which is not covered by PDMS, can be tapped by a spring contact pin.

A sketch and photographs of a chip with compact microelectrode arrangement are shown in Fig. 3.8 and Fig. 3.9.

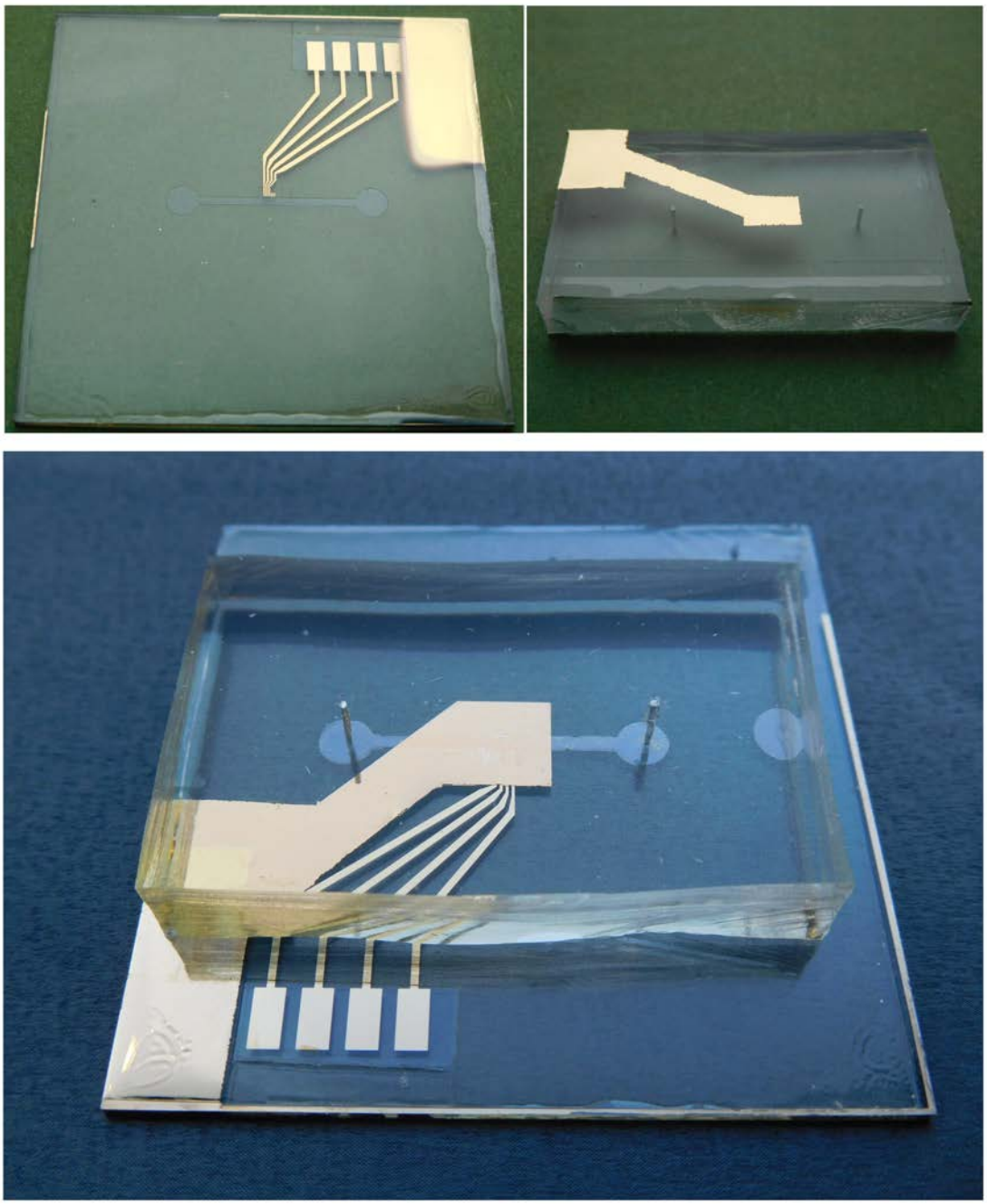

Figure 3.9 – Chip with compact electrode arrangement. Electrode array with micropatterned photo resist layer. Electrode leads are covered by the resist layer. Active parts of electrodes are exposed. A stripe of gold on the resist layer serves as contact pad for the counter electrode (top left). A piece of PDMS with deposited counter electrode (top right). The completed chip. A part of the counter electrode and the gold pad have an overlapping region which allows to contact the counter electrode (bottom).

3.12 Photo uncaging

In the field dealing with the absorption of light by matter, photo uncaging represents a highlight of the efforts, to synthesize, handle or prepare substances at the molecular level for the spatiotemporal control of specific chemical reactions. As described in this chapter, photo uncaging is also a very useful method to provide cells with spatially and temporally well-placed chemotactic stimuli.

Initially, messenger molecules (cAMP in the case of *Dictyostelium discoideum*) are present as caged compounds in the required concentration in the bulk medium. The cage is a protecting group bound to the messenger molecule, which prevents the binding of the molecule to the receptor on the cell surface, i.e. the cells cannot sense it. The next step is the controlled light-induced breaking of the bond between cage and compound, a process called photolysis. Here, the energy $E = h\nu$ of the photon(s) must fulfill the resonance condition for absorption of light, i.e. it must match the excitation energy of the molecule due to the discrete nature of its excited states [88]. Once the molecule is brought by photon energy absorption into an electronically excited state S_1 or S_n (n>1), it firstly will return to the lowest vibrational state v_0 of the electronic state S_1 by a photophysical process like internal conversion (IC) or intersystem crossing (ISC), as can be inferred from the known Jablonski diagram [88, page 26]. IC and ISC are radiationless processes. A return to the ground state S_0 can only occur from this lowest vibrational state of S_1 (rule of Kasha) by a photophysical or by a photochemical process. Since photo uncaging yields a product that is chemically different from the original reactant, it belongs to the group of photochemical processes. In general, the probability that a molecule undergoes a defined process after absorption of a photon is given by the quantum yield $\Phi_x(\lambda) = n_x/n_p$, that is the amount n_x of photochemical events x divided by the number of absorbed photons n_p at the irradiation wavelength λ.

The caged compounds used in our experiments are the axial and equatorial diastereomers of the 7-[bis(carboxymethyl)-amino]coumarin-4-ylmethyl (BCMACM) esters of cAMP [89]. Fig. 3.10 shows the structure of the molecules. The caged compounds photorelease cAMP upon one- as well as two-photon excitation and are highly resistant to spontaneous hydrolysis in the dark. The single-photon photochemical quantum yields as well as the extinction coefficients (given by the Beer-Lambert law) are high for the caged compounds, resulting in excellent photosensitivity at long-wavelength irradiation. Even moderate UV/Vis irradiation is sufficient to obtain large amounts of free cAMP [89]. Photoactivation of the axial or equatorial di-

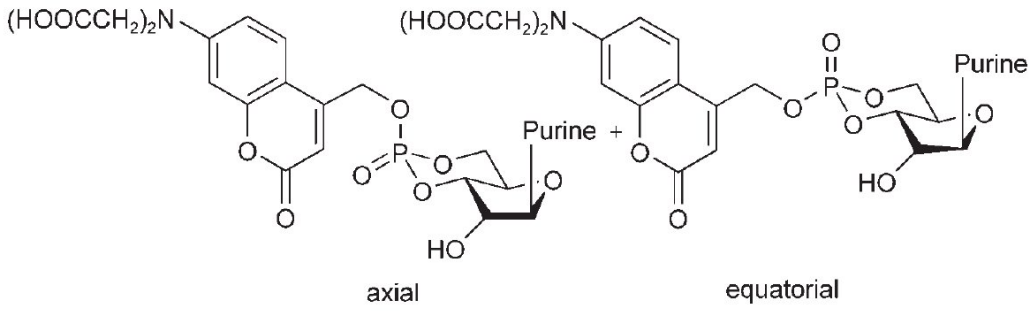

Figure 3.10 – cAMP as caged compound: BCMACM esters, the purine derivative is adenin.

astereomers by irradiation with wavelengths of 330-430 nm in aqueous buffer leads to the 7-[bis(carboxymethyl)amino]-4-(hydroxymethyl)coumarin, a proton and the respective free cAMP anion [89].

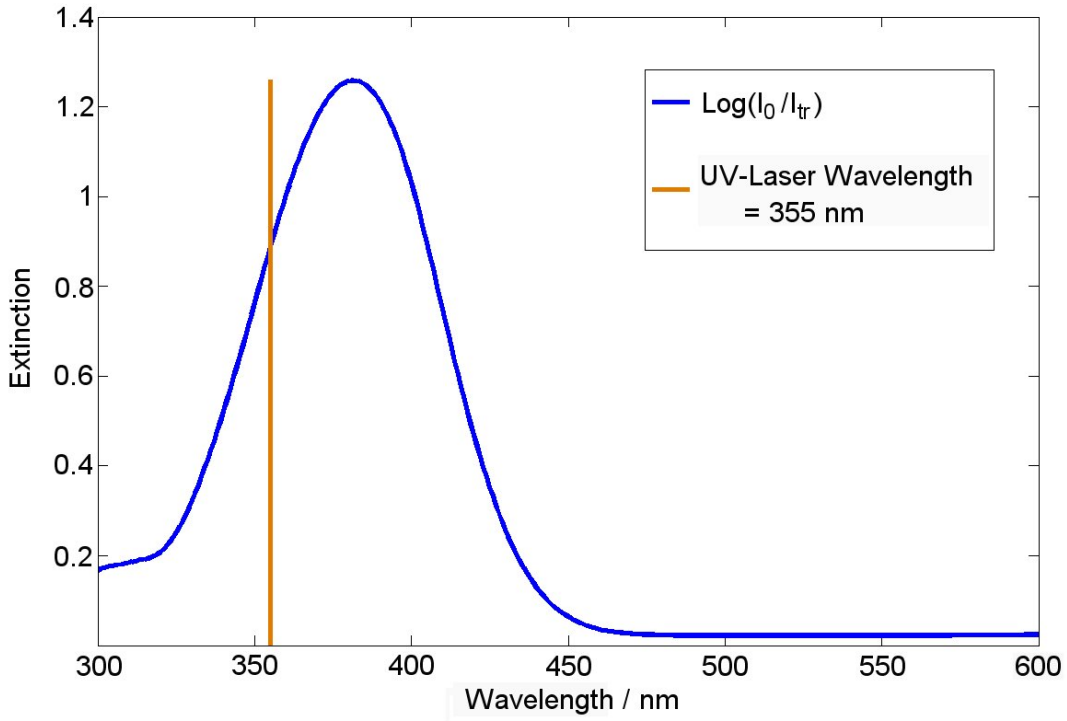

Figure 3.11 – Extinction spectrum for BCMACM-cAMP, measured in Soerensen buffer (pH=6.0) with a spectrophotometer (concentration c=100 μM, thickness d=1 cm). The vertical line indicates the UV wavelength λ=355 nm used in experiments for photo uncaging.

Fig. 3.11 shows the extinction curve for wavelengths 300-600 nm, measured in Soerensen buffer (pH=6.0) with a spectrophotometer (Cari 5000, Agilent Technologies, Victoria, Australia). The concentration of the sample was c=100 μM and its thickness d=1 cm. The vertical line indicates the

355 nm-wavelength of the UV-laser, which we used in our experiments (see RESULTS section). The laser beam was focused through the 4x objective of an inverted microscope and directed into a micro channel through the bottom glass slide of a PDMS-glass-chip, so that only a small local region of a micro channel was irradiated with UV light. Cells in the micro channel were outside of this region, so that caged compounds inside of cells were not uncaged from the laser beam. For imaging cells and channels visible dark red light with wavelength 690 nm from a polychromator was used.

4 RESULTS

4.1 Single cell measurements

In this section, we will present impedance time series of single amoeboid cells on microelectrodes. In the absence of cells, the current flow between working and counter electrode is only restricted by the bulk electrolyte resistance. Cells partly covering the working electrode surface cause a measurable increase of the impedance due to their insulating membranes, i.e. the coverage of the electrode surface reduces the area available for current flow. While motile *Dictyostelium* amoebae spread and attach on two-dimensional surfaces, they undergo morphological changes from a small round shape to a large flat shape and vice versa. Protrusion of pseudopods followed by retraction of the cell's tail constitute the basic steps in amoeboid motility. During protrusion, the projected area of the cell increases and during retraction it decreases. We will show that such cyclic morphological changes are reflected in similar oscillations of the impedance kinetics. However, we will also provide evidence that the observed oscillations and fluctuations in the impedance kinetics do not arise solely from changes of the projected area of a cell. In addition, nanometer variations of the cleft between the cell's ventral side and the electrode surface, possibly related to the formation of adhesion sites, strongly affect the impedance signal.

4.1.1 Time evolution of the projected area and the overall trend of impedance data correlate

In Fig. 4.1 A and B, impedance measurements of vegetative wild type and *tal*A$^-$ cells are shown. All measurements were carried out on identical goldfilm electrodes (diameter 50 μm, Applied Biophysics, Troy, New York, USA) under identical conditions. During measurement, the cells were imaged using an inverted microscope to capture variations of the projected cell area. Between 1 and 3 cells were located on the electrode surface while the impedance was recorded for 80 minutes (upper line in Fig. 4.1A and B). The projected cell area was calculated as described in subsection 4.1.3.

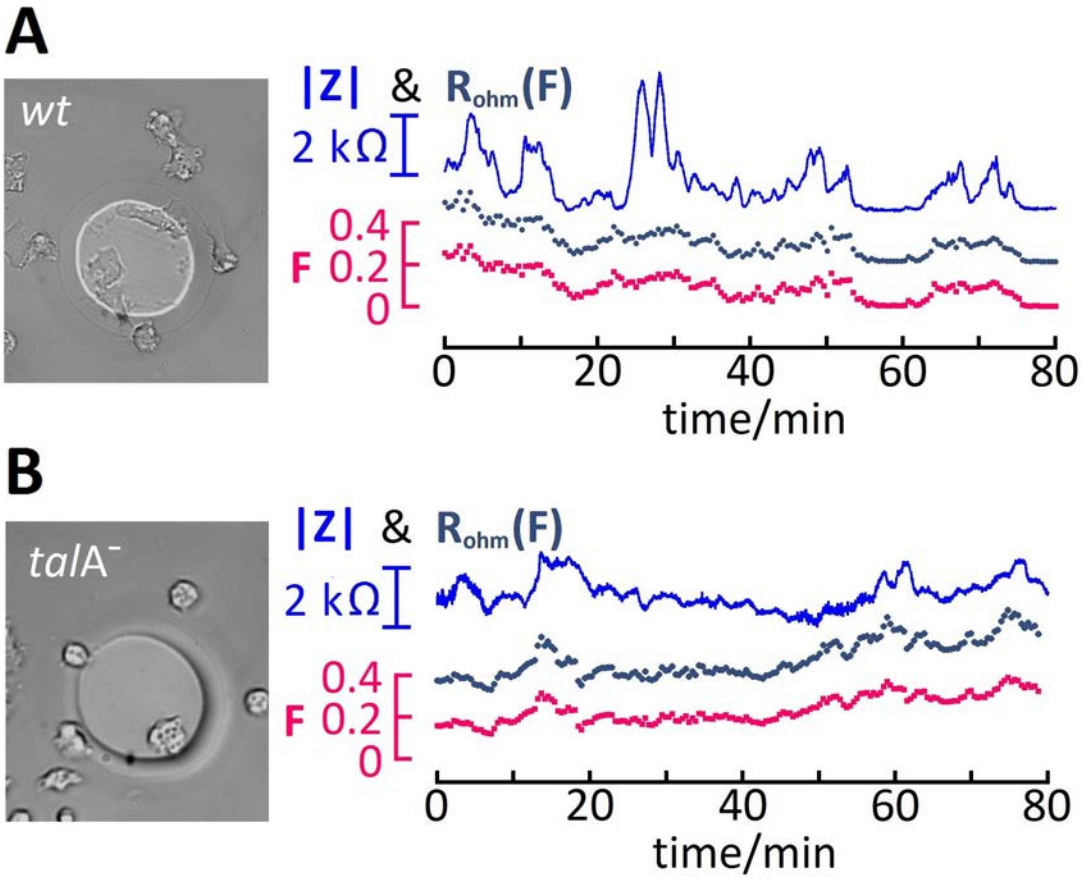

Figure 4.1 – Time evolution of impedance |Z| (upper line), modeled ohmic resistance $R_{ohm}(F)$ (middle line) and normalized projected area F (bottom line) for AX2-WT (A) and *tal*A$^-$ cells (B).

Quantity F shows the ratio of the projected area and the electrode surface area (bottom line in Fig. 4.1 A and B). Comparison of impedance data and corresponding F-values reveals that the slow irregular oscillations of |Z| resemble those of F (on a timescale of several minutes), i.e. F appears as the underlying trend in the time evolution of the impedance. To quantify this observation, we computed correlation coefficients $C = \mathrm{Cov}(|Z|, F)/\sigma_{|Z|}\sigma_F$, where Cov(.,.) is the covariance, σ is the standard deviation and thus $C \in [-1, 1]$. For the data of AX2-WT and *tal*A$^-$ mutants given in Fig. 4.1 A and B the computed correlation coefficients were C(WT) = 0.66 and C(*tal*A$^-$) = 0.43. Thus, both data sets show positive correlation in the time course of impedance and normalized projected area.

To reveal the dependence of the impedance on the projected cell area, we used a classical electro-stationary model introduced in Ref. [90] to calculate the ohmic potential in the vicinity of a small disc electrode. In this model, the interaction of a cell with its substrate, notably the formation of sites of close contact, is not explicitly taken into account. Thus the corresponding

parameter, the cell-substrate distance h, can be considered as constant in this model. The total ohmic resistance can be calculated from Ohm's law and depends inversely on the electrode radius r_0:

$$R_{ohm} = \frac{1}{4\kappa r_0} \tag{4.1}$$

where κ is the solution conductivity. If one or more cells cover a part of the surface area A of the disc electrode, then the effective electrode area A*, where current flows directly in the bulk medium, reduces to A*=(1-F)A. If a radius r* is assigned to the reduced area,

$$r* = \sqrt{\frac{(1-F)A}{\pi}}, \tag{4.2}$$

then the ohmic resistance depends approximately linearly on the projected cell area F:

$$R_{ohm}(F) = \frac{1}{4\kappa r*} = \frac{\sqrt{\pi}}{4\kappa\sqrt{A}}\frac{1}{\sqrt{1-F}} \approx \frac{\sqrt{\pi}}{4\kappa\sqrt{A}}\Big(1+\frac{1}{2}F\Big). \tag{4.3}$$

As shown in Fig. 4.1 A and B, time courses of modeled ohmic resistance $R_{ohm}(F)$ and normalized projected area F are proportional, so if there is a positive correlation between the measured impedance |Z| and F, there is also a correlation between |Z| and $R_{ohm}(F)$. Based on this observation, we conjecture that long-term oscillatory trends in the impedance data are mainly related to changes in the projected cell area.

4.1.2 A cell line that is deficient in cell-substrate adhesion shows reduced impedance fluctuations

We also observed in the data shown in Fig. 4.1 A and B that AX2-WT cells produced fluctuations in |Z| that are higher in magnitude than those of *tal*A$^-$ cells — a mutant that is known to be strongly defective in substrate adhesion [49]. We quantified this observation by computing standard deviations of AX2-WT and *tal*A$^-$ impedance time series from Fig. 4.1 A and B. Before taking the standard deviations, the lowest oscillatory trend was removed from data by subtracting a polynomial fit of second order. We found that fluctuations in the time series of impedance measured for AX2-WT were about twice as large as those of *tal*A$^-$ cells; σ(WT) = 826 Ohm and σ(*tal*A$^-$) = 447 Ohm. The projected area of AX2-WT cells is smaller or equal to that of *tal*A$^-$ cells in Fig. 4.1 A and B. Therefore

changes in the size of the projected cell area cannot be the cause of larger impedance fluctuations.

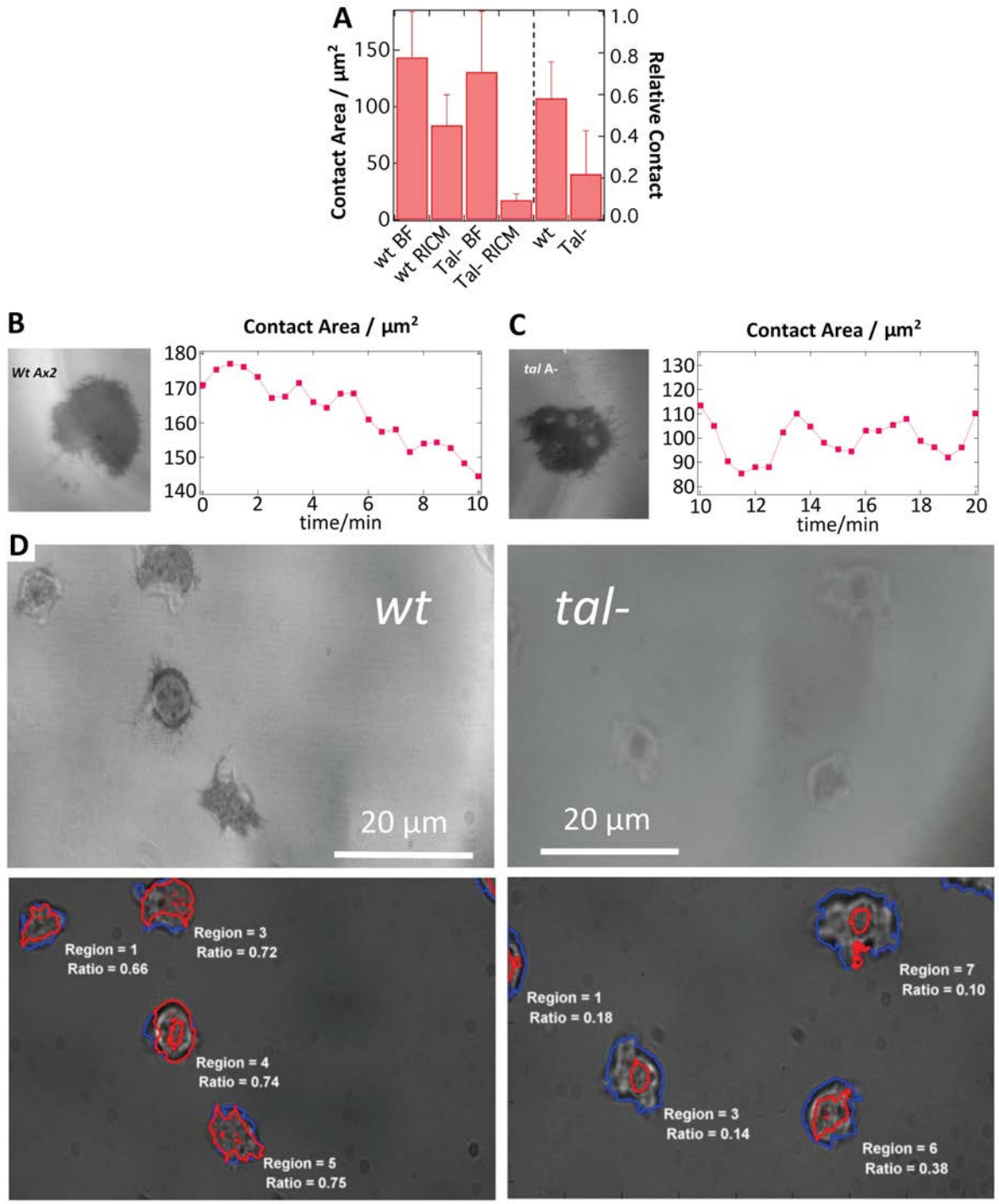

Figure 4.2 – (A) Averaged projected cell area and contact area obtained from bright field (BF) and reflection interference contrast microscopy (RICM) for WT and *tal*A$^-$ cells. (B,C) Time evolution of the contact area (RICM) for a WT and a *tal*A$^-$ cell. (D) Examples of BF and RICM images of WT and *tal*A$^-$ cells. Contact area (RICM, red lines) and contour area (BF, blue lines).

In Fig. 4.2 A, we show a comparision of the cell-substrate contact area,

viewed in reflection interference contrast microscopy (RICM), and the projected cell area, viewed in brigthfield microscopy, of AX2-WT and *tal*A$^-$ cells. In agreement with Ref. [49], we find that in the less adhesive *tal*A$^-$ cells, the substrate contact area is strongly reduced. Examples of the contact area and the projected cell area for both cell lines are shown in Fig. 4.2 D. The time evolution of the substrate contact area of a AX2-WT and a *tal*A$^-$ cell determined from RICM-images can be seen in Figs. 4.2 B and C. These time traces display a slow oscillatory trend, similar to the time evolution of the projected area in Figs. 4.1 A and B. We thus conclude that rapid fluctuations in the impedance amplitude are neither related to the projected cell area nor to the contact area as imaged by RICM. They rather arise from the formation of local adhesion sites leading to changes in the cell-substrate distance within the contact area.

4.1.3 Measurements of the projected cell area

The time course of the projected cell area for AX2-WT and *tal*A$^-$ cells were independently recorded from impedance measurements to test whether irregular impedance oscillations arise from those of the projected area. Images from time lapse microscopy were processed as described in the method section and 25 time series of length >1h were recorded for WT as well as *tal*A$^-$ cells, giving 50 short time series of 0.5 hours for both cell lines. Characteristic scales were found with the same wavelet based analysis as for impedance time series (Fig. 4.3), which is described in the methods section.

4.1.4 Standard deviations of detrended impedance time series correspond to the cell-substrate adhesion strengths

To systematically explore the relation between cell-substrate adhesion and fluctuations in the impedance signal, we have collected more than hundred single-cell impedance time series from AX2-WT cells and the four mutant strains *tal*A$^-$, *nap*A$^-$, *amp*A$^-$ and *GFP-α-tubulin* with different adhesion properties. We used microelectrode-arrays (MEAs) with 59 square electrodes ($50\mu m \times 50\mu m$) arranged on a square grid, with equal distances of $200\mu m$ between them (see Fig. 4.4 B). If vegetative cells at low density were seeded into the culture chamber, some electrodes were found with just a single cell on top. In each experiment, four such electrodes were selected and simultaneously recorded. In this way, at least 20 single-cell

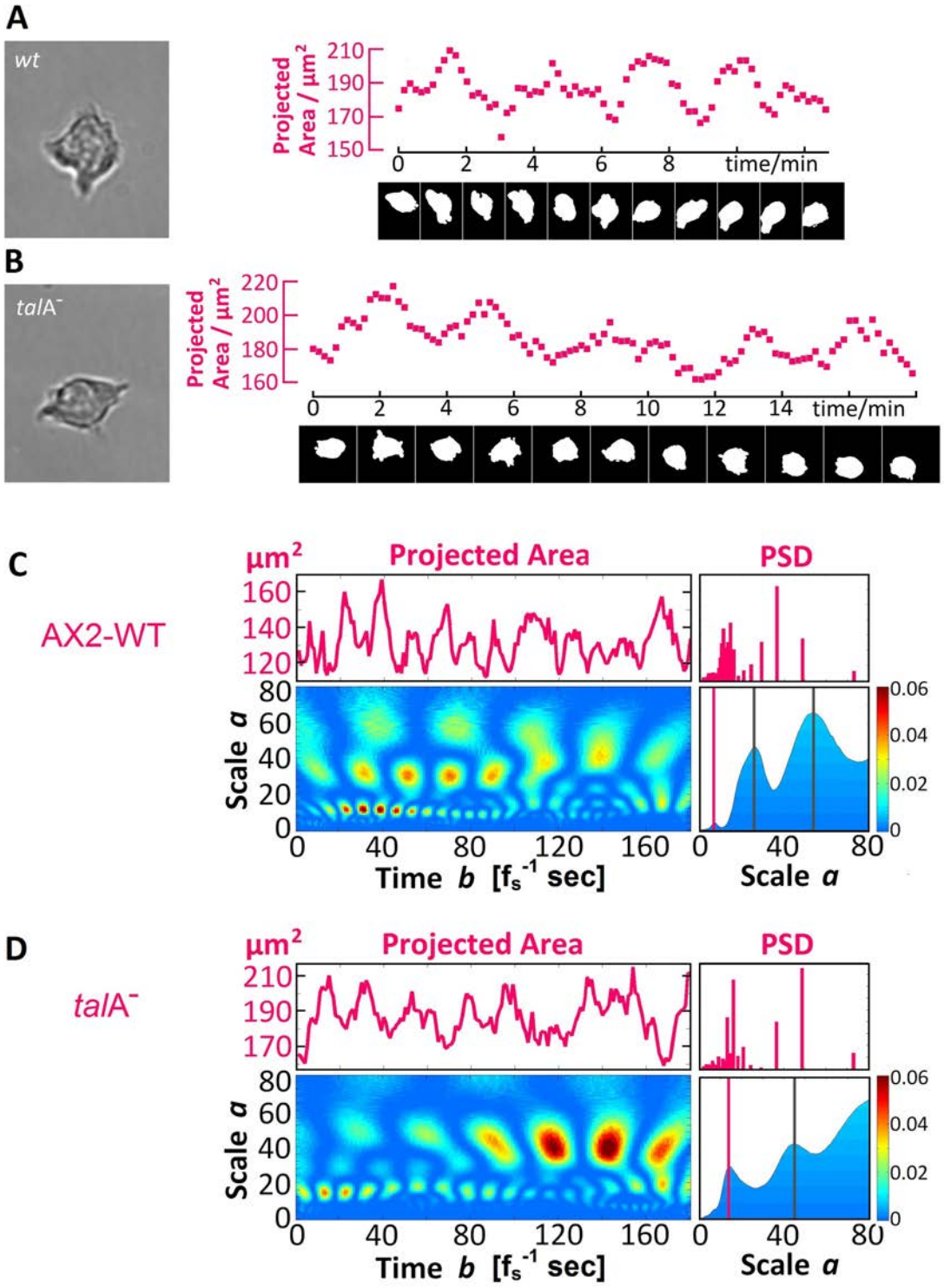

Figure 4.3 – (A,B) Time evolution of the projected area for a selected AX2 cell and a *tal*A$^-$ cell, shown together with the cell shapes at minima and maxima of 5 oscillation periods. (C,D) Selected time series of the projected area, wavelet scalogram, time-averaged scalogram and power spectrum for an AX2 cell and a *tal*A$^-$ cell.

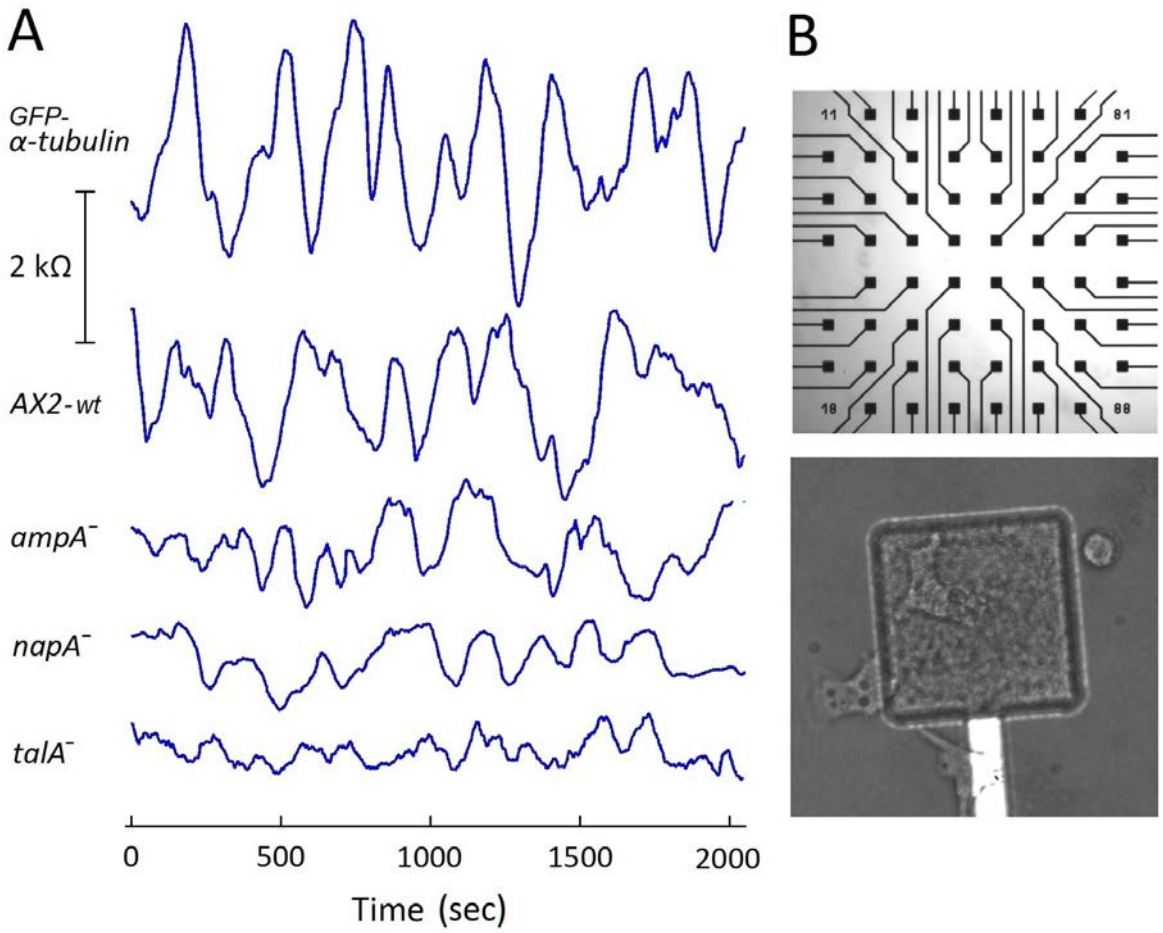

Figure 4.4 – (A) Selected single cell impedance time series for AX2-WT and mutant cell lines. (B) Photographs show 1. 59 square electrodes (50μm×50μm) of a micro-electrodearray (MEA) used for single cell recordings and 2. A single electrode with cells.

impedance time series of approximately 30 min were recorded for every cell line (20 timeseries for WT, *nap*A$^-$, and *amp*A$^-$, 26 for *tal*A$^-$, and 32 for *GFP-α-tubulin*).

In Fig. 4.4A, five selected examples of our single cell measurements are displayed. The impedance signals show typical irregular oscillations arising from correlated shape changes of single cells attached to the electrode. We applied the wavelet transform to the impedance time series to find the characteristic scale representing the motility cycle period as described in the method section. The interesting range, where characteristic scales occurred was 1 – 800 (the relation between scale a of the Morlet wavelet and the period p is given by $p = ca$ with $c \approx 1.23$). In our data, three scales in the relevant range were identified in the scalograms for the predominant part of all time series. The scales change over time due to non-stationarities and alterations of the motility cycle period of a cell. To identify the dominant

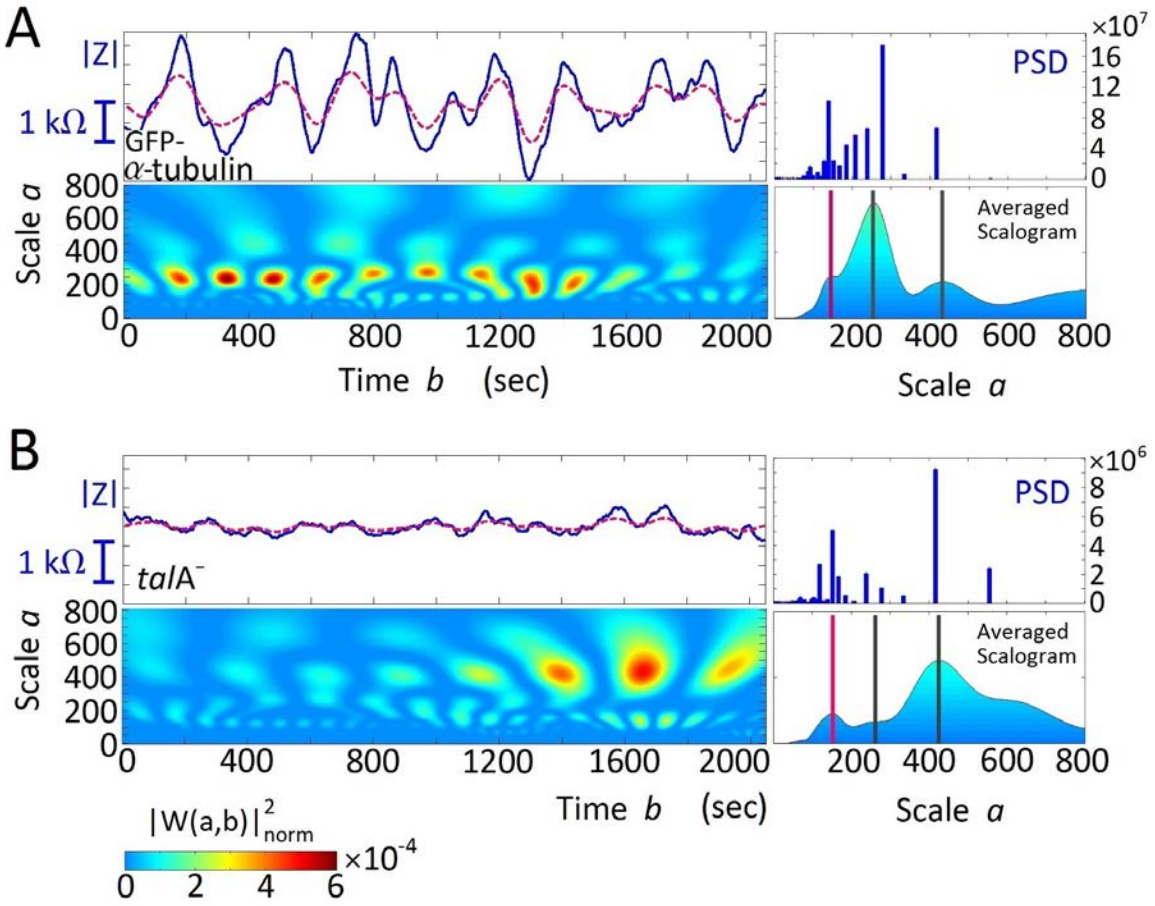

Figure 4.5 – (A) Single cell impedance time series and wavelet scalograms for *GFP-α-tubulin* and *tal*A$^-$. Low-pass filtered signals (dashed lines). On the right side time-averaged scalograms and power spectra (PSD) are shown.

scales of a time series, the wavelet coefficients $|X_W(a,b)|^2$ were time-averaged. The averaged wavelet transforms are shown to the right of each scalogram in Fig. 4.5. The characteristic scales correspond to the local maxima in the averaged scalograms. For different time series, the maxima may occur at different positions and with different weights.

The smallest persistent scale in an averaged scalogram represents the smallest characteristic oscillation period of the signal. We used this scale (resp. the corresponding period) as the characteristic motility cycle period of a given cell. This scale was marked by a red vertical line in the averaged scalograms of Fig. 4.5. The averaged motility cycle periods are shown in Fig. 4.6 B. Above the averaged scalograms of Fig. 4.5, the corresponding power spectra are shown. Obviously, in most cases, the same three-scale-structures as in the scalograms appear. But only from the scalograms it can be easily reconstructed how scales evolve over time.

After removing linear trends, the standard deviations of fluctuations of

impedance signals were computed to quantify their amplitudes.

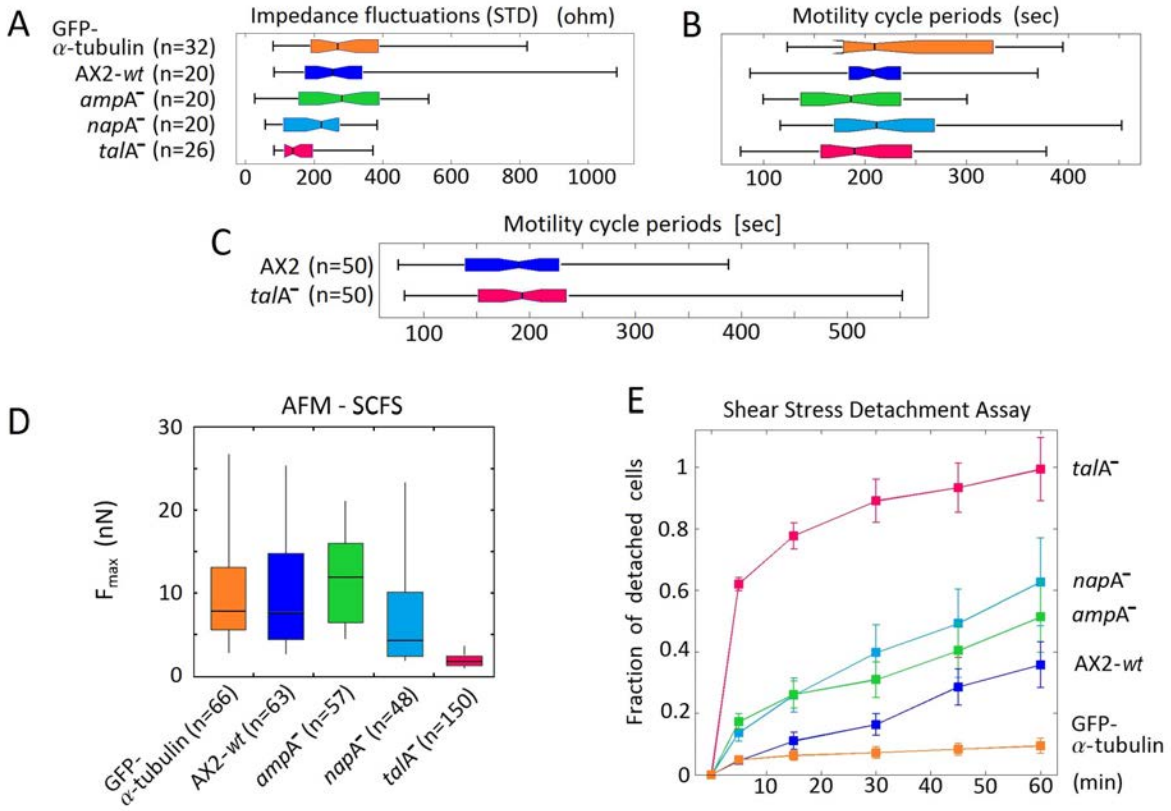

Figure 4.6 – (A) Standard deviations of high-pass filtered impedance signals. (B) Motility cycle periods (from impedance time series). (C) Motility cycle periods (from projected area time series). (D) Maximal adhesion force measured with AFM-SCFS. (E) Shear stress detachment assay. At indicated time points detached cells were counted.

Results are presented as boxplots in Fig. 4.6 A. We observed a correlation between the standard deviations of the detrended impedance time series and the adhesion strengths measured independently by the fraction of detached cells in the shear stress detachment assay resp. cantilever picking of single cells by AFM-SCFS (see method section for a detailed description of independent adhesion measurements). The largest standard deviations are found for the strongly adhesive cell lines *GFP-α-tubulin*, AX2-WT and *amp*A$^-$ (impedance analysis and cantilever picking reveal *amp*A$^-$ as the most strongly adhesive cell line, while in the shear stress detachment analysis *GFP-α-tubulin* is the strongest). All methods clearly reveal *tal*A$^-$ and *nap*A$^-$ as the cells with the weakest adhesion strength.

No such trend is found for the motility cycle periods derived from impedance data (Fig. 4.6B). Cycle periods of *tal*A$^-$ cells do not deviate significantly from those of other cells. Similarly, the motility cycle periods derived from projected cell area data for AX2-WT and *tal*A$^-$ cells (see

Fig. 4.6 C) do not significantly differ from those calculated from impedance data. To compare scales of the projected area with those of the impedance, note that the sample frequencies were different for both data sets ($f_s \approx 1$ sec^{-1} for impedance data and $f_s \approx 0.1$ sec^{-1} for projected area data), i.e. the scales of the projected area must be multiplied with the corresponding sample period of approximately 10 sec to make them comparable to the scales of the impedance.

4.2 Cell population measurements

4.2.1 Cell-substrate impedance kinetics during the onset of collective behavior of aggregation-competent *Dictyostelium* cells

Dictyostelium amoebae have developed a survival strategy upon depletion of nutrients, which marks the onset of collective behavior, cell communication and multicellularity of eukaryotes [19]. This developmental program mediated by gene expression is easily recalled in the laboratory by separating cells from the culture medium and the nutrients therein. During a period of about 6 hours starved cells then acquire a chemotactic machinery which enables them to sense sources of cyclic adenosine 3',5'-monophosphate (cAMP) and to move collectively in streams towards centers of aggregation. At the end of this process the cell aggregate develops to a fruiting body at the end of a long stalk to facilitate spore dispersal.

ECIS was successfully employed to monitor micromotion of aggregating amoebae during their developmental life cycle by recording time series of the impedance magnitude at 4 kHz AC frequency [20, 21, 65]. Planar microelectrodes placed at the bottom of culture wells work as sensors in the aggregation plane of amoebae. Cells are filled via a pipette in culture wells, spread and attach to the bottom of wells and start to move across electrodes. Only the small fraction of the whole cell population located on top of the electrode is traced by impedance sensing, but the whole process of aggregation can be reconstructed from this time trace due to the onset of collective behavior, to which more and more cells become entrained over large distances by chemotaxis.

It is observed that, at the start of measurements, when cells are filled in the culture wells, the initial sharp increase in impedance is proportional to the density of cells (Fig. 4.7 A). The peak is due to an initial uniform distribution of cells across the whole fluid volume in the culture well, since the measurement is very sensitive to changes of the volume composition

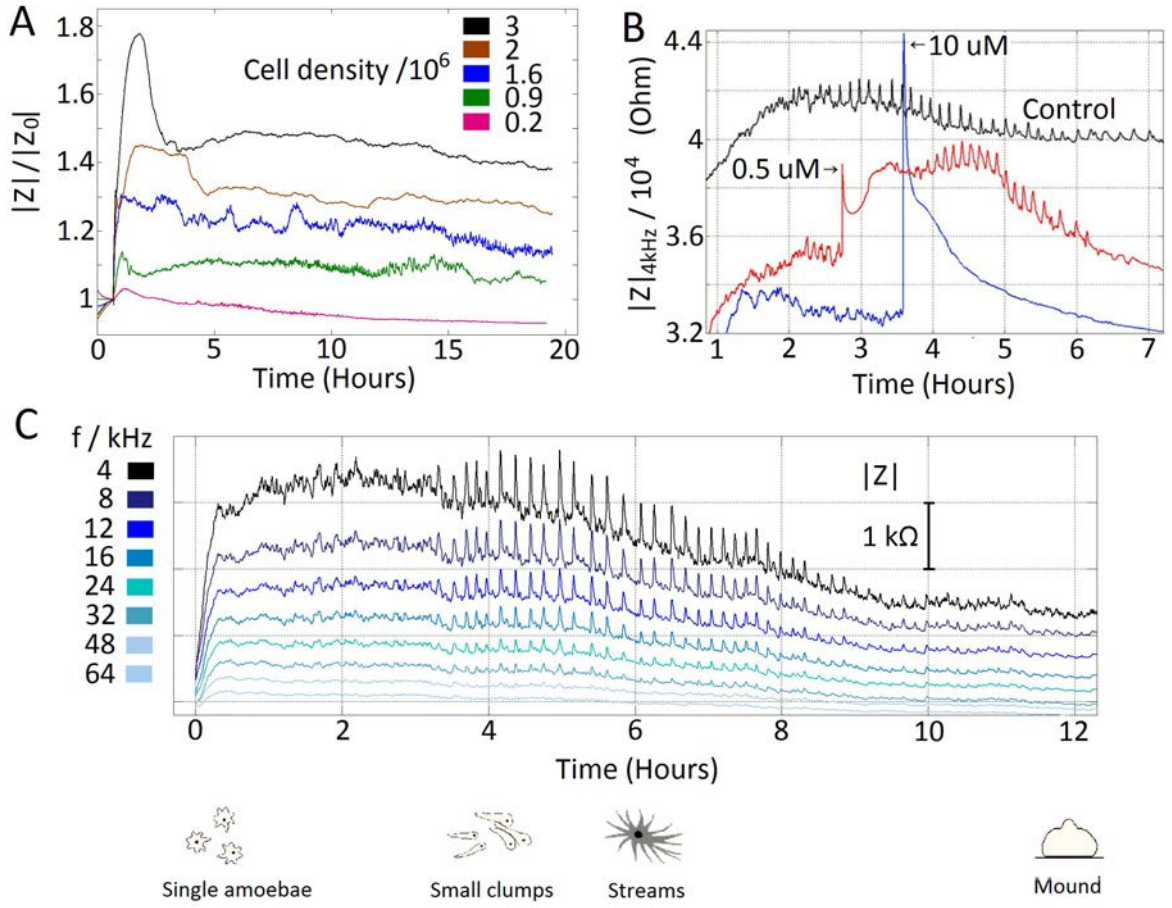

Figure 4.7 – (A) Impedance magnitude divided by the magnitude of a cell-free electrode at 4 kHz for different cell densities. (B) Impedance kinetics of cells treated with Latrunculin A. (C) Impedance kinetics for AC frequencies ranging from 4 to 64 kHz.

and its biomass content. Then it takes about half an hour for cells to sediment by gravity to the bottom of the culture well, causing a drop of impedance from the initial peak. After this drop the impedance begins to fluctuate with the onset of cell micromotion. For a given geometry and size of the electrode system and a given AC frequency, the strength of impedance fluctuations, quantified by the standard deviation of the time signal, also depends on cell density. As demonstrated in the last chapter for an impedance spectrum and also for the time evolution shown in Fig. 4.7 C, an AC signal frequency of 4 kHz produced the largest fluctuations and oscillations of the impedance magnitude for cell densities ranging from 5×10^5 to 1.5×10^6cells/cm^2 (corresponding to 250-750 cells on an electrode with a diameter of 250 μm). This is the expected behavior, when one considers that cell motion is the cause of impedance fluctuations. Too few cells on an electrode will diminish such variations, whereas a too large density will produce higher impedances, but will also level out individual

cell contributions to the overall deviations from mean.

That cell micromotion is the cause for fluctuations visible in impedance time series can be demonstrated when micromotion abruptly halts during the measurement. This can be achieved by application of Latrunculin A, a toxin produced by certain sponges that prevents actin polymerization and thus the remodeling of the cytoskeleton during cell movement by binding actin monomers near the nucleotide binding cleft [91]. Fig. 4.7 B shows impedance kinetics of AX2 WT cells, where a weak and a strong concentration (0.5μM and 10μM) of Latrunculin A was added to the culture wells with a pipette. This caused a strong peak and afterwards a decrease of the impedance signal in the absence of fluctuations due to a rounding up of cells, which were no longer able to move. For the weak concentration cells recovered after about half an hour, which caused a new increase in impedance and the recovery of fluctuations after about one hour. Cells treated with a strong concentration did not recover and the smooth impedance signal decreased further until the end of the measurement.

Fig. 4.8 A shows an example of an impedance measurement of *Dictyostelium* cells during their developmental life cycle, starting with the onset of starvation and ending with the collection of cells in aggregates, which leads to the formation of mounds. Fig. 4.8 B showas further examples of impedance oscillations. The process of collection is thought to be mediated by the upcoming of signaling centers during the first hours of starvation, which periodically emit pulses of cAMP that extend as spatiotemporal waves through the surrounding population. Cells sense the change in concentration and the location of the emitting center when the wave front passes and response by emitting an own pulse of cAMP—thereby reinforcing the wave—and by making a step forward in direction to the wave source. The consequence is entrainment of many cells from a large area; important are the changes in morphology strictly coupled to the chemotactic response, since only these morphological changes are traced by impedance recordings. Evidence is based on darkfield microscopy studies of aggregating cell populations, showing wave patterns as alternating dark and bright bands, corresponding to resting round-shaped cells and moving elongated cells, which scatter light in a different manner. *Dictyostelium discoideum* and some other cell lines exhibit cyclic periodicities in morphological changes, governed by protrusions, retractions and adhesions [21, and references therein].

The emergence of collective behavior during the aggregation process is reflected in three stages visible in impedance kinetics (indicated durations of these stages may vary among different cell populations):

1. (0-3 h) Amoebae located on the electrode surface independently follow

their intrinsic motility cycles similar than vegetative cells, which perform cyclic shape oscillations and adhesion dynamics without phase entrainment on the population level. This causes the impedance to fluctuate randomly, i.e. periodicities occur more or less, but are not maintained over a larger period. Individual 'out-of-phase' micromotions produce desynchronized micro-impedance signals, which cause erratic fluctuations of the overall mean impedance output.

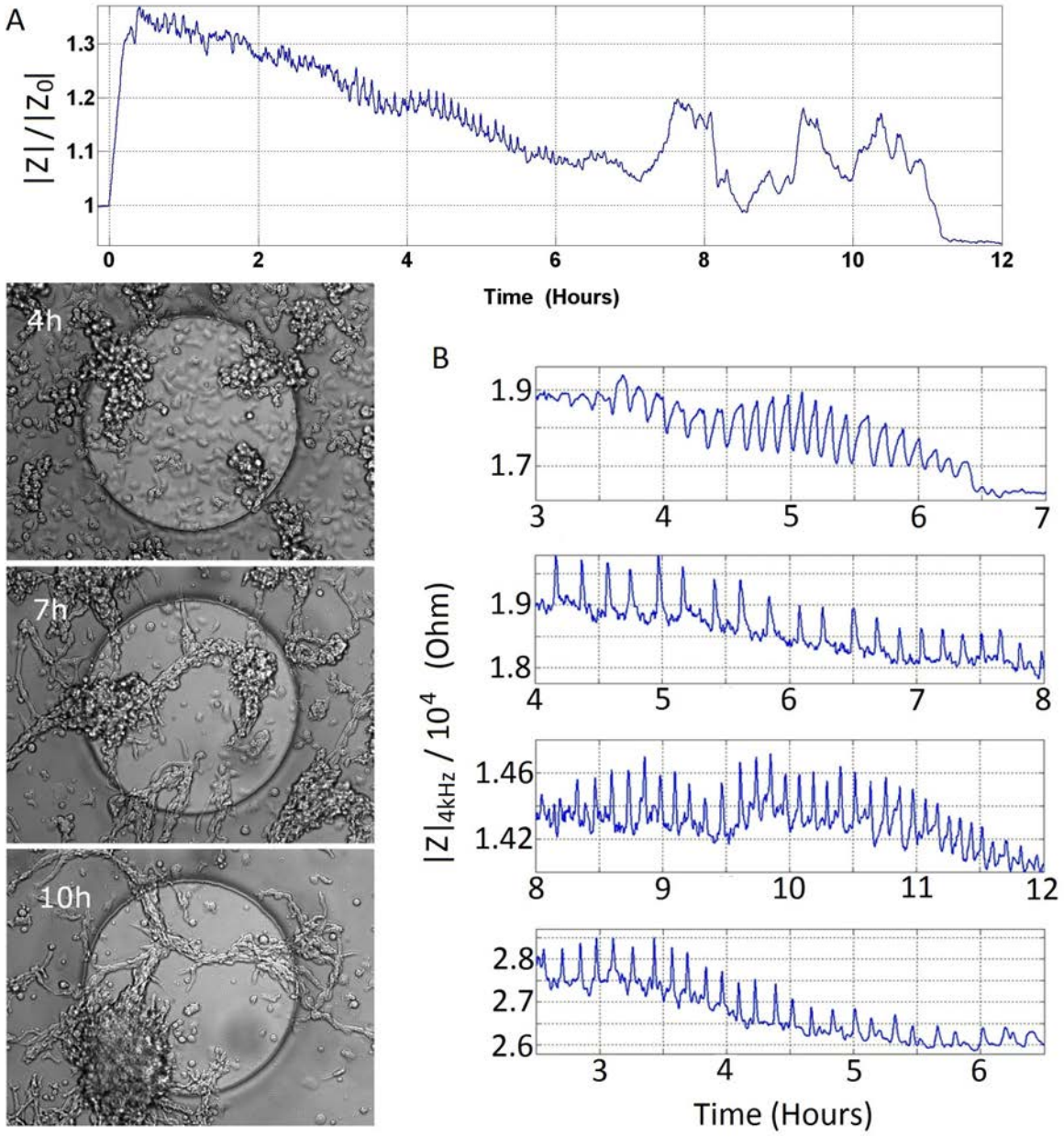

Figure 4.8 – (A) Impedance kinetics of starved *Dictyostelium* cells during the pre-aggregation phase. Photographs depict the cell-covered electrode at indicated times. (B) Further examples of impedance oscillations.

2. (3-6 h) The dynamics suddenly changes when distinct periodic peaks or

spikes arise in the impedance kinetics, which at first appears as a surprising event due to the fact that photographs taken at this stage still show single cells performing motility cycles as before. But what really happened is a phase transition to collectively performed shape oscillations and cell-substrate contacts, leading to coherent oscillations of the overall impedance, since the few cells located on the electrode surface are stimulated from a passing cAMP wave *at the same time*. After the receipt of a signal cells elongate and make a step forward. Periodic impedance peaks resemble such of coupled excitable oscillators, displaying rapid phase entrainment upon suprathreshold stimuli. Evidence that cell-substrate interactions (adhesions, changes of the substrate distance) are the main cause for the occurence of impedance spike trains comes from the analysis of motility cycles of single cells, showing that adhesion dynamics consists of cyclic exertion of traction forces to the substrate, associated with displacement of the cell body by protrusion and retraction [59, 92]. Adhesion dynamics on the nanometer scale therefore affect the current flow through the cleft between basal membrane and substratum. At the end of this stage cells have collected to small clumps and clusters, which in some measurements produce small monomodal impedance oscillations different from the shape of spikes seen before [21].

3. (>6 h) Small cell clumps further collect by streaming in large clusters, which later merge in still larger clusters to form a mound. If such clusters are located at the electrode surface, then the impedance kinetics shows large amplitude fluctuations in the absence of spiking. When moving clusters leave the electrode, or when their location is not identical to that of the electrode, than the impedance decreases and fluctuations decease, sometimes leaving few roundish cells behind that do not oscillate [21].

4.2.2 Impedance spike trains arise from the collective performance of cell-shape oscillations and cell-substrate adhesions

With the above given observations of the time evolution of the impedance during the first hours after starvation of a population of amoebae, we were interested in modelling the phase transition to collective behavior and its reflection in the emergence of coherent impedance oscillations (spike trains). As the starting point, we define specific single-cell microscopic impedances Z_{nm} (n,m=1,...,N) on a N×N square grid. Every single cell impedance is calculated by the Giaever-Keese impedance formula (see formula 2.3 in section 2.3). Then, the specific ensemble impedance of an electrode

covered by N^2 cells is represented by a 2D-parallel configuration of N^2 micro-impedances:

$$Z = \left[\sum_{n,m=1}^{N} \frac{1}{Z_{nm}} \right]^{-1} \tag{4.4}$$

With this definition we are able to compute microscopic single cell impedances Z_{nm}—depending on single cell shape oscillations (variations of $r_{c,nm}$) and substrate dynamics (variations of h_{nm})—and their combined effect to the overall ensemble impedance Z. It is clear that changes of Z are most pronounced, when individual contributions Z_{nm} act in synchrony. The driving force of entrainment of single cells is the cAMP signaling system. To model the process of synchronization, we have combined the single-cell micro-impedances Z_{nm} with the kinetic equations of Martiel and Goldbeter, governing the cAMP signaling system of a single cell, as described in the following:

The cAMP signalling system represents the central part of the complex chemotactic machinery of single *Dictyostelium* cells built up during the developmental live cycle. Given this system for single cells, it enables a cell population to collect widespread single cells to aggregation centers without the need of guidance by specialized cells, since different modes of dynamic behavior can be recalled from the same cell in response to surrounding stimuli: autonomous oscillations of cAMP, relay of cAMP pulses and adaption to constant stimuli ([19, chapter 8 and references therein]). Martiel and Goldbeter proposed kinetic equations for the signaling system based on receptor desensitization upon stimulation by cAMP [93]. In this model, extracellular cAMP binds to a membrane-bound receptor in active state and thereby activates the enzyme adenylate cyclase (ACA) located on the intracellular side of the membrane. ACA activation in turn stimulates internal cAMP production and secretion, which increases the external cAMP level and amplifies the cyclic process. Amoebae control the runaway dynamics by secretion of a cAMP phosphodiesterase (PDE), which degrades cAMP. Degradation is also controlled by secretion of an inhibitor of PDE (PDI). Concentrations of both proteins are known to increase during the aggregation phase [19, p.117,121-125]. The dynamics as a whole has all properties of an excitable system, which is well known to generate spatiotemporal excitation waves and spirals throughout a population of coupled excitable elements. Selforganization in this sense must be optimized by fine tuning of the excitable dynamics by secretion of PDE and PDI to the extracellular space.

We have used a two-variable version of the Martial-Goldbeter model, governed by the activator variable γ_{nm}, the external cAMP concentration

of a single oscillator divided by the dissociation constant K_R=10^{-7}M, and the inhibitor variable ϱ_{nm}, the fraction of receptors in active state. This model can be found in [94]. We used it without a spatial term (Laplacian). The set of kinetic equations is given by

$$\epsilon\dot{\gamma}_{nm} = s\Phi_{nm} - \gamma_{nm} + C\bar{\gamma} + \sqrt{2D}\xi(t) \tag{4.5}$$

$$\dot{\varrho}_{nm} = -f_{1,nm}\varrho_{nm} + f_{2,nm}(1 - \varrho_{nm}) \tag{4.6}$$

with the functions

$$\Phi_{nm} = \frac{\lambda_1 + Y^2}{\lambda_2 + Y^2}, \quad Y = \frac{\varrho_{nm}\gamma_{nm}}{1 + \gamma_{nm}}$$

$$f_{1,nm} = \frac{1 + \kappa\gamma_{nm}}{1 + \gamma_{nm}}, \quad f_{2,nm} = \frac{L_1 + \kappa L_2 c\gamma_{nm}}{1 + c\gamma_{nm}}$$

The last two terms in equation 4.5 represent the coupling term with coupling strength C and the noise term with noise strength D and Gaussian white noise $\xi(t)$. Parameter values used in the simulations are given in the Appendix.

Initially, a single unperturbed oscillator stays in a stable state. Binding of cAMP to a receptor in active state occurs when a stimulus exceeds a threshold. Then, ACA is activated by the bound receptor (represented by the function Φ), intra- and extracellular cAMP levels rise and receptors enter the desensitized or passive state, which in turn decreases ACA activation and cAMP levels. A new excitation can only occur when the active state of receptors is reestablished after a refractory period. Fig. 4.10 A shows the time evolution of the variables of a single oscillator, driven by white noise above the threshold (D=2×10^{-6}). Fig. 4.10 B depicts the nullclines of the system and single oscillator excitation loops in phase space. A system of noise-driven globally coupled oscillators, which are coupled by the mean cAMP output

$$\bar{\gamma} = \frac{1}{N^2}\sum_{n,m=1}^{N}\gamma_{nm}, \tag{4.7}$$

will also exhibit a transition to sustained oscillations of the mean output of the system, if the noise strength D exceeds a threshold. The most regular oscillations occur at intermediate noise levels, a phenomenon known as *coherence resonance*. Pattern formation occurs if a local coupling to the next neighbors is introduced, that is

$$\bar{\gamma} = \gamma_{n-1,m} + \gamma_{n+1,m} + \gamma_{n,m-1} + \gamma_{n,m+1} - 4\gamma_{n,m}. \tag{4.8}$$

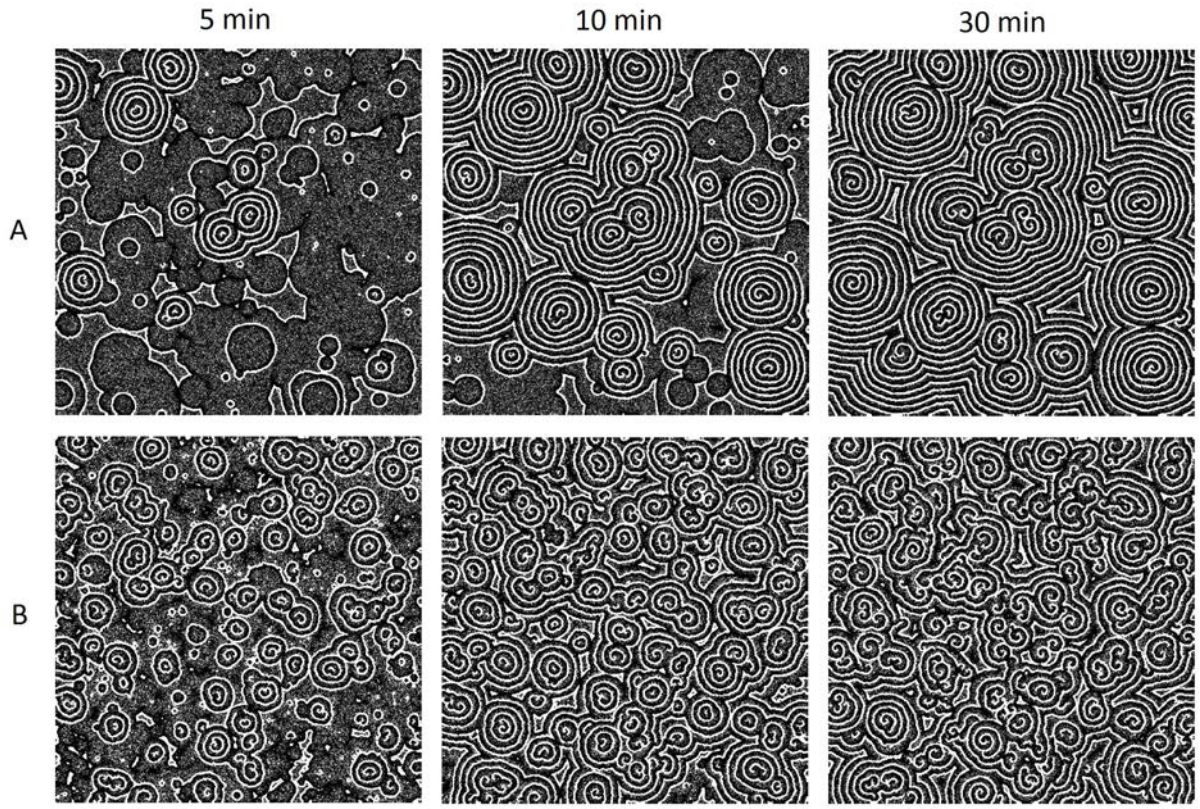

Figure 4.9 – Spiral competition in an ensemble of 400×400 coupled cAMP oscillators for different noise strengths. (A) D=8×10^{-8}, (B) D=1.3×10^{-7}.

Then, at low noise levels, spirals and targets can propagate through a population, thereby entraining a large number of cells. In this context it was found that mutants lacking the phosphodiesterase inhibitor PDI were not able to form aggregates by entraining cells from large territories. The selection for spiral waves by tuning of excitability may therefore be an important function of this protein [95]. Fig. 4.9 shows spiral competition for two different noise strengths in a population of 400×400 oscillators. For a given territory size (the grid size in this simulation is arbitrary), increasing noise levels produce an increasing number of signaling centers.

To couple the above introduced micro-impedances Z_{nm} to the cAMP signaling system, the set of equations for γ_{nm} and ϱ_{nm} are extended by equations for the radius $r_{c,nm}$ and the substrate separation h_{nm} of a single cell. These variables are then coupled to the signaling system by computing them as simple linear functions of the receptor variable ϱ_{nm}, $r_{c,nm} = A\varrho_{nm} + B$ and $h_{nm} = E\varrho_{nm} + F$, or, alternatively, to the adenylate cyclase function Φ_{nm}. Micro-impedances are then computed as functions of these variables, $Z_{nm} = z(r_{c,nm},h_{nm})$, were z is given by the Giaever-Keese impedance model. We denote that a detailed derivation of kinetic equations according to the recruitment/activation of certain proteins, governing the changes in

morphology after the receipt of a chemotactic stimulus, such as cringing, actin polymerization or actomyosin contraction, is beyond the scope of our model. Instead, we propose above given simple relations, where radius and substrate distance depend on the receptor variable or ACA-function, which enables us to demonstrate the emergence of impedance spike trains in response to shape oscillations (governed by $r_{c,nm}$) and substrate interactions (governed by h_{nm}). Fig. 4.10 C shows a single oscillator impedance peak of Z_{nm} according to variations of $r_{c,nm}$ and h_{nm}. The gringe response, i.e. rounding up of the cell shape, is the first event after receptor occupation by cAMP (increase of γ_{nm}) and is initiated by a decrease of $r_{c,nm}$. When this response is completed, the cell re-elongates (increase of $r_{c,nm}$) and starts to establish adhesive contacts (decrease of h_{nm}). The time dependence of h_{nm} is therefore delayed: $h_{nm}(t) = E\varrho_{nm}(t\text{-}\tau) + F$, where τ is the duration of the gringe response. It is seen from Fig. 4.10 C that a strong increase of the impedance Z_{nm} occurs by a simultaneous increase of $r_{c,nm}$ and decrease of h_{nm}. The impedance has a maximum when $h_{c,nm}$ reaches its minimum. Variations of the substrate distance therefore have the strongest effect on impedance kinetics.

Phase entrainment and sustained oscillations in an ensemble of oscillators occur by periodic stimulation above the threshold. This can be achieved in different ways. When globally coupled, the phases are entrained by their own global phase (mean cAMP output), which becomes the periodic driving force of entrainment. But, this would not lead to the observed decrease of oscillation periods and amplitudes and final decease of oscillations 2-6 hours after their onset, which is due to a progressive increase of cAMP concentration towards the end of the pre-aggregation phase. This increase in cAMP levels can be simulated by increasing the noise strength over time in a system of globally coupled oscillators (Fig. 4.10 F), or, alternatively, by coupling the oscillators to their own accumulated amount of cAMP. In the latter case, the mean-global-output term is replaced by an accumulation term,

$$\bar{\gamma}(t) = \sum_{k=1}^{i} \frac{1}{N^2} \sum_{n,m=1}^{N} \gamma_{nm}(k\Delta t), \tag{4.9}$$

where i is the number of timesteps in the simulation up to time $t=i\Delta t$. Upon subtreshold stimulation at a low constant noise level, the accumulation term slowly increases until the oscillators enter the regime of coherent oscillations. Then, with every collective excitation, the accumulation term strongly increases in a stepwise manner, leading to adaption by receptor occupation and a rapid decay of excitations when the coupling strength C is strong. Thus, to delay receptor occupation and control the process of

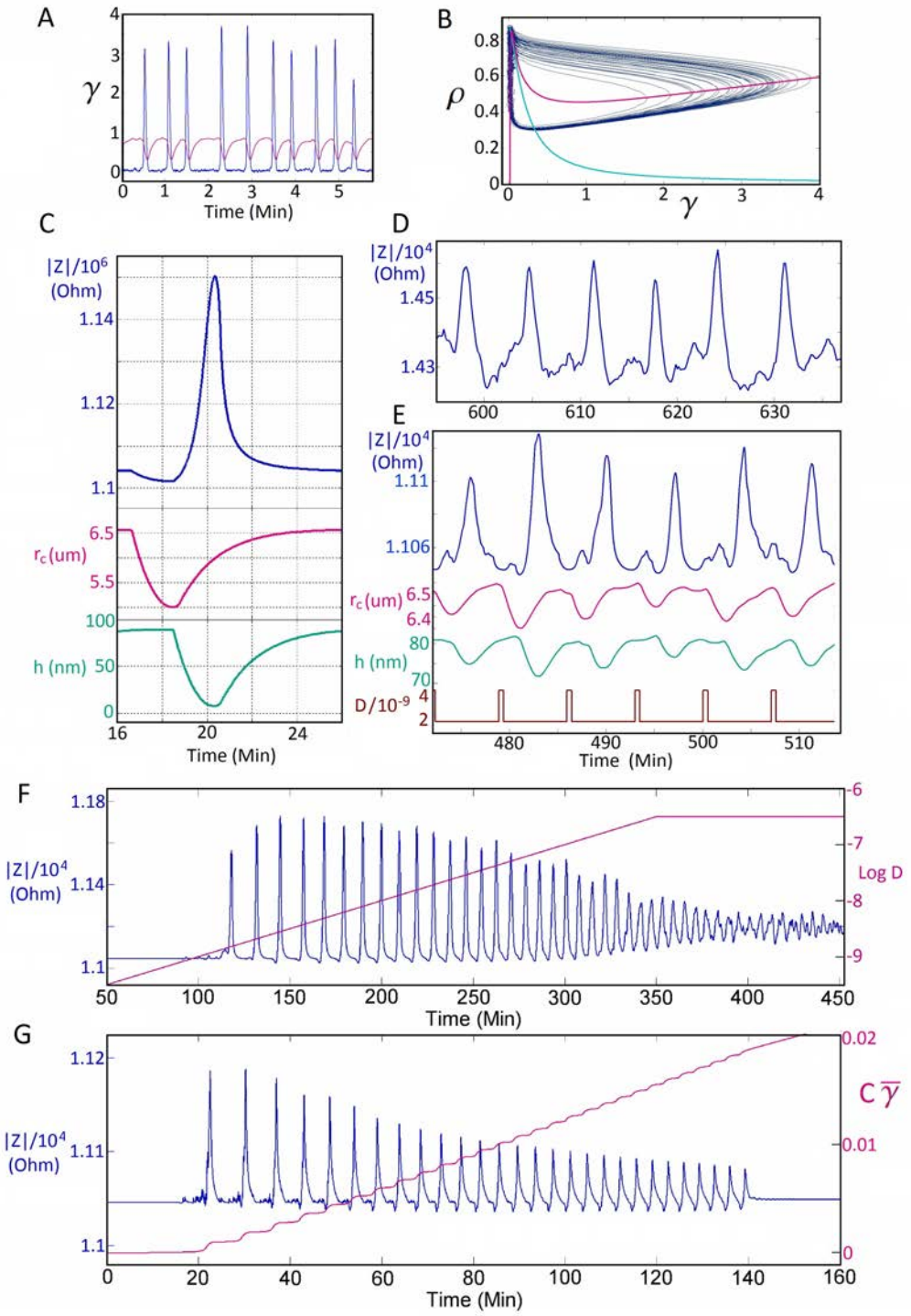

Figure 4.10 – (A) Single cAMP oscillator; cAMP concentration divided by the dissociation constant K_R=10^{-7}M (blue) and number of receptors in active state (red). Noise strength D=2×10^{-6}. (B) Nullclines $\dot{\gamma}_{nm}$=0 (red), $\dot{\varrho}_{nm}$=0 (green) and variables in phase space. (C) Micro-impedance of a single cell, governed by r_c and h, which are coupled to the receptor variable. Constant stimulus α=0.0005 instead of noise. (D) Experimental impedance time trace (AX2-WT cells on a 250μm-electrode). (E) Model impedance of 100 oscillators without coupling (C=0), but periodic noise modulation. (F) Model impedance of 100 globally coupled oscillators; noise strength increases. (F) Model impedance of 100 oscillators; constant noise level; The coupling term is replaced by an accumulation term.

aggregation, the cells have to degrade most of accumulated cAMP, which is simulated by decreasing the coupling strength C. Fig. 4.10 G shows a simulation with C=6.5×10^{-7}, where the spike train deceases after a longer period of about 2 hours, as observed in measurements.

In another situation, the driving force of entrainment is given by a periodic modulation of noise levels, where no coupling is needed for synchronization of oscillators (C=0). This situation may be given when aggregating cells repeatedly and simultaneously become stimulated by a passing wave of cAMP. This is shown in Fig.(Fig. 4.10 E), where a periodic alternation of two different noise levels leads to oscillations of the ensemble impedance Z. Oscillators were stimulated for 30 seconds with stronger noise, leading to distinct peaks of Z, and afterwards with weaker noise for 6.5 minutes, leading to suppressed phases, since not all oscillators were excited during this interspike interval. Periodic modulation of noise was adjusted to match the frequency of impedance peaks and the occurrence of suppressed phases during interspike intervals seen in the measurement of Fig. 4.10 D.

We note, that our model depends solely on the well-established concepts of excitability and refers only to the time evolution of the system, without the inclusion of spatial and cell density information. Also, cell movement and how it affects the impedance kinetics is not considered. Motility cycles are present in vegetative cells as well as during development, and their performance by many cells without entrainment of phases and frequencies still cause irregular fluctuations of the impedance, as seen in almost every measurement before the transition to coherent oscillations. During this transition cells become entrained in collective behavior, meaning that individual 'out-of-phase' motions disappear. However, our model impedance is coupled only to those morphological changes, which arise during the onset of collective behavior, i.e. it shows a constant baseline before the transition to coherence, which is not observed in measurements. Despite these limitations we are able to demonstrate the transition to coherent oscillations and the evolution and decay of impedance spike trains, as observed in experiments.

4.3 Chemotactic cell migration

Cell migration is a fundamental survival strategy in nature and a prerequisite for the development of all higher multicellular organisms. Cultured cells and the availability of mutant cell lines provide the basis for systematic studies of the components and details of migration. In this chapter, we focus on chemotactic cell migration and the development of micro-laboratory devices for the electrical detection of chemotaxis. There are a variety of methods

which are traditionally employed to assess chemotactic movement, such as under-agarose assays, boyden chambers, scratch or exclusion zone assays, which partly use time lapse microscopy for real-time monitoring of migration speeds (for a review see [96]). The central task which has to be accomplished by chemotaxis assays is the preparation of stable chemical gradients as the external cue for chemotactic movement. The use of microelectrodes to measure time-resolved chemotaxis of weakly substrate-adherent motile cells led to the develeopment of ECIS-techniques. In [97] an ECIS/taxis system was designed, which combines a conventional ECIS 8-well-array with an under-agarose assay for real-time measurements of chemotactic cell motility. Our aim was to extend the concept of impedance sensing to the field of microfluidics with special focus on the miniaturization of the measurement cell. The incorporation of cell-substrate impedance sensors into microfluidic channel systems by using planar microelectrode arrays as substrate for micro channels, which are embossed to the surface of a piece of PDMS, is not a new concept. But we show for the first time impedance measurements in combination with a microfluidic concentration gradient generator to provide a stable gradient. The results are presented in sections 4.3.1 and 4.3.2. In most ECIS measurements a single electrode is used. We use arrays with four working electrodes to facilitate the measurement of chemotaxis speed by utilizing the spatial disposal of electrode stripes in a zebra-crossing configuration. Furthermore, we advanced in the development of a miniaturized system in two steps: 1. We employed the relatively new technique of photolysis of caged compounds to create a cAMP micro-source in a narrow space, and 2. we decoupled the large counter electrode from the substrate of the micro channels (electrode array) and reintroduced it in the system as the ceiling of the micro channels. Measurements with photo uncaging, using the conventional electrode arrays as well as the compact electrode arrangement, are presented in section 4.3.3.

4.3.1 Cell migration in a flow chamber traced by cell-substrate impedance sensors

To develop an impedance-based cell migration assay we incorporated planar gold-film microelectrodes into a microfluidic device. Planar microelectrode arrays with four working electrodes (WE) and a large counter electrode (CE) were fabricated using lift-off techniques and sputter coating as described in section 3.6. According to the protocol given in section 3.7 the miceo channel structure of a concentration gradient generator shown in Fig. 3.5 (section 3.8) was embossed via soft lithography onto the surface of PDMS. Cutted pieces of PDMS were positioned on top of electrode arrays with the

alignement tool (Fig. 3.6) described in section 3.9 and the completed chip was sealed and connected to the transimpedance amplifiers with the clamp tool described in section 3.10. Fig. 3.7 shows a scetch and a photograph of the whole device. Four holes in the upper plastic plate serve as tube connectors, two of which supply the inlets of the gradient generator with cAMP and buffer only via a syringe pump (not shown), the others serve as cell inlet and common outlet. The active part of the chip was imaged via an inverted microscope through a large hole in the lower plastic plate. Fig. 4.11 shows a scetch of the details. A variety of electrode geometries were tested, a configuration with electrode stripes (width and spacing were both 50μm) is shown in top view in the upper panels of Fig. 4.11 (depicting the whole chip and a detailed look on the active part). Photographs in the lower panels show the active part after cells were filled in the flow channel and a front view of the whole chip.

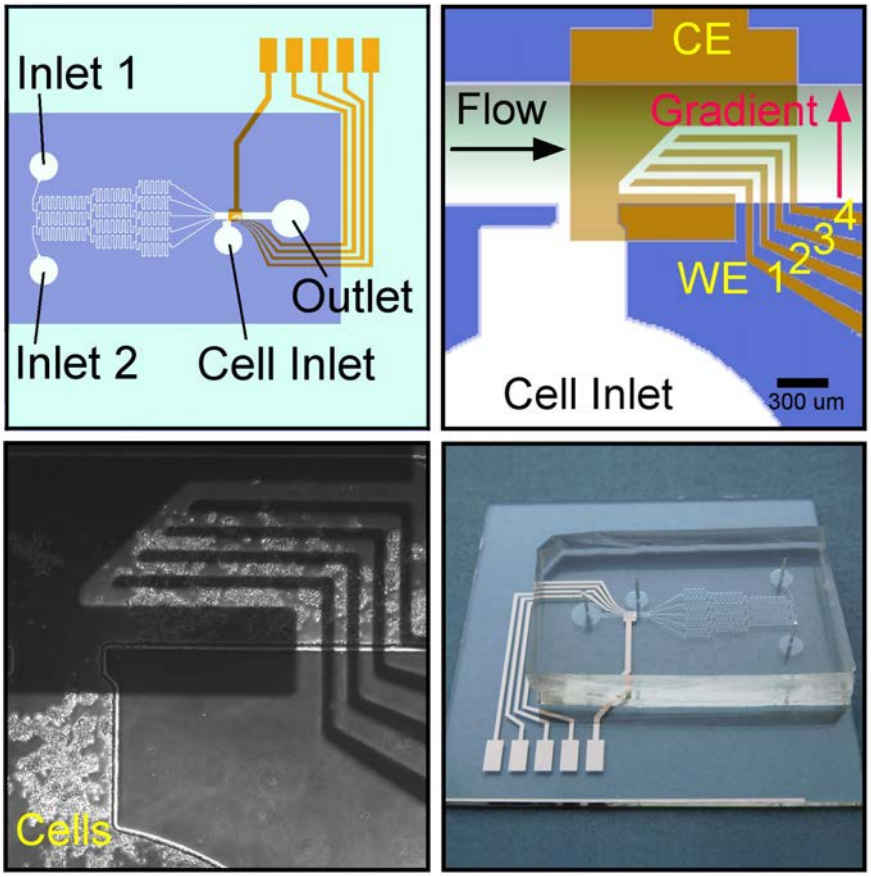

Figure 4.11 – Microfluidic chip-based chemotaxis assay with electrode stripe configuration in the flow channel of a concentration gradient generator. Top view of the whole chip and of the active part with 4 working electrodes (WE), counter electrode (CE) and the cell inlet connected to the main flow channel (upper panels). Phase contrast image of the chip with cells before the start of measurement and a front view photograph of the whole chip (lower panels).

Dictyostelium AX2-WT cells were cultured as described in the method section and prepared for experiments in the following way: to enhance the chemotactic sensitivity cells were resuspended in Soerensen buffer and stimulated with short pulses of cAMP every 6 minutes in a shaking culture. cAMP stimulation was performed for 3-5 hours and pulsed cells then immediately used for experiments.

For the electrode configuration shown in Fig. 4.11 equally spaced electrode stripes were placed parallel to the direction of flow in the flow channel of the concentration gradient generator (width 740 μm, height ca. 80 μm). Such an electrode configuration allows for studying migration of cells moving up the gradient, since electrodes with different positions along the vertical axis should display temporally separated impedance kinetics (increase of resistance), when cells leave the lower part of the channel and collect at the upper part. A series of such measurements were performed, two of which are shown in Fig. 4.12, were the same electrode configuration was tested with two different inlet-1 concentrations of cAMP: 1 μM (Fig. 4.12 A) and 2.5 μM (Fig. 4.12 B). Impedance kinetics of all four electrodes in both measurements display characteristic shapes with similar as well as different features. Common to all is the sharp rise in impedance during the first hour of measurement, which marks the attachment and spreading phase of *Dictyostelium* cells after seeding and distributing of the cell population in the flow chamber shortly before the start of measurement. When placed in the chamber, cells start to make contacts to the surrounding surface, thereby loosening cell-cell contacts and clusters and occupying free space by random movements (seen in Fig. 4.12 A and B, middle panels, showing more uniformly distributed cells than in the first panels). After the initial rise and decline (0h-2h) of impedance electrodes display differences in impedance kinetics, which are more pronounced in measurement B, where electrodes 3 (up to 7h) and 4 (up to 9h) show a slow increase, whereas electrodes 1 and 2 show a decrease. This is due to different initial cell positions of measurement A and B. In A, cells initially are distributed across the whole channel, i.e. all electrodes are covered by a similar amount of cells. In B, cells initially are mainly located in the lower part of the channel, i.e. electrodes 1 and 2 are more covered by cells than electrodes 3 and 4. Clearly, when cells move up the gradient, they leave electrode 1 and 2 and collect at electrodes 3 and 4.

The following conclusions were made concerning the observations given above and from other test experiments: 1. Impedance sensing microelectrodes work well under flow conditions in microfluidic channels. An increase of impedance is observed when electrode cell coverage increases and when cells make adhesive contacts to the substrate during the attachment and

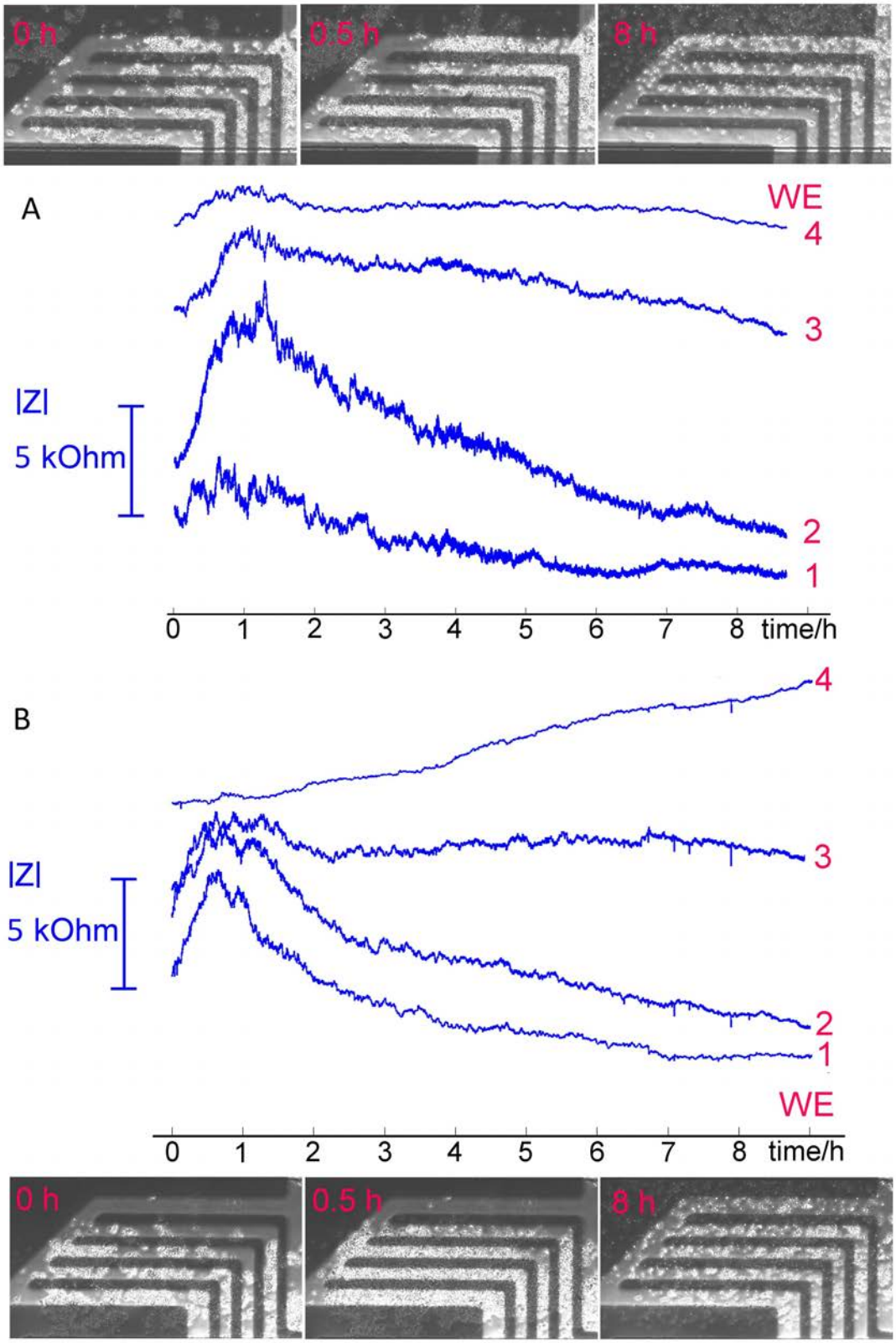

Figure 4.12 – Two mesurements where the electrode stripe configuration shown in Fig. 4.11 was tested. Phase contrast photographs depict the active part of the elcetrode array at indicated time points in the flow channel with cells moving up the gradient. Working electrodes (WE) 1-4 are numbered according to their position in the channel from bottom to top.

spreading phase. 2. There are critical parameters which limit the miniaturization of the measurement cell, notably the size of the electrodes, the distance between working electrodes and counter electrode and the height of the flow channel. Electrical noise and impedance, which are enhanced by reducing the size of microelectrodes, are further increased when the channel height is decreased and the distance to the counter electrode is increased. A too small channel height leads to a critical squeezing of the electrical field lines in the measurement cell, which strongly increases the impedance. We therefore reduced the WE-CE distance to 50 μm and increased the channel height to 80 μm, to compensate the increases in noise and impedance. To quantify our observations: when a relatively large WE (50000 $\mu m^2 = 0.05$ mm^2)is used, then the channel height can be held small (40-80 μm). If a further reduction of the WE size is required, than the channel height must be increased. 3. Impedance kinetics of electrodes 3 and 4 shown in Fig. 4.12 B display an increase in impedance when cells collect at the upper part of the flow channel. But cells enter these electrodes at different times, which makes the measurement of cell speed problematic. Thus, it should be regarded with respect to chemotaxis speed measurements that stronger and faster impedance changes are observed when cells enter an initially cell-free electrode about the same time. 4. It would be advantageous to place electrode stripes not *in direction*, but *perpendicular* to a micro channel, so that electrode leads are entirely covered by insulating PDMS. Such an electrode arrangement requires a concentration gradient *in direction* of the channel, which cannot be achieved by the above used gradient generator. Measurements with a suitable cAMP source, which establishes a gradient along a channel, are presented in section 4.3.3.

4.3.2 Cell sheet migration over circle-microelectrodes

ECIS 250μm-microelectrodes in open wells were successfully employed as wound healing assays, using 1000-fold currents (1mA) as in normal noninvasive operation mode, to create well-defined wounds in confluent cell layers and to monitor cell migration/proliferation rates in the ensuing healing process. These automated measurements replaced traditional scratch assays [73, 74]. Furthermore, an electric fence cell migration assay was designed, which works without the wounding step and which provides a cell-free electrode surface until a surrounding confluent cell layer has formed. The electric fence assay avoids the problem of possible cell remnants on the electrode surface after wounding.

Two ways of operation were realized using the arrangement of a cell reservoir connected to a stationary gradient flow chamber equipped with

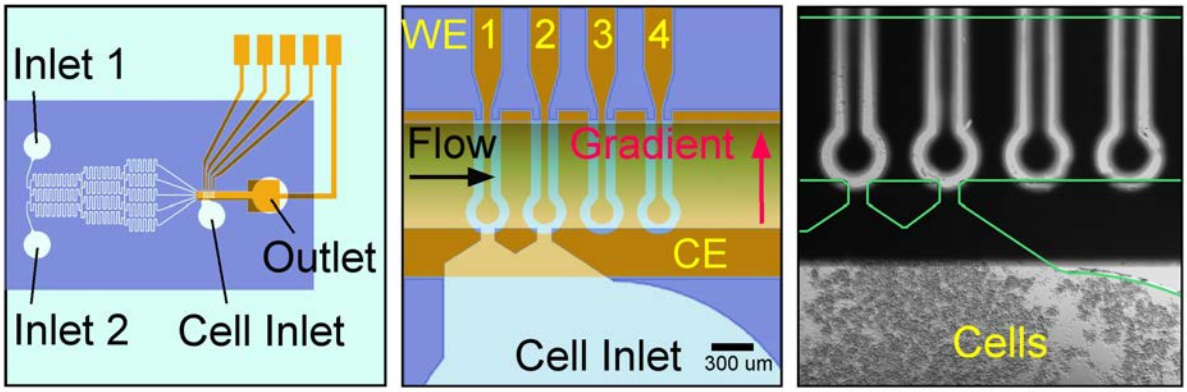

Figure 4.13 – Microfluidic chip-based chemotaxis assay with four circle microelectrodes placed in the flow chamber of a concentration gradient generator. Top view of the whole chip and of the active part (sketch and phase contrast photograph with cells) with 2 cell entrance channels connecting the cell reservoir with the flow channel. Electrodes 3 and 4 serve as control. Chemotactic cells from the reservoir sense cAMP molecules from the flow channel and are forced by the entrance channels to cross the circle electrodes when moving up the gradient.

impedance sensors as shown in Fig. 4.11 and Fig. 4.13. Firstly, cells were filled in the flow chamber to create an uniform cell density distribution across the whole flow channel (which was discussed in the previous section). Secondly, it was observed that some chemotactic well developed cell populations resting in the cell inlet reservoir migrated as cell sheets through the entrance channel to the neighboring gradient flow chamber.

The observation of occupation of an initially cell-free flow chamber by migrating cell sheets was employed to design an impedance based microfluidic cell migration assay by placing micro circle-electrodes in the flow chamber near cell reservoir entrance channels. Four working electrodes, surrounded in 70μm-distance by a large counter electrode, were aligned side-by-side downwards the flow channel, two of which were placed near 80μm wide cell entrance channels, the others were used as control and were separated from migrating cells (Fig. 4.13).

Experimental preparation and setup for the measurement of Fig. 4.14 was performed as follows: the prepared chip was clamped between Plexiglas plates and connected to the transimpedance amplifier device as described in section 4.3.1 and the methods section. Inlet 2 of the gradient generator was connected via tubing to a syringe pump and supplied with buffer flow only. Inlet 1 was initially closed with a stopper during the first step of filling the chip with buffer, to avoid the filling of the cell reservoir with cAMP. Cell inlet tube with cell syringe and outlet tube were already inducted during the first step of chip filling. Next cells were filled in the cell inlet so that cells remained in the cell reservoir near the entrance channels to

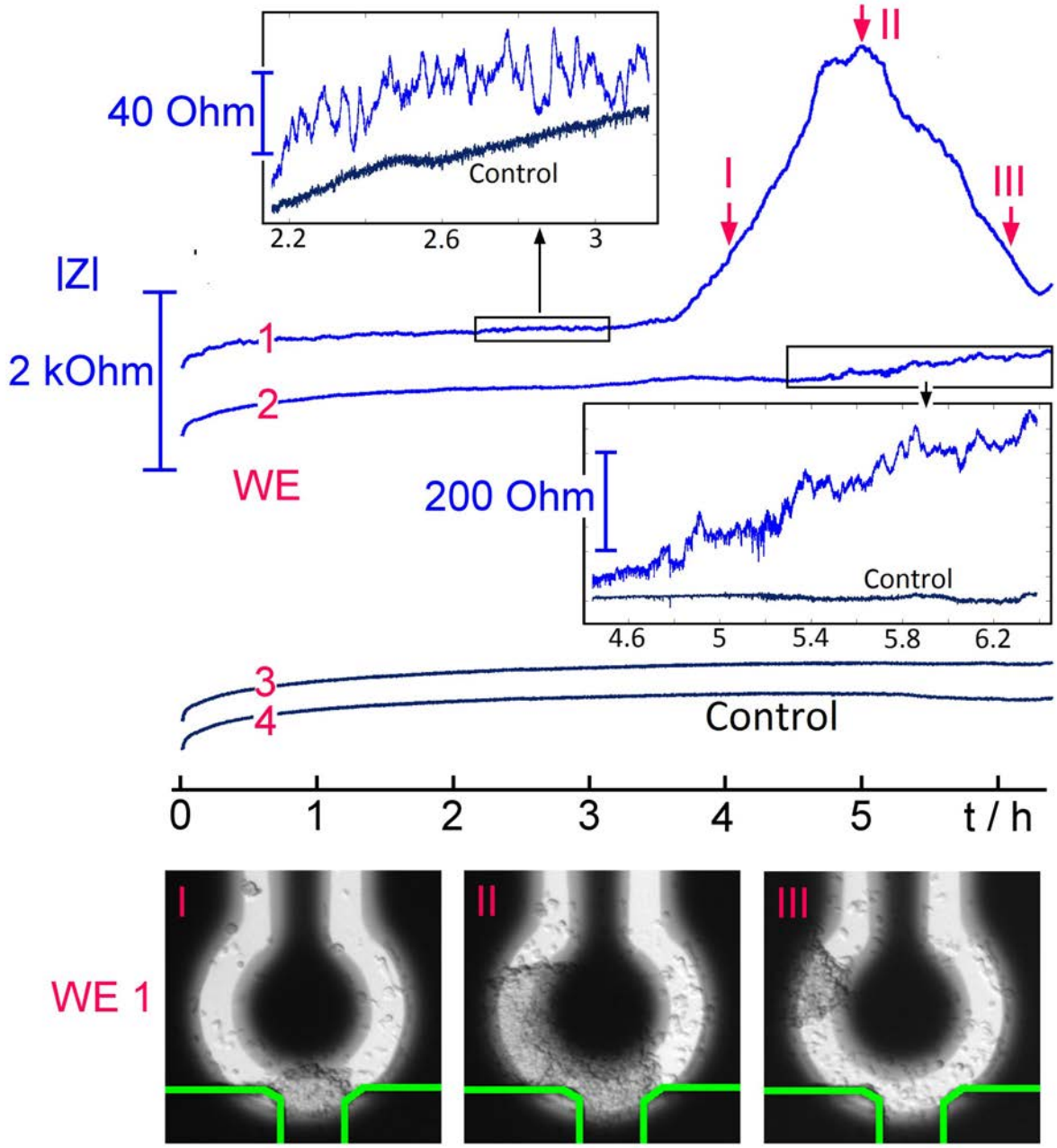

Figure 4.14 – Impedance mesurement where the circle electrode configuration shown in Fig. 4.13 was used. Phase contrast photographs depict the first electrode (WE 1) when crossed by a moving cell sheet (green lines depict the entrance channel). Insets show fluctuations from WE 1 and 2 caused by a few single cells, taking place on a much smaller scale than cell sheet overgrowth. WE 3 and 4 were used as control.

the flow chamber. Next the gradient generator was ready for operation. The stopper was removed and inlet 1 supplied via tubing and syringe pump with a flow of 20M-concentration of cAMP. cAMP and buffer flow were performed with the same syringe pump at 2μL/minute (i.e. 4μL/minute were flowing through the whole chip). Afterwards image acquisition and impedance recording were started.

After start of the measurement cells in the upper part of the cell reservoir orientated towards the entrance channels to the flow chamber. Images show that random movements turned into directed chemotactic motions during the first two hours of measurement. This process propagated through the whole cell population and was initiated by cells, which obviously sense cAMP molecules diffusing through the entrance channels into the cell reservoir. The amount of such diffusing molecules remains limited over time since they stem from the side of the flow channel with low cAMP concentration, which means that so long as the gradient is maintained no complete mixing will occur between fluids of flow channel and cell reservoir. The final cAMP concentration in the cell reservoir will not exceed the lowest cAMP concentration in the flow channel. Cells migrating to the first entrance channel formed a dense cell sheet in which individual cells were not visible. The propagating front of the cell sheet was forced by the small entrance channel to cross the 150μm-circle-electrode when moving to the higher cAMP concentration at the opposite side of the flow channel. This shows that chemotactic cell migration is a highly adaptive process, enabling cells to accurately find the source of environmental cues, which can be utilized to guide cells to certain locations in a micro-laboratory. The shape of migrating cell sheets and clusters can be formed by the geometry of microchannels.

From the recorded impedance kinetics the whole process of migrating cell sheets, clusters or streams as well as single cell movements can be discerned. The impedance trace of the first electrode (WE 1 in Fig. 4.14) encodes the electrode surface coverage and decoverage of a confluent cell layer (cell sheet), by which the free electrode area is continuously decreasing, rising the impedance to 117 percent of its value at the start of coverage (from 18 to 21 kOhm). Electrode coverage and decoverage both taking about 1.3 hours. Assuming that the distance travelled for coverage is of the order of the electrode diameter, one obtains for the velocity of an amoeboid cell sheet 150um/1.3h = 115um/h. The same holds for decoverage.

Also visible in impedance kinetics of Fig. 4.13 are fluctuations caused by the movement of single cells. This takes place on a scale 100 times smaller than that of surface coverage and is depicted in the insets of Fig. 4.14. The dynamics of cell overgrowth appears as the overall trend of impedance

kinetics, whereas single cell fluctuations constitute the small scale variations.

4.3.3 Creating a flexible cAMP micro-source by photo uncaging

An elegant way to overcome the problem of providing well-defined gradients to migrating cells is photo uncaging, meaning that a molecule can be rendered biologically inert ("caged") until its specific function (binding to a receptor) is switched on by photolysis [77]. This means among others that a well-placed molecule source in space and time can be created simply by illumination of caged compounds, which were already present in the bulk medium before, but were not recognized by cells. Combination of microfluidic device applications with photo uncaging of molecules is a promising research field, since handling of few molecules as well as arrangement of molecule masses can be directly performed near locations of biochemical reactions under investigation. For example, since the area of illumination can be restricted to arbitrary geometries, a well-defined gradient can be generated in a small laminar flow chamber without the need of a branched channel network outside the flow chamber for gradient preparation. For example, illumination of a triangle-(V-)shaped region in the flow channel generates a linear stationary gradient perpendicular to the flow direction, since in the upper region of the channel more molecules are uncaged and transported downstream than in the lower region due to the V-shaped illumination.

Preparation of molecular gradients in micro channels by photo uncaging can be also performed without flow, where transport of molecules is achieved only by diffusion. The creation of a constant molecule source is approximately achieved when only a small volume fraction of the micro channel is illuminated, so that the diffusive flux of uncaged molecules out of the illuminated region is balanced by the diffusive influx of caged molecules from the surrounding reservoir. The influx of caged molecules decreases with time due to a slow replacement of caged compounds in the reservoir by uncaged molecules, whose flux out of the uncaging region also slowly drops. Thus, when the illuminated region is small compared to the reservoir, then the concentration of uncaged molecules in the surrounding of the source only slowly increases and a gradient can be maintained over a certain time interval.

Experiments with photo uncaging were performed on an inverted microscope. A focused laser beam (UV laser, wavelength λ=355nm, Genesis series, COHERENT, Santa Clara, USA) was coupled in the optical path of the microscope and directed through the objective into a micro channel

through the bottom glass slide (electrode array) of the microfluidic chip shown in Fig. 4.15.

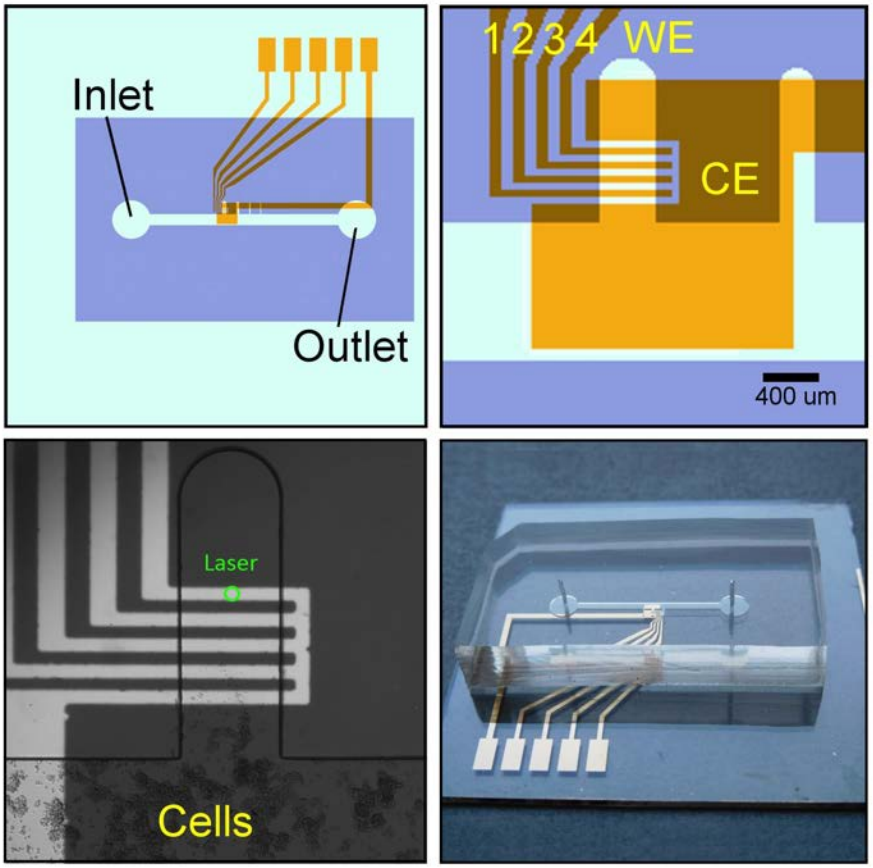

Figure 4.15 – Chip-based chemotaxis assay with electrode stripe configuration. Top view of the whole chip and of the active part with 4 working electrodes (WE) and counter electrode (CE)(upper panels). Phase contrast image of the chip with cells filled in the large horizontal channel. The position of the laser beam for photo uncaging is shown. Cells must traverse four electrode stripes to reach the cAMP source. Front view photograph of the whole chip (lower panels).

The chip was fabricated as described in sections 4.3.1, 4.3.2 and the methods section. The channel system consists of a broad horizontal channel (width 1 mm), connecting cell inlet and outlet, and a series of vertical channels, one of which was equipped with four electrode stripes at the entrance area to the horizontal channel. Length, width and height of the vertical channel was 1200 μm, 400 μm and 200 μm respectively. Microelectrode stripes were disposed perpendicular to the channel as seen in Fig. 4.15. Before start of measurement the laser spot (diameter 40-50 μm) was positioned 500-600 μm distant to the entrance area of the channel with electrode stripes in between. Then the laser shutter was closed and the whole chip was flooded with 10 μM BCMACM-cAMP in Soerensen buffer. Afterwards cells (3-4h pulsed with cAMP) were filled in the chip

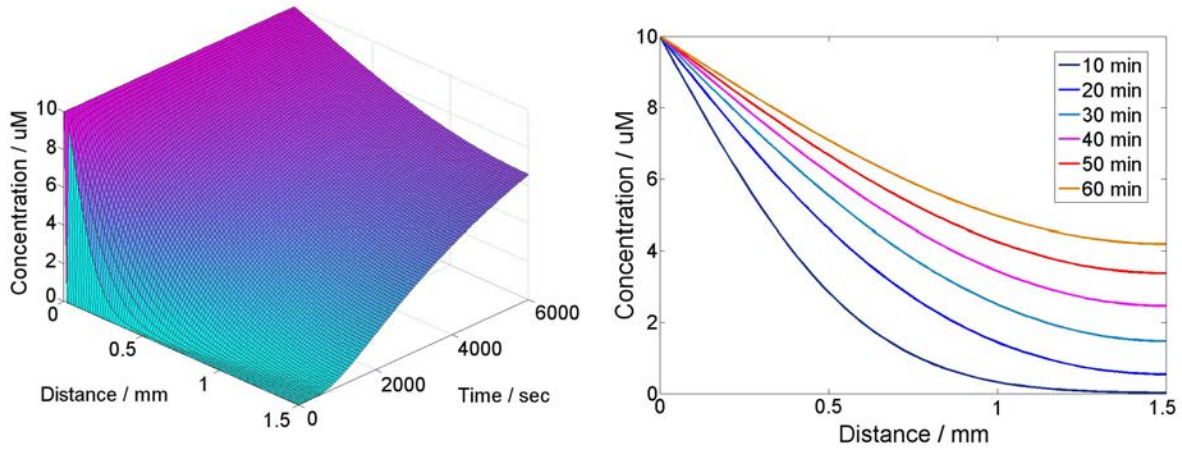

Figure 4.16 – 1-dimensional simulation of a non-stationary concentration profile from a constant source at the left side and no flux boundary condition at the right side.

and placed at the entrance area of the vertical channel. Finally impedance recording and image acquisition were started and the laser shutter opened. For image acquisition, the whole chip was illuminated from above with red light (wavelength 690 nm).

The concentration profile of the cAMP source and its variation in time was calculated as follows: the intensity of the laser beam was measured with an optical power meter (model 1918-R, NEWPORT, Irvine, California), by placing the sensor directly at the site of beam entrance above a microelectrode array without a piece of PDMS on top. The value 50 μW was measured for the lowest intensity level used in experiments. To calculate the percentage of radiation absorbed by the irradiated volume in the micro channel, the exponential absorption law $I_{trans} = I_0 \exp(-\alpha d)$ was related to the beer-lambert law $\log(I_0/I_{trans}) = \varepsilon_\lambda$ c d, where I_{trans} is the transmitted radiance, I_0 the incident radiance (=50 μW) and ε_λ the extinction coefficient, which can be read out from the extinction spectrum shown in the methods section (Fig. 3.11). The spectrum displays $\log(I_0/I_{trans})$, which was measured for a BCMACM-cAMP concentration of c=100 μM and sample thickness d=1 cm. The relation of the absorption coefficient α to the extinction coefficient is $\alpha = \varepsilon_\lambda$ c ln10. With a BCMACM-cAMP concentration of 10 μM, used in chip measurements, with a thickness of 200 μm (0.02 cm, given by the channel height), it turned out that most of the radiation was transmitted through the sample and only 0.4 percent of I_0 was absorbed. With the given cylinder-shaped irradiation volume (cylinder with 50 μm diameter and 200 μm height), the concentration of caged molecules and the absorbed energy, the number of photons per caged molecule can be calculated, giving 150 photons/molecule/second for an

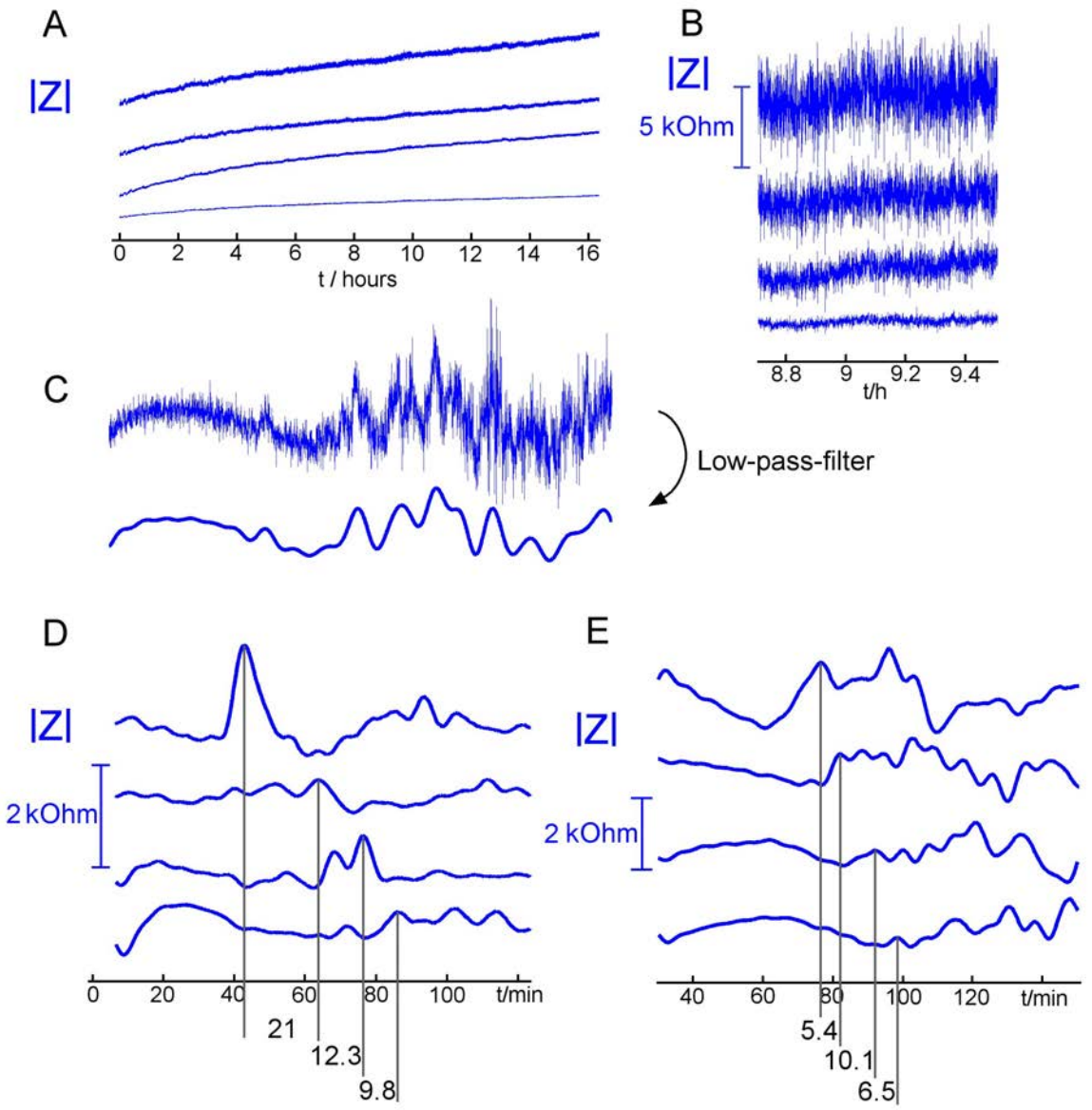

Figure 4.17 – Measurements were the chip shown in Fig. 4.15 was used. (A) Cell-free system with a channel height of 80 μm. (B) Enlarged view of impedance traces in A. Noisy signals stem from electrodes which were not properly working due to the small channel height. (C) Signal from a chip with increased channel height (200 μm) with smaller noise amplitudes. Signals were low-pass filtered to find the changes caused by cells. (D) Impedance traces of electrode stripes 1-4 (from top to bottom) belonging to the photographs shown in Fig. 4.18 (left). Time points were cells traversed the electrodes are marked by vertical lines. Numbers below the time axis are time intervals between vertical lines. (E) Impedance traces belonging to the photographs shown in Fig. 4.18 (right).

incident energy of 50 μW. This shows that the lowest laser energy used was high enough to uncage all caged compounds in the irradiation volume.

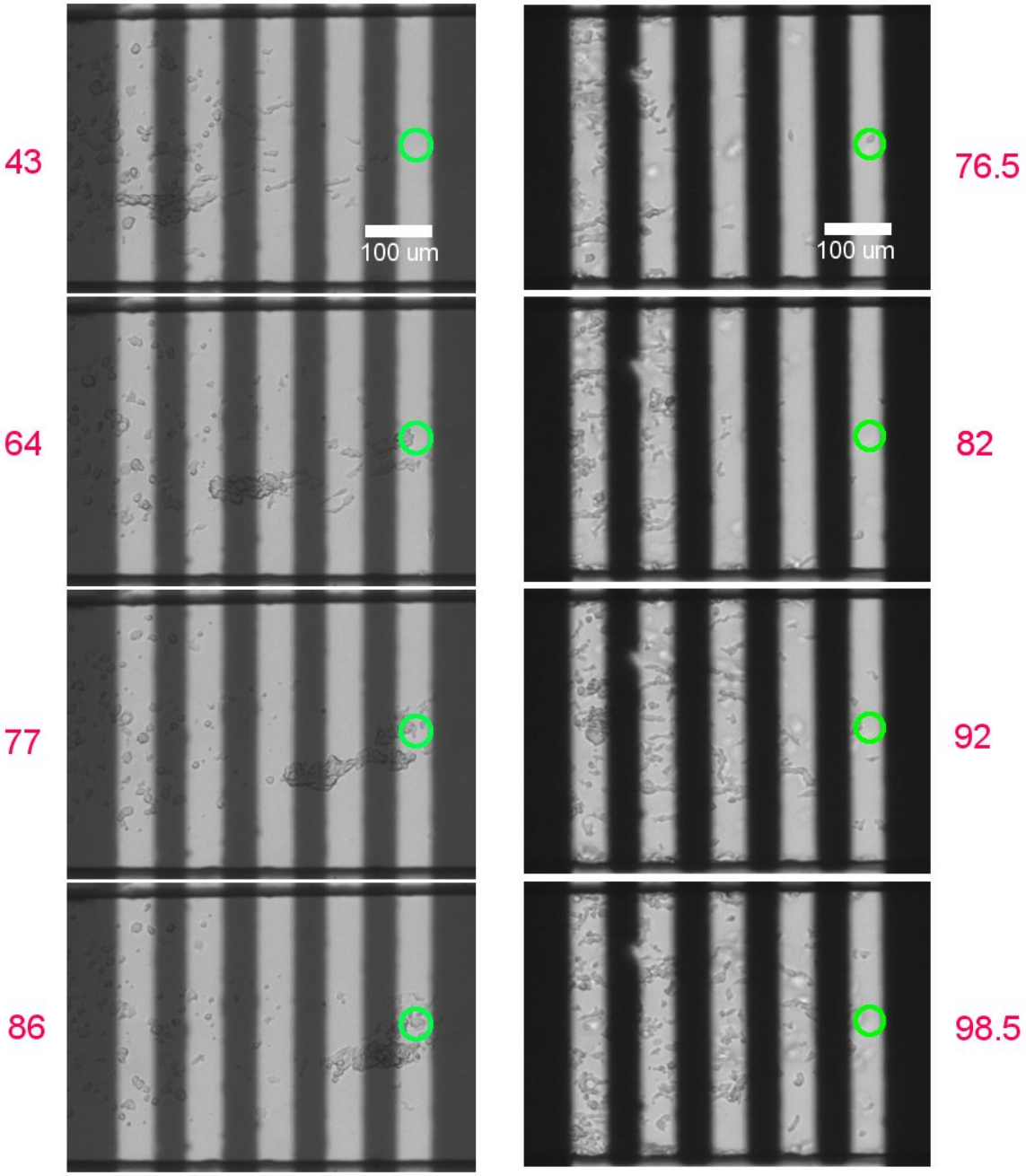

Figure 4.18 – Photographs belonging to impedance kinetics shown in Fig. 4.17D and E. Numbers left and right indicate time points when photographs were taken. Green circles mark the position of the laser spot and cAMP source. Cells move from left to right to reach the source.

Fig. 4.16 shows the non-stationary onedimensional concentration profile

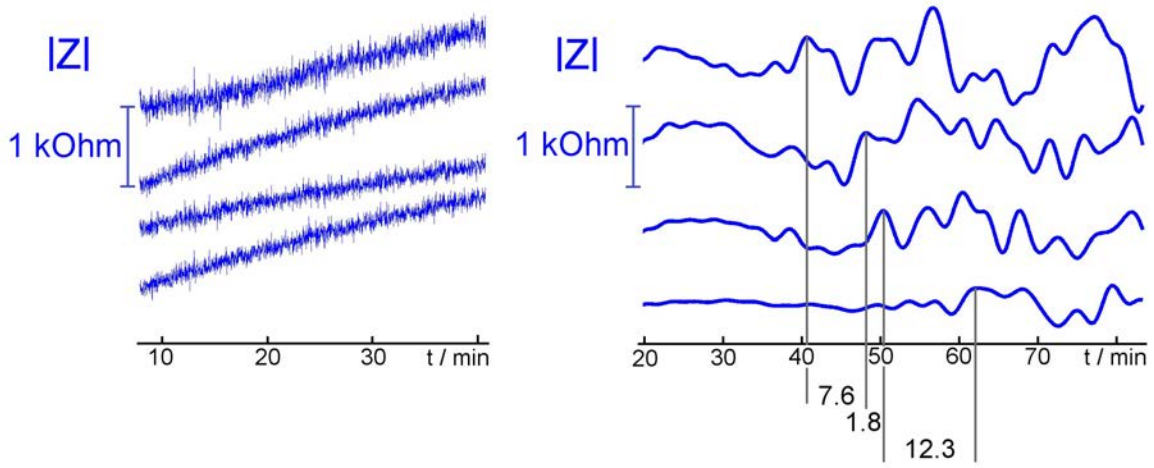

Figure 4.19 – Measurement with a chip with compact electrode arrangement. Impedance time traces belong to the photographs shown in Fig. 4.20. Cell-free system (left). High-pass filtered signals of the system with cells (right). Time points were cells traversed the electrodes are marked by vertical lines. Numbers below the time axis are time intervals between vertical lines.

and its time evolution, computed from the diffusion equation $c_t = Dc_{xx}$, with the assumption of a constant 10μM-molecule source. For calculation, we used the matlab solver 'pdepe' with suitable boundary conditions (constant concentration on the left boundary (source) and no flux at the right boundary. The right boundary was assumed to be 1.5 mm away from the left boundary to match the experimental condition of a micro channel wall opposite to the source). As mentioned above, this assumption of a constant source holds only when uncaged molecules, diffusing out of the irradiated volume, are immediately replaced by caged molecules from the surrounding reservoir. The diffusion coefficient D for cAMP molecules was estimated from the Stokes-Einstein relation, $D = k_B T/(6\pi\eta R) \approx 2\times10^{-6}$ cm^2/sec (k_B=1.38$\times10^{-23}$ J/K: Boltzmann constant, T=300 K: absolute Temperature, η=1mPas: viscosity of water at 20°C, R=1 nm: radius of the particle).

The arrangement of a constant cAMP source, providing a non-stationary diffusive cAMP gradient in direction of a micro channel, and spatially disposed electrode stripes perpendicular to the channel, was employed to create the electrical cell migration assay shown in Fig. 4.15. Fig. 4.17 A and B shows a test measurement of impedance kinetics without cells. Long-time series of the magnitude of Z show noisy signals with different noise strength, indicating that not all electrodes were properly working. With an increased channel high of ca. 200 μm and electrode sizes of 400$\times$50 μm time signals normally displayed noise amplitudes of ca. 1 kOhm. Such signals were low-pass-filtered to extract impedance changes caused by cell

Table 4.1 – Cell migration speeds in μm/min

Measurement	v_{21}	v_{32}	v_{43}	v_{41}
1	11.0	6.5	5.7	7.1
2	4.8	8.1	10.2	7.0
3	18.5	9.9	15.4	13.6
4	10.9	15.1	11.6	12.3
5	13.2	56.6	8.2	13.9

activity, shown in Fig. 4.17 C.

Fig. 4.17 D and E show impedance measurements belonging to the photograph series of Fig. 4.18. Cells in the micro channel sense diffusive cAMP molecules after switching on the source by photo uncaging. When cells move towards higher concentrations of molecules, they must pass four planar electrode stripes on the way to the source. Electrode stripes are spaced by equal distances of 100 μm, allowing to capture chemotaxis speeds of migrating cells by recording impedance kinetics of electrodes. Migrating single cells or clusters of cells produce peaks in the measured impedance kinetics when crossing the surfaces of planar electrode stripes. By relating the impedance peaks of consecutive electrodes, the time intervals for travelling a 100 μm-distance can be extracted. Deviations in the travelled distance due to finite widths of electrode stripes cause measurement errors. The smaller the distance between related electrodes, the larger the measurement error.

Besides the measurements with conventional electrode arrangement we show in Fig. 4.19 a measurement with compact electrode arrangement as described in the methods section 3.11 (Fig. 3.8). Impedance traces of Fig. 4.19 belong to the photograph series of Fig. 4.20, showing four electrode stripes on the bottom of the chip, which are not surrounded by a counter electrode as in the measurements of Fig. 4.18. The counter electrode is reinserted as the ceiling of the chip.

In table 4.1 measured velocities of chemotactic AX2-WT cells from five measurements under equal conditions with conventional electrode arrangement (measurement 1-4) and with compact electrode arrangement (measurement 5) are listed. Velocities of column 2-4 are calculated by relating consecutive electrodes: v_{21}=100 μm/(t_2-t_1), v_{32}=100 μm/(t_3-t_2), v_{43}=100 μm/(t_4-t_3), where the timepoints t_i (the index i=1,2,3,4 numbers the electrodes from left to right in Fig. 4.18 and Fig. 4.20) are extracted from impedance traces, three of which are shown in Fig. 4.17 and Fig. 4.19. Velocities of column 5 are derived from electrodes with the largest distance, v_{41}=300 μm/(t_4-t_1).

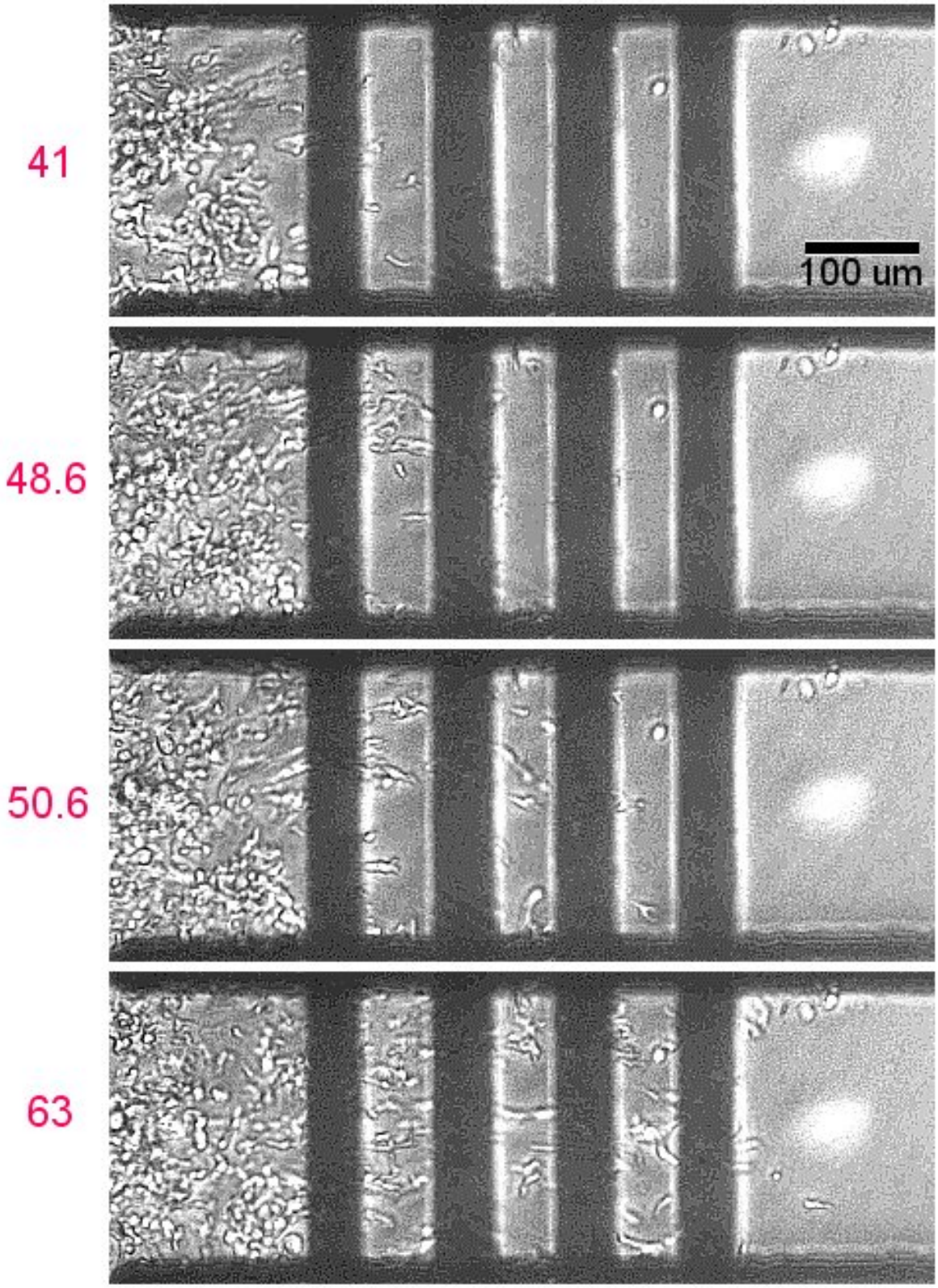

Figure 4.20 – Chip with compact electrode arrangement. Photographs belonging to impedance kinetics shown in Fig. 4.19. Numbers indicate time points when photographs were taken. The position of the laser beam (cAMP source) is visible as a white spot. Cells move from left to right to reach the source.

5 DISCUSSION

In this experimental study, single cells of *Dictyostelium discoideum* AX2 Wild Type and four mutant strains, *tal*A$^-$, *nap*A$^-$, *amp*A$^-$ and *GFP-α-tubulin* were measured using a custom designed cell-substrate impedance sensor, which allowed for simultaneous recording of impedance data and for video microscopy. Cell-shape changes were captured by timelapse microscopy, allowing us to relate such events to changes in the kinetics of the impedance. By fitting a model we show that cell-substrate interactions must be involved. For our analysis we collected more than hundred impedance time-series of vegetative wild type cells and four mutant strains with altered cell-substrate adhesiveness (*talA*$^-$, *napA*$^-$, *ampA*$^-$ and *GFP-α-tubulin*). The magnitude of impedance fluctuations differs for the adhesion-deficient mutants and is correlated with the order of increasing adhesion strengths of these cell lines that are determined independently in a shear stress detachment assay and with single cell force spectroscopy (cantilever picking). We have also developed a model to describe collective behavior of aggregating *Dictyostelium* cells and its reflection in the occurence of impedance spike trains. Chemotactic cell movement was measured by developing the concept and experimental setup of an electrical cell migration assay. In the following these topics are discussed.

5.1 Influence of mutations on cell substrate adhesion

We chose *D. discoideum* mutant strains according to their different cell-substrate adhesiveness compared to AX2-WT cells. Talin is one of the actin binding proteins which anchors filamentous actin to the plasma membrane. Phenotypic alterations of *tal*A$^-$ cells include larger cell sizes, a more 'blebbing'-like shape than wild type and weaker adhesion to surfaces [49]. The protein *nap*A was shown to be involved in regulation of actin nucleation. Knockout mutants of *nap*A, made by homologous recombination in wild type strain AX3, have a smaller and more rounded shape than the wildtype, chemotax slower, protrude smaller pseudopods, and have defects in cell-substrate adhesions [98]. The protein *amp*A (Adhesion Modulation

Protein A) plays a role in cell migration and adhesion during development. For *amp*A knockout mutants an increased substrate adhesion was reported. The vegetative *amp*A null cells were largely unable to migrate toward folic acid and they protrude fewer and more rounded pseudopods. Consistently, *amp*A$^-$ cells polymerize less actin while over expressing cells polymerize more actin than wild type [99]. In our detachment assay, *amp*A$^-$ showed a weaker substrate adhesion strength than the wild type, in contrast to the magnitude of impedance fluctuations and the maximal adhesion force measured by cantilever picking, which assessed *amp*A$^-$ cells as stronger adhesive than wild type.

5.2 Impedance time series encode cell shape and adhesion dynamics

Surface-attached single motile amoeboid cells undergo oscillatory shape changes. Alternating protrusion and retraction constitute a motility cycle, which appears as the basic pattern of all forms of movement and taxis over various substrata [100]. This process is associated with the formation of adhesion sites.

Thus, the motility of amoebae can be seen as a combination of (1) *shape oscillations* due to periodic increase (protrusions) and decrease (retractions) of the projected cell area and (2) *cell-substrate interactions*, comprising the formation of traction stress patterns, adhesion regions and possibly other events taking place in the cell-substratum gap.

In our experiments, all impedance time series of single vegetative amoebae are characterized by irregular oscillations. Successive minima of oscillations correspond to a compact cell shape as the start/end point of a motility cycle. An impedance model reveals that indeed the projected cell area is encoded in these long-term trends of the impedance kinetics. Characteristic scales of the motility cycles and their alteration over time were uncovered by computing wavelet scalograms, as described in the methods and results. The most persistent scales were obtained by time-averaging the scalograms.

Superposed to these oscillatory long-term trends, we observed fluctuations in the impedance signal. In order to quantify the impedance fluctuations, we subtracted a linear fit from our data and computed standard deviations of the resulting signals (Fig. 4.6) as a measure of the amplitude of fluctuations. By comparison with two independent adhesion assays, we found that the amplitude of impedance fluctuations correlates with the adhesion strength.

Taken together, all methods shown in Fig. 4.6 reveal *GFP-α-tubulin*, AX2-WT, and *amp*A$^-$ as the strongest adhesive cell lines. Within this

group, impedance fluctuations and the maximal adhesion force (Fig. 4.6 A, D) assess *amp*A$^-$ as the strongest adhesive cell line. In the shear stress detachment assay, this is the case for *GFP-α-tubulin* cells. All methods produced consistent results regarding the group of cell lines with weak adhesion strength, *nap*A$^-$ and *tal*A$^-$.

We conjecture that the fluctuations are associated with the formation of localized cell-substrate adhesion sites. The correlation of fluctuation magnitude and adhesion strength suggests that cells with more dynamic cell-substrate interactions are less prone to detachment. Reflection interference contrast microscopy confirms that adhesion relies on regions of contact between the ventral cell membrane and the substrate and does not depend on the projected cell area. However, the fluctuating dynamics of individual adhesion sites within these contact regions cannot be resolved with this method.

In contrast to the correlation between fluctuations and adhesion strength, differences between the motility cycle periods of the different cell lines are not statistically significant (see Fig. 4.6 B and C). This suggests that the adhesion strength of a cell does not affect its motility cycle period (except the cases of very weak or strong adhesion). A possible interpretation of this observation is that soil-living *Dictyostelium* amoebae have to cope with a variety of substrates of different adhesiveness, where maintenance of a robust motility cycle is an important function for survival under these conditions.

In future work, we will focus on the relation between fluctuations in the impedance signal and periodic dynamics in the actin cytoskeleton [101]. Also the relation to random components in the cell trajectories will be explored [102–104].

5.3 Modelling impedance spike trains

When a cell-substrate impedance sensor (microelectrode) is placed in the aggregation plane of a population of starved amoebae, then impedance spike trains are observed in the recorded impedance kinetics. In section 4.2.2 we have developed a model to capture the emergence and decay of these spike trains as observed in measurements.

The impedance formula of Giaever and Keese depends on morphological parameters of a cell, which is described as a floating disc with radius r_c and substrate distance h. This formula is suitable to model the cell-substrate impedance $z(r_c,h)$ of a single cell. To model synchronization on the population level, we used kinetic equations of Martiel and Goldbeter describing the cAMP signalling system [93]. These kinetic equations can

be used to model a coupled ensemble of noise-driven excitable oscillators. The global cAMP output of this system displays well-known properties of excitabilty such as coherence resonance, i.e. the occurence of most coherent oscillations at intermidiate noise levels. We have coupled the morphological parameters of a single cell to the cAMP signalling system by relating radius and substrate distance to the receptor variable (the fraction of receptors in active state). Then we computed the impedance of a system of coupled cAMP oscillators as the overall impedance of a parallel circuit of single cell impedances.

With the given model system different scenarios can be realized leading to sustained oscillations of the ensemble impedance (Fig. 4.10). Alternating supra- and subtreshold noise levels produce spike trains with supressed phases in between spikes (Fig. 4.10 D, E). Increasing noise levels combined with global coupling or a low constant noise level combined with cAMP accumulation both lead to a phase transition to coherent oscillations, an increase of oscillation frequency, a decrease of oscillation amplitude and final decay of oscillations as observed in experiments (Fig. 4.10 F, G).

We note that the core principle of the model is the coupling of the impedance to changes in cell morphology, which as constituents of the motility cycle are in turn coupled to the cAMP signalling system. This concept can be further developed and extended, which was beyond the scope of this thesis. For example, the changes in morphology can be decomposed in 1. shape oscillations (kinetics of the projected area), 2. kinetics of the substrate contact area (as seen in RICM) and 3. kinetics of close contact zones or specific substrate interactions (or unspecific interactions in the case of *Dictyostelium*). This decomposition implicates that different dynamic regions with different cell-substrate separations exist beneath an interfaced motile cell. The question is how the dependence of the impedance on these morphological changes can be modeled. Up to date, the Giaever-Keese impedance formula is the only model which includes an explicit dependence of the impedance on the morphological parameters r_c and h. For the above given decomposition of the projected cell area A in sub-regions A_i with different substrate separations h_i (i=*1,2,3*), this means that a mean substrate distance h must be calculated when using the Giaever-Keese impedance formula, given by the weighted sum of substrate separations h_i: $h = \frac{A_1}{A}h_1 + \frac{A_2}{A}h_2 + \frac{A_3}{A}h_3$ (which holds when $A = A_1+A_2+A_3$).

5.4 Electrical detection of chemotactic cell migration

Microfluidic device fabrication has become a major aprroach in biosciences to include laboratory tasks into confined micro spaces using laminar flow channels and the biocompatibility of PDMS to provide suitable microenvironments for the study of cellular functions. The future of microfluidics lies in the development of highly integrated microdevices with respect to measurements of single cells [30, 71]. This means that the fabrication process of integrated chips will be more challanging and that requirements for laboratory equipment will increase.

Besides various traditional methods to capture chemotaxis of cultured cells there are few electrical methods based on ECIS, which have in common that sensors are placed in open wells or culture dishes. The aim of the current experimental work presented in section 4.3 was the integration of cell-substrate impedance sensors into a chip-based microfluidic system, which provides a well-defined chemoattractant gradient to small groups or clusters of chemotactic cells. This kind of chip-based electrical chemotaxis assay is capable to trace and monitor the chemotactic activity of weakly surface-attached motile cells such as *Dictyostelium discoideum*.

We used surface patterning techniques for the construction of electrical chemotaxis assays. A standard photolithography liftoff technique in combination with sputter coating was used to fabricate microelectrode arrays as the substrate for a system of micro channels embossed in a piece of PDMS via soft lithography (replica molding). The sealing of the micro channel system, which is normaly done by plasma bonding, was achieved by clamping the chip between two plastic plates. This construction is advantageous, since it allows the mounting of spring contact pins in the upper plate for contacting electrode pads and the repeated usage of electrode arrays after measurement.

The essential task for quantifying directional sensing of chemotactic cells is the preparation of a chemical concentration gradient. Microfluidic gradient generators establish spatially and temporally stable concentration gradients *perpendicular* to the direction of flow in a microchannel. As pointed out in section 4.3.1 we searched for a method to generate a concentration gradient *in direction* of a microchannel. In principle, a simple H-structure, connecting two vertical flow channels with a high and a low concentration by a horizontal gradient channel, should generate such a gradient along the horizontal channel by diffusion between the vertical flow channels. The condition for a stable diffusive gradient is that no flow will pass the connecting horizontal channel. But in practice it is difficult to realize since

the gradient turns out to be unstable due to smallest differences in flow pressure of vertical channels, which undermines a stable flow equilibrium even when a pressure-controlled pump is used. In [105] this problem was solved by diminishing the channel height of the horizontal channel to a few micrometer, but this would be not practicable when introducing microelectrodes. Also, a flow-preventing wall, permeable only for diffusing molecules, could be placed into the horizontal channel at the side of high concentration. This method would be interesting for its own, but would complicate the fabrication process and increase costs.

Photolysis of caged compounds was the method of choice for gradient preparation as described in sections 3.12 and 4.3.3. This technique has great potential in combination with microfluidics: it allows to place a molecule source at any location in a microchannel without the need of further space for gradient preparation; chemotactic cells in the surrounding immidiatedly start to reach the source when switching it on; it can be applied with or without a flow. We tested this method successfully in combination with spatially disposed microelectrodes and measured the position of migrating cells on their way to the cAMP source. Time-resolved signals of four different electrodes were related to calculate migration speeds (table 4.1) with a mean value of 11 ± 4 μm/min. Furthermore, we searched for experimental solutions for miniaturization of the measurement chamber and have succesfully designed a chip with compact electrode arrangement as described in section 3.11. Future development could include the use of impedance-optimized microelectrodes for further miniaturization with respect to single cell measurements, the use of microelectrode arrays to measure many single cells simultaneously or the fabrication of multifunctional platforms integrating electrical and other types of sensors or tasks in a single device.

Most of our work was concerned with the steps of fabrication, the experimental realization and ongoing studies of technological principles and pitfalls. Much patience is needed to cope with electrical measurements of biological samples. Up to date we are able to present a prototype of an electrical chemotaxis assay and a 'proof of concept', but much future work has to be done with regard to miniaturization, multifunctionality, high throughput and ease of operation.

Appendix

In the following we list the parameter values used in the simulations shown in Fig. 4.10 for the Martiel-Goldbeter model (eq. 4.5 and 4.6 in section 4.2.2) and the Gieaver-Keese impedance model (eq. 2.3 in section 2.3).

Martiel-Goldbeter model: ϵ=0.01, s=45, λ_1=0.001, λ_2=2.4, κ=12.5, L_1=10, L_2=0.005, c=1. To match spike intervals of 5-12 minutes observed in experiments, the functions $f_{1,nm}$ and $f_{2,nm}$ were multiplied with the factor q=0.05. Noise and coupling strengths used are given in the text and figure captions.

Giaever-Keese impedance model: the membrane impedance Z_m was modelled according to eq. 2.4 in section 2.3 with R_m=10000 Ωcm^2, C_m=1 $\mu F/cm^2$ and ω=2π4000 Hz. The impedance of the cell-free electrode, Z_n, was modelled as a resistor and capacitor in series with R_n=500 Ωcm^2 and C_n=0.2 $\mu F/cm^2$. The resistivity of the solution was ρ=500 Ωcm and the junctional resistance R_s=1 Ωcm^2. As described in section 4.2.2, cell radius and substrate distance were coupled to the receptor variable according to $r_{c,nm}(t) = A\varrho_{nm}(t) + B$ and $h_{nm}(t) = E\varrho_{nm}(t\text{-}\tau) + F$. For this, the constants A=3.8$\times 10^{-4}$cm, B=3.26$\times 10^{-4}$cm, E=2$\times 10^{-5}$cm, F=-9.1$\times 10^{-6}$cm and τ=1.85 min were used in the simulations shown in Fig. 4.10 C, E, F. For the simulation shown in Fig. 4.10 G, radius and substrate distance were coupled to the function Φ_{nm}, i.e. $r_{c,nm}(t) = A\Phi_{nm}(t) + B$ and $h_{nm}(t) = E\Phi_{nm}(t\text{-}\tau) + F$, with A=-7.5$\times 10^{-4}$cm, B=6.5$\times 10^{-4}$cm, E=-3.8$\times 10^{-5}$cm, F=8$\times 10^{-6}$cm and τ=1 min.

Numeric integrations of kinetic equations were done with an Euler scheme with time increment Δt=0.005.

Bibliography

[1] J.M. Kita, R.M. Wightman, Curr. Opin. Chem. Biol. **12(5)**, 491 (2008).

[2] B. Alberts, A. Johnson, J. Lewis, M. Raff, K. Roberts, M. Walter, Garland Science, 4th edition, New York (2002).

[3] R. Pethig, D.B. Kell, Phys. Med. Biol. **32(8)**, 933 (1987).

[4] H. Morgan, T. Sun, D. Holmes, S. Gawad, N.G. Green, J. Phys. D. Appl. Phys. **40**, 61 (2007).

[5] K. Burridge, K. Fath, T. Kelly, G. Nuckolls, C. Turner, Ann. Rev. Cell Biol. **4**, 487 (1988).

[6] B.M. Gumbiner, Cell **84(3)**, 345 (1996).

[7] C.S. Izzard, L.R. Lochner, J. Cell Sci. **21**, 129 (1976).

[8] I. Giaever, C. R. Keese, Proc. Natl. Acad. Sci. USA **88**, 7896 (1991).

[9] I. Giaever, C. R. Keese, Proc. Natl. Acad. Sci. USA **81**, 3761 (1984).

[10] I. Giaever, C.R. Keese, IEEE Transactions on Biomedical Engineering **33(2)** 242 (1986).

[11] I. Giaever, C. R. Keese, Proc. Natl. Acad. Sci. USA **89**, 7919 (1992).

[12] I. Giaever, C.R. Keese, Nature **366**, 591 (1993).

[13] C.-M. Lo, C. R. Keese, I. Giaever, Experimental Cell Research **204**, 102 (1993).

[14] P.M. Ghosh, C. R. Keese, I. Giaever, Biophys. J. **64**, 1602 (1993).

[15] C.-M. Lo, C. R. Keese, I. Giaever, Experimental Cell Research **213**, 391 (1994).

[16] C.-M. Lo, C. R. Keese, I. Giaever, Biophysical Journal **69**, 2800 (1995).

[17] J. Wegener, C. R. Keese, I. Giaever, Experimental Cell Research **259**, 158 (2000).

[18] C. R. Keese, K. Bhawe, J. Wegener, I. Giaever, BioTechniques **33**, 842 (2002).

[19] R.H. Kessin, Cambridge University Press (2001).

[20] E. Schäfer, C. Westendorf, E. Bodenschatz, C. Beta, B. Geil, A. Janshoff, Small **7**, 723 (2011).

[21] E. Schäfer, M. Tarantola, E. Polo, C. Westendorf, N. Oikawa, E. Bodenschatz, B. Geil, A. Janshoff, PLoS ONE **8**, e54172 (2013).

[22] See the website www.dictybase.org.

[23] K.F. Swaney, C.-H. Huang, P.N. Devreotes, Annu. Rev. Biophys. **39**, 265 (2010).

[24] G. Amselem, M. Theves, A. Bae, C. Beta, E. Bodenschatz, Phys. Rev. Lett. **109**, 108103 (2012).

[25] S. Morgenthaler, S. Lee, S. Zürcher, N.D. Spencer, Langmuir **19(25)**, 10459 (2003).

[26] T. Kraus, R. Stutz, T.E. Balmer, H. Schmid, L. Malaquin, N.D. Spencer, H. Wolf, Langmuir **21**, 7796 (2005).

[27] J.C. McDonald, D.C. Duffy, J.R. Anderson, D.T. Chiu, H. Wu, O.J.A. Schueller, G.M. Whitesides, Electrophoresis **21**, 27 (2000).

[28] S.K.W. Dertinger, D.T. Chiu, N.L. Jeon, G.M. Whitesides, Anal. Chem. **73**, 1240 (2001).

[29] S. Kim, H.J. Kim, N.L. Jeon, Integr. Biol. **2**, 584 (2010).

[30] G.M. Whitesides, Nature **442**, 368 (2006).

[31] See the website www.allaboutcircuits.com.

[32] E. Barsoukov, J.R. McDonald, John Wiley Sons Inc., 2nd edition (2005).

[33] H.G.L. Coster, T.C. Chilcott, A.C.F. Coster, Bioelectrochemistry and Bioenergetics **40**, 79 (1996).

[34] D.A. Borkholder, Dissertation (1998).

[35] E.T. McAdams, J. Jossinet, Bioelectrochemistry and Bioenergetics **40**, 147 (1996).

[36] R. Höber, Arch. Ges. Physiol. **133**, 237 (1910).

[37] H. Fricke, S. Morse, J. Gen. Physiol. **9**, 153 (1925).

[38] H.P. Schwan, Adv. Biol. Med. Phys. **5**, 147 (1957).

[39] J.D. Robertson, Prog. Biophys. **10**, 343 (1960).

[40] K.R. Foster, Annu. Rev. Biomed. Eng. **4**, 1 (2002).

[41] T. Sun, H. Morgan, Microfluid Nanofluid **8**, 423 (2010).

[42] C.-M. Lo, M. Glogauer, M. Rossi, J. Ferrier, Eur. Biophys. J. **27**, 9 (1998).

[43] M. Sabouri-Ghomi, Yi Wu, K. Hahn, G. Danuser, Curr. Opin. Cell Biol. **20**, 541 (2008).

[44] R. Zaidel-Bar, S. Itzkovitz, A. Ma'ayan, R. Iyengar, B. Geiger, Nat. Cell Biol. **9**, 858 (2007).

[45] I. Kaverina, O. Krylyshkina, J.V. Small, Int. J. Biochem. Cell Biol. **34**, 746 (2002).

[46] J.D. Humphries, A. Byron, M. J. Humphries, J. of Cell Sci. **119**, 3901 (2006).

[47] H. Wolfensohn, Y. I. Henis, B. Geiger, A. D. Bershadsky, Cell Mot. Cytoskel. **66**, 1017 (2009).

[48] B. Geiger, J. P. Spatz, A. D. Bershadsky, Nat. Rev. Mol. Cell Biol. **10**, 21 (2009).

[49] J. Niewöhner, I. Weber , M. Maniak, A. Müller-Taubenberger, G. Gerisch, J. Cell Biol. **138**, 349 (1997).

[50] S. Cornillon, E. Pech, M. Benghezal, K. Ravanel, E. Gaynor, F. Letourneur, F. Brückert, P. Cosson, J. Biol. Chem. **275**, 34287 (2000).

[51] P. Fey, S. Stephens, M. A. Titus, R. L. Chisholm, J. Cell Biol. **159**, 1109 (2002).

[52] T. R. Varney, E. Casademunt, H. N. Ho, C. Petty, J. Dolman, D. D. Blumberg, Dev. Biol. **243**, 226 (2002).

[53] S. Cornillon, L. Gebbie, M. Benghezal, P. Nair, S. Keller, B. Wehrle-Haller, S. J. Charette, F. Brückert, F. Letourneur, P. Cosson, EMBO reports **7**, 617 (2006).

[54] I. Weber, E. Wallraff, R. Albrecht, G. Gerisch, J. Cell Sci. **108**, 1519 (1995).

[55] K. S. K. Uchida, S. Yumura, J. of Cell Sci **117**, 1443 (2004).

[56] B. Alvarez-Gonzalez, R. Meili, E. Bastounis, R.A. Firtel, J.C.Lasheras, J.C. del Alamo, Biophys. J. **108**, 821 (2015).

[57] E. Decave, D. Garrivier, Y. Brechet, B. Fourcade, F. Bruckert, Biophys. J. **82**, 2383 (2002).

[58] E. Decave, D. Garrivier, Y. Brechet, F. Bruckert, B. Fourcade, Phys. Rev. Lett. **89**, 108101-1 (2002).

[59] R. Meili, B. Alonso-Latorre, J. C. del Alamo, R. A. Firtel, J. C. Lasheras, Mol. Biol. Cell **21**, 405 (2010).

[60] J. C. del Alamo, R. Meili, B. Alonso-Latorre, J. Rodriguez-Rodriguez, A. Aliseda, R. A. Firtel, J. C. Lasheras, Proc. Natl. Acad. Sci. USA **104**, 13343 (2007).

[61] M. Buenemann, H. Levine, W.-J. Rappel, L.M. Sander, Biophys. J. **99**, 50 (2010).

[62] P.A. DiMilla, J.A. Stone, J.A. Quinn, S.M. Albelda, D.A. Lauffenburger, The J. of Cell Biol. **122**, 729 (1993).

[63] P.A. DiMilla, K. Barbee, D.A. Lauffenburger, Biophys. J. **60**, 15 (1991).

[64] W. F. Loomis, D. Fuller, E. Gutierrez, A. Groisman, W.-J. Rappel, PLoS ONE **7**, e42033 (2012).

[65] M. Tarantola, A. Bae, D. Fuller, E. Bodenschatz, W.-J. Rappel, W.F. Loomis, PLos ONE **9**, e106574 (2014).

[66] V. Perumal, U. Hashim, J. Appl. Biomed. **12**, 1 (2014).

[67] L. di Blasio, P. A. Gagliardi, A. Puliafito, R. Sessa, G. Seano, F. Bussolino, L. Primo, J. of Cell Sci. **128**, 863 (2015).

[68] N. Ke, X. Wang, X. Xu, J. A. Abassi, Methods in Molecular Biology **740**, 33 (2011).

[69] P. A. Gagliardi, A. Puliafito, L. di Blasio, F. Chianale, D. Somale, G. Seano, F. Bussolino, L. Primo, Scientific Reports **5**, 10206 (2015).

[70] K. M. Pietrosimone, X. Yin, D. A. Knecht, M. A. Lynes, J. Vis. E. **62**, 3840 (2012).

[71] J. El-Ali, P.K. Sorger, K.F. Jensen, Nature **442**, 403 (2006).

[72] L. Song, S.M. Nadkarni, H.U. Bödeker, C. Beta, A. Bae, C. Franck, W.-J. Rappel, W.F. Loomis, E. Bodenschatz, Eur. J. Cell Biol. **85**, 981-989 (2006).

[73] C.R. Keese, J. Wegener, S.R. Walker, I. Giaever, PNAS **101**, 1554 (2004).

[74] J.F. Lee, Q. Zeng, H. Ozaki, L. Wang, A.R. Hand, T. Hlam E. Wang, M.J. Lee, JBC, 29190 (2006).

[75] Y. Xia, G.M. Whitesides, Angew. Chem. Int. Ed. **37**, 550 (1998).

[76] Y. Xia, G.M. Whitesides, Annu. Rev. Mater. Sci. **28**, 153 (1998).

[77] G.C.R. Ellis-Davies, Nat. Methods **4(8)**, 619 (2007).

[78] A. Yamaguchi, P. Jin, H. Tsuchiyama, T. Masuda, K. Sun, S. Matsuo, H. Misawa, Analytica Chimica Acta **468**, 143 (2002).

[79] S. Sawai, P. A. Thomason, E. C. Cox, Nature **433**, 323 (2005).

[80] L. Bosgraaf, A. Waijer, R. Engel, A. J. G. W. Visser, D. Wessels, D. Soll, P. J. M. van Haastert, J. of Cell Sci. **118**, 1899 (2005).

[81] E. K. B. Pfannes, M. Theves, C. Wegner, C. Beta, J. Muscle Res. Cell Motil. **33**, 95 (2012).

[82] An introduction to sputter coating can be found at the website www.youtube.com/watch?v=myiAv-5D47s.

[83] see the website www.elveflow.com with reviews and tutorials therein.

[84] N.L. Jeon, S.K.W. Dertinger, D.T. Chiu, I.S. Choi, A.D. Stroock, G.M. Whitesides, Langmuir **16**, 8311 (2000).

[85] J. Park, H.S. Kim, A. Han, J. Micromech. Microeng. **19**, 065016 (2009).

[86] T. Adrega, S.P. Lacour, J. Micromech. Microeng. **20**, 055025 (2010).

[87] I.R. Minev, S.P. Lacour, Applied Physics Letters **97**, 043707 (2010).

[88] P. Klan, J. Wirz, John Wiley and Sons (2009). (ISBN: 978-1-405-19088-6)

[89] V. Hagen, B. Debowski, V. Nache, R. Schmidt, D. Geißler, D. Lorenz, J. Eichhorst, S. Keller, H. Kaneko, K. Benndorf, B. Wiesner, Angew. Chem. Int. Ed. **44**, 7887 (2005).

[90] Yu. V. Pleskov, V. Yu. Filinovskii, (Springer, Berlin, 2012).

[91] E.G. Yarmola, T. Somasundaram, T.A. Boring, I. Spector, M.R. Bubb, The J. of Biol. Chem. **275(36)**, 28120 (2000).

[92] P. Seriburi, S. McGuire, A. Shastry, K.F. B
ohringer, D.R. Meldrum, Anal. Chem. **80**, 3677 (2008).

[93] J.-L. Martiel, A. Goldbeter, Biophys. J. **52**, 807 (1987).

[94] J.J. Tyson, K.A. Alexander, V.S. Manoranjan, J.D. Murray, Physica D **34**, 193 (1989).

[95] E. Palsson, K.J. Lee, R.E. Goldstein, J. Franke, R.H. Kessin, Proc. Natl. Acad. Sci. **94**, 13719 (1997).

[96] N. Kramer, A. Walzl, C. Unger, M. Rosner, G. Krupitza, M. Hengstschl ager, H. Dolznig, Mutation Research **752**, 10 (2013).

[97] N. Hadjout, G. Laevsky, D.A. Knecht, M.A. Lynes, Biotechniques **31**, 1130 (2001).

[98] N. Ibarra, S. L. Blagg, F. Vazquez, R. H. Insall, Current Biol. **16**, 717 (2006).

[99] E. F. Noratel, C.L. Petty, J. S. Kelsey, H. N. Cost, N. Basappa, D. D. Blumberg, Cell Biol. **13**, 29 (2012).

[100] P. J. M. Van Haastert, A. N. Hotchin, PLos ONE **6** e27532 (2011).

[101] C. Westendorf, J. Negrete Jr., A.J. Bae, R. Sandmann, E. Bodenschatz, C. Beta, PNAS **110**, 3853 (2013).

[102] H. U. Bödeker, C. Beta, T.D. Frank, E. Bodenschatz, EPL **90**, 28005 (2010).

[103] G. Amselen, M. Theves, A. Bae, E. Bodenschatz, C. Beta, PLoS ONE **7**, e37213 (2012).

[104] N. Makarava, S. Menz, M. Theves, W. Huisinga, C. Beta, M. Holschneider, Phys. Rev. E **90**, 042703 (2014).

[105] M. Skoge, M. Adler, A. Groisman, H. Levine, W.F. Loomis, W.-J. Rappel, Integr. Biol. **2**, 659 (2010).

Affidavit

I declare in lieu of oath, that I wrote this thesis and performed the associated research myself, using only literature cited in this volume. If text passages from sources are used literally, they are marked as such.
I confirm that this work is original and has not been submitted elsewhere for any examination, nor is it currently under consideration for a thesis elsewhere.

Potsdam, May 2017

_____

Signature

Acknowledgements

I would like to thank all current and former members of the Biological Physics group of Potsdam University, most notably Matthias Gerhardt, Kirsten Krüger, my professor Carsten Beta and also Marco Tarantola of the MPI Göttingen for their contributions to my work and support. These contributions are the following:
Dr. Matthias Gerhardt has designed the transamplifier system used for our experimental setup to measure the magnitude of impedance shown in Fig. 3.1. He also contributed to the development and fabrication of microelectrode arrays and microchannel systems introduced in section 3.6 and 3.7.
Our chemical-technical assistent Kirsten Krüger comprehensively contributed to the biological part of my work. She guided the laboratory work concerning the cultivation and preparation of cells for all experiments and for the detachment assays introduced in section 3.4 and shown in Fig. 4.6 E.
Dr. Marco Tarantola conducted the experiments for Single Cell Force Spectroscopy introduced in section 3.5 and shown in Fig. 4.6 D and all Interference Reflection Microscopy studies shown in Fig. 4.2.
I would also like to thank my parents for their support during the past years.

Helmar Leonhardt
Potsdam, May 2017